Bayesian Atmospheric Retrieval for Exoplanets

Uniqueness of Exoplanet Spectra, Characterizations of Super-Earths, and Evaluations of Dedicated Space Telescope Designs

by

Björn Benneke

Submitted to the Department of Aeronautics and Astronautics
in partial fulfillment of the requirements for the degree of

Doctor of Philosophy

at the

MASSACHUSETTS INSTITUTE OF TECHNOLOGY

June 2013

Author .....
Department of Aeronautics and Astronautics
May 23, 2013

Certified by .....
Sara Seager
Professor of Planetary Science, Professor of Physics
Thesis Supervisor

Certified by .....
David W. Miller
Professor of Aeronautics and Astronautics
Thesis Committee

Certified by .....
Kerri L. Cahoy
Assistant Professor of Aeronautics and Astronautics
Thesis Committee

Certified by .....
Joshua N. Winn
Associate Professor of Physics
Thesis Committee

Accepted by .....
Eytan H. Modiano
Professor of Aeronautics and Astronautics
Chair, Graduate Program Committee

Bayesian Atmospheric Retrieval for Exoplanets

Uniqueness of Exoplanet Spectra, Characterizations of Super-Earths, and Evaluations of Dedicated Space Telescope Designs

by

Björn Benneke

Submitted to the Department of Aeronautics and Astronautics
on May 23, 2013, in partial fulfillment of the
requirements for the degree of
Doctor of Philosophy

Abstract

After centuries of studying the eight planets in our solar system, recent improvements in technology have given us the unprecedented opportunity to detect planets orbiting stars other than the sun, so-called exoplanets. Recent statistical studies based on 800 confirmed planets and more than 3000 planet candidates suggest that our galaxy is teeming with billions of planets. Many of them are likely to orbit their host stars at a distance where liquid water and potentially life can exist. Spectroscopic observations of exoplanets can provide us with information about the atmospheres and conditions on these distant worlds.

This thesis presents a Bayesian retrieval framework to analyze spectroscopic observations of exoplanets to infer the planet's atmospheric compositions, the surface pressures, and the presences of clouds or hazes. I identify what can unambiguously be determined about the atmospheres of exoplanets by applying the retrieval method to sets of synthetic observations. The main finding is that a *unique* constraint of the atmospheric mixing ratios of all infrared absorbing gases and up to two spectrally inactive gases is possible if the spectral coverage of the observations is sufficient to (1) determine the broadband transit depths in at least one absorption feature for each absorbing gas and (2) measure the slope and strength of the molecular Rayleigh scattering signature.

For the newly discovered class of low-density super-Earths, with radii and masses intermediate between Earth and Neptune, I present an observational approach to distinguish whether these planets more closely resemble the giant planets in our solar system or whether they represent a completely new, potentially water vapor-rich type of planet. The approach discussed in this work represents the science case for the largest Hubble Space Telescope program ever awarded for a single exoplanet.

The numerical methods and the conceptual understanding of atmospheric spectra presented in this thesis are key for the design of future space telescopes dedicated to

the characterization of transiting exoplanets. I present an integrated design evaluation framework for the proposed Exoplanet Characterization Observatory (EChO) that simultaneously models the astrophysical signal and the telescope's payload module. I demonstrate that costly cryogenic cooling to observe the mid-infrared spectrum beyond $\sim 11\,\mu$m is not required while visible light observations down to $\sim 400\,$nm are essential for the mission success.

The observational study of exoplanet atmospheres is in its infancy and its pace is poised to accelerate as observational techniques are improved and dedicated space missions are designed. The methods developed in this thesis will contribute to constraining the atmospheric properties of a wide variety of planets ranging from blazingly-hot gas giants to temperate Earth-like planets.

Thesis Supervisor: Sara Seager
Title: Professor of Planetary Science, Professor of Physics

Acknowledgments

First and foremost, I would like to express my sincere gratitude to my PhD advisor, Professor Sara Seager, for her outstanding mentorship, guidance, and friendship. She has always been available to offer valuable support when needed, and also gave me strong encouragements and independence to pursue my own ideas. I am particularly grateful to her for introducing me to my dream job: studying the nature of distant worlds. I am inspired by her ambitious long-term vision, her work efficiency, and her strong voice in the scientific community. From her, I have learned that, with sufficient ambition, one can pursue virtually any scientific and engineering goals, independent of one's main field of expertise.

I would also like to thank the members of my thesis committee, Professors Josh Winn, Kerri Cahoy and David Miller. I am grateful to Josh Winn for important scientific and career advice. I am inspired by his expertise and his organized way of conducting and communicating science. Kerri Cahoy's and David Miller's engineering perspectives have been valuable to this research project which is on the verge between aerospace engineering and scientific exploration.

At the University of Chicago, I would like to thank Professor Jacob Bean for his collaboration in observationally studying super-Earths. I am grateful that, with his expertise as an exoplanet observer, we are able to conduct the observations of GJ 1214b suggested in this thesis using the *Hubble Space Telescope*.

I am grateful to Professor Zoltan Spakovzsky for bringing me to MIT and two years of guidance during my Master's thesis project. His guidance has made me a better researcher that greatly helped me during my doctoral research.

In the MIT exoplanet team, I would like to thank Leslie Rogers, Brice Demory, Julien de Wit, Nikku Madhussudhan, Andras Zsom, Vlada Stamenkovic, Renyu Hu, Stephen Messenger, Brice Croll, Roberto Sanchez, and Amaury Triaud for their the camaraderie and scientific discussions. They have supported me with advice and friendship. I very much enjoyed the productive atmosphere in this group of exceptional scientists.

Outside the exoplanet community, I would like to thank many friends in Boston who made the last six years an unforgettable experience. In particular, I would like to thank Andreas, Francois, Fabio, Sameera, Jeff, Jon, Liz, Leo, Josh, Irene, Been, and Jaime.

I would like to thank my high school physics teacher, Berndt Wasser, for dedicating his free time to offer a physics A-course outside the regular curriculum. Without his selfless support, my career may have taken a different route. I am grateful to my first physics teacher, Joachim Förster, for awakening my natural interest in science and engineering.

I am grateful to my parents and my brother for their love and personal support and always encouraging me to go my own ways. Finally, but most importantly, I would like to thank Blair who has my eternal gratitude and love for her encouragements and her immense support and understanding over the entire course of my graduate career.

Contents

List of Figures

List of Tables

Nomenclature

Abbreviations

CLR	Centered-log-ratio transformation
EChO	Exoplanet Characterization Observatory
FCS	Flat field calibration
FGS	Fine Guiding System
FPA	Focal plane array
IR	Infrared
JWST	James Webb Space Telescope
LW	Long-wavelength
PAS	Pupil adapter system
MCT	Mercury cadmium telluride
MCMC	Markov Chain Monte Carlo
NIR	Near-infrared
RMC	Restricted Monte Carlo
SW	Short-wavelength
TMA	Three mirror anastigmats camera
VIS	Visible

Roman Symbols

A_{P}	Planetary Bond albedo

B	Bayes factor
a_{P}	Semi-major axis or planet orbit
b	Impact parameter
C_p	Specific heat capacity
$\boldsymbol{D}$	Vector of observational data
D_{Rayl}	Rayleigh scattering slope
e	Orbital eccentricity
F_K	King correction factor
f	Ratio between observational time in-transit and out-of-transit
G	Gravitational constant
g	Surface gravity
H	Scale height
i	Orbital inclination
K	Semi-amplitude of the line-of-sight motion
k_{B}	Boltzmann's constant
M_{atm}	Total mass of atmosphere
M_i	Retrieval model i
M_P	Planet mass
M_*	Stellar mass
N	Number of data points
n	Number density
n_ν	Refractive index
n_σ	"sigma" significance
P	Orbital period
p	Pressure
p_{Surf}	Surface or cloud-top pressure
$p(\boldsymbol{x})$	Probability density
q_j	Mole fraction of element j
R	Spectral resolving power
R_{P}	Planetary radius

$R_{\mathrm{P},10}$	Planetary radius at 10 mbar pressure level
$R_{\mathrm{P,Obs}}$	Observed transit depths
R_*	Radius of the host star
r	Radius
T	Temperature
T_{eq}	Equilibrium temperature
T_{int}	Internal luminosity
V	Prior volume
X_i	Mole fraction of molecular species i
w_i	Weight of data point i

Greek Symbols

β	"Temperature" parameter
Δ	Difference
δ	Transit depth
δT	Model temperature error
Γ	Adiabatic lapse rate
γ	Ratio of mean visible opacity and mean thermal opacity
λ	Wavelength
λ_{peak}	Peak wavelength of black body emission
μ_{mix}	Mean molecular mass
ν	Wave number
π	Prior probability distribution
ρ	p-value
σ	Standard deviation
σ_λ	Extinction cross section
σ_R	Rayleigh scattering cross section
τ	Optical depth

$\boldsymbol{\theta}$	Retrieval parameter vector
$\boldsymbol{\xi}$	Vector of centered-log-ratio transformed composition

Subscripts

$_{\mathrm{HR}}$	High resolution
$_{\mathrm{min}}$	Minimum
$_{\mathrm{P}}$	Planet
$_{\mathrm{ref}}$	Reference value
$_{*}$	Star

Mathematical Notation

$\mathcal{H}$	Negative entropy
$\mathcal{K}$	Modified Bessel function of the second kind
$\mathcal{L}$	Likelihood function
$\sum$	Sum
$\mathcal{Z}$	Bayesian evidence

Chapter 1

Introduction

In the two decades since the first detection of the first exoplanet, dedicated surveys have detected the existence of more than 800 confirmed planets and more than 3000 planet candidates. Recent statistical studies based on these planets suggest that there must be billions of planets in our galaxy alone. Millions of these planets are suggested to orbit their host stars in what is called the habitable zone, a region where the heat received from the host star is just right to allow the presence of liquid water and a temperate climate similar to that on our own planet, Earth.

Modern astronomical facilities enable us to remotely probe the physical and chemical conditions in the atmospheres of exoplanets, despite their inconceivable distance to Earth. By observing the spectral intensity of light transmitted through or emitted or reflected by the atmosphere, we are able to infer the gas composition and the physical conditions in the atmospheres of distant exoplanets. The studies of exoplanets give us the unprecedented opportunity to put our solar system, including the formation and characteristics of our Earth and our own existence, into the larger context of the universe. Ultimately, one of the goals of exoplanet characterization is to search for atmospheric biosignatures to answer the ancient question "Are we alone?".

This thesis is devoted to developing the necessary tools to infer the conditions on distant exoplanets in a statistically robust manner and to guide the design of dedicated space telescopes. I provide a conceptual understanding of the information that can be provided by spectroscopic observations of planets, identify how to best

characterize a new type of planets called super-Earths, and provide recommendations for the design of a proposed dedicated space mission for exoplanet exploration.

1.1 Background

1.1.1 Basic Ingredients of Planet Formation

Solar System exploration and astronomical observations of stars and the interstellar medium have provided us with empirical evidence about the "raw materials" that can serve as the basic building blocks for the formation of stars and planets. Today we know that more than 98% of the baryonic mass in the universe is hydrogen and helium gas. The next most abundant elements in the universe by mass are O, C, Ne, N, Mg, Si, Fe, Al, S, Ca, Na, and Ni, and together they make up the vast majority of the universe's remaining mass, leaving only $< 0.14\%$ for all other elemental species. The relative abundances of the elements were set by nucleosynthesis in the very early universe after the Big Bang and in stellar interiors and supernovas. Together with our knowledge of the chemical properties of the elements, their relative abundances can be regarded as prior information to identify which are the most plausible molecular and atomic species to form the planets.

Observations of the Solar System planets and protoplanetary disks around other stars show that considerable fractionation of the elements takes place during the planet formation process. The main driver for fractionation of the elements is the difference in condensation temperatures of the most stable molecular forms of the elemental species. Shortly after the formation of a protostar, refractory materials in circumstellar nebula with high condensation are able to condense out first and closest to the star, while volatile species can condense only at several astronomical units distance to the star or not at all.

According to their condensation temperature, we generally divide the basic building blocks of planets into three categories: "Refractory materials" or "rocks" are materials with condensation temperatures between ~300 and 1700 K. The dominant

mineral and molecular forms of mainly Mg, Si, Fe, Al, S, Ca, Na, and Ni can be found as solids in the inner Solar System. "Ices" are chemical compounds with low boiling temperatures and melting points above about 100 K. The can be stable in solid, liquid, or gaseous form near the surface of a planet. Examples include H_2O, CO_2, CO, CH_4, NH_3, N_2, SO_2. The ices bind the majority of the available carbon and oxygen that is not incorporated into mineral form as rock. "Gases" are substances such as H_2 and He with condensation temperatures below $\sim$ 40 K that remain in gaseous form even at large distances from stars.

1.1.2 The Solar System Planets

The composition of the planets in the Solar System follows the trends suggested by the different condensation temperatures of the basic planet forming materials. The planets in the inner Solar System are terrestrial or "rocky" and are mainly composed of refractory materials that accreted from the material that condensed first in the circumsolar nebular. Earth's interior, for example, is composed of approximately 97% refractory materials formed from the elements Fe, Si, Mg, Ca, and Al as well as the oxygen included in the minerals. The atmospheric composition of the terrestrial planets then evolved as a complex interplay of outgassing from the planet's interior, loss of light species through atmospheric escape, and chemical reaction with and near the surface.

The giant planets in the outer Solar System have undergone a different formation process. The current most plausible scenario is that their hypothesized core formed through the accretion of icy material that condensed out beyond the "ice-line" at around 2 – 3 AU from the sun. The strong gravitational pull of the newly formed core was then able to accrete vast amounts of hydrogen and helium gas from the circumstellar disk in the vicinity of the planet — finally forming the hydrogen/helium dominated atmospheres observed today.

This distinct formation scenarios of the terrestrial and giant planets may explain the clear categorization between relatively small rocky planets in the inner solar system and massive giant planets. The solar system hosts no intermediate sized planets.

1.1.3 Planetary Spectra

Our exquisite knowledge about the Solar System planets is a result of decades of studies using orbiters, fly-bys, in-situ probes, landers, sample returns, and Earth-based astronomical observations which provide spectroscopy as well as resolved images. While exoplanet exploration offers the chance to study thousands of more planets, exoplanet studies of the foreseeable future will be fundamentally limited to spectroscopic observations without the ability to spatially resolve any surface or cloud features.

The reason for the difference in our ability to study exoplanets and Solar System planets is enormous distance to stars other than the sun. The closest exoplanets are of the order $\sim 10,000 - 100,000$ times further away from us than the planets in our Solar System. The enormous distance prevents us, in the foreseeable future, from sending any robotic probes or obtaining any resolved images of the planet's surface.

Depending on the viewing geometry and the wavelength range observed, we can distinguish three types of planetary spectra (Figure 1-1): reflective spectra, thermal emission spectra, and transmission spectra. Reflective spectra are the ones most familiar to humans because we generally see reflected visible light when we observe objects in our direct environment or a planet through a telescope. Most of the analysis in this work is, however, devoted to the interpretation of transmission spectra.

Reflective Spectra The "reflective spectrum" measures the wavelength dependent intensity of light that originated from the star and is scattered back to the observer by the planet's surface or atmosphere. Earth, for example, appears blue on photographs taken from space because Rayleigh scattering of gas molecules in Earth's atmosphere scatters light at short wavelength most efficiently. The higher reflectivity of blue is manifested as a higher reflectance towards 400–500 nm (Figure 1-1(a)). At near-infrared wavelengths, the reflectance of Earth shows features that are characteristic of the gases in the atmosphere and the reflectance of Earth's surface. Strong

absorption features of water vapor and oxygen in Earth's spectrum lead to characteristic absorption features at 0.82, 0.94, 1.13, and 1.4 μm and 0.76 and 1.27 μm, respectively. At these wavelengths, a fraction of the light intensity that originated from the star and was scattered by the Earth's surface is absorbed along its path through the atmosphere, leading to characteristic dips in the reflective spectrum. It is the presence and shape of the dips in the spectra that provides us with information about the gases present in the atmosphere and their abundances.

Thermal emission spectra The "thermal emission spectrum", the second type of planetary spectrum, measures the light that is directly thermally emitted by the planet due to the inherent temperature. Known as Wien's displacement law, a result of the laws of black body radiation, the peak of black body emission occurs at the wavelength

$$\lambda_{peak} = \frac{2.897 \cdot 10^{-3}\,\mathrm{K} \cdot \mathrm{m}}{T}, \tag{1.1}$$

where T is the temperature of the emitting body. For temperate planets such as Earth, the peak of thermal emission occurs, therefore, at $6 - 25\,\mu$m (Figure 1-1). The emission spectrum of a bare rocky surface would resemble the smooth Planck function of a black body radiator. The gases in Earth's atmosphere, however, "bite" chunks out of the smooth black body spectrum that are characteristic to the gases in the atmosphere. The absorption features occur because the cool gas at high altitude absorbs the thermally emitted light from the surface and re-radiates some of the absorbed energy a lower intensity. The opposite happens if warmer layers or the atmosphere are on top of of cooler air. The central peak of the CO_2 feature at 15 μm, for example, is a result of the increase in temperature with altitude in Earth's atmosphere (Figure 1-1(b)). Altogether the thermal emission spectrum is a complicated convolution of the planet's surface temperature, the vertical temperature profile of the atmosphere, and abundances of gas and particles in the atmosphere.

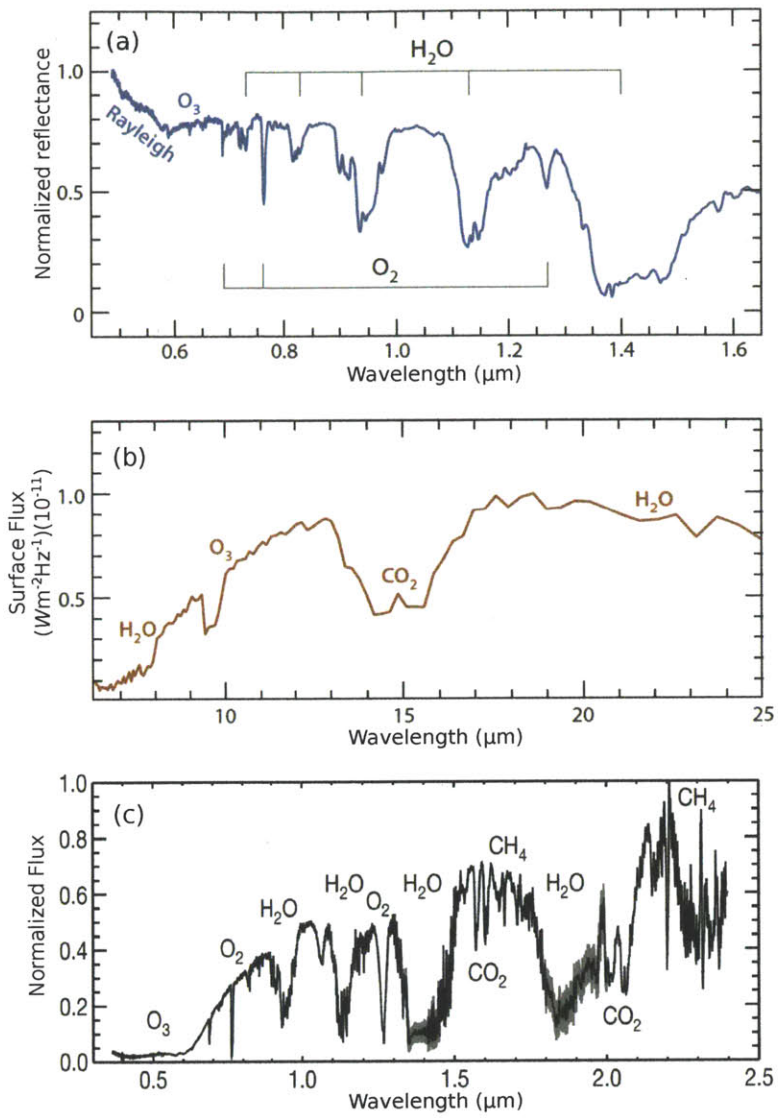

Figure 1-1: Observed global spectra of Earth. The spectra illustrate how Earth would look like as an exoplanet if observed from a distant star. The reflective spectrum (a) was obtained from an Earthshine measurement from the dark side of the moon by Turnbull et al. (2006). The thermal emission spectrum (b) was observed by the Mars Global Surveyor en route to Mars (Christensen & Pearl, 1997). The transmission spectrum (c) was inferred from a lunar eclipse observation by Palle et al. (2009). Panels (a) and (b) are adapted from Seager & Deming (2010). The simultaneous presences of molecular oxygen (O_2), water vapor (H_2O), and methane (CH_4) are detectable in the spectra and would be a clear indication of biological activity on Earth.

Transmission spectra The "transmission spectrum" of a planetary atmosphere can be observed if the star as a bright light source is aligned behind the observed planet as seen from the observer. For exoplanets, the transmission spectrum can be observed if the orbit of the planet is fortuitously aligned such that the planet temporarily crosses in front of its host star (see also Section 1.1.4). A small fraction of light beams originating from the star then transmit through the atmosphere of the exoplanet on its path to the observing telescopes. At wavelengths characteristic to the gases in the planet's atmosphere, light is absorbed or scattered out of the line-of-sight, leading to a decrease in the observed light intensity (Figure 1-1(c)). Rayleigh scattering, which is most efficient at short wavelengths, is the reason why the limb of Earth's atmosphere is mostly opaque to blue light, resulting in the red color of the moon during lunar eclipses.

Out of the three types of spectra described above, the transmission spectrum contains the information about the desired atmospheric composition of a planet in the least convoluted form. Reflective spectra are generally a complex convolution of surface reflectivity, cloud particle reflectivity, and abundances of atmospheric. The shapes of features in thermal emission spectra are a convolution of the surface temperature, the vertical temperature profile of the atmospheres, and the abundances of the gases. Additionally, a spectrum of an unresolved planet is generally an average spectrum of surface patches of different spectral properties and temperature and with or without cloud coverage. Transmission spectra, on the other hand, are dominated by the atmospheric composition because the surface reflectance has no direct influence and the opacities of the gases are only weakly dependent on the exact temperature in the atmosphere.

1.1.4 Observational Techniques for Exoplanet Planets

There are currently three main techniques employed to study the composition and atmospheres of exoplanets: direct imaging spectroscopy, transit spectroscopy, and radial velocity measurements of the host star.

Direct Imaging Spectroscopy The conceptually most straightforward way to study the atmospheres of exoplanets is to take a direct image of the planet as a point source and to analyze the light the planet emits or reflects as a function of the wavelength. Direct imaging of exoplanets is in its infancy, however, because obtaining an image of a faint planetary companion adjacent to a bright host star presents an extreme technological challenge. The contrast between planets in our Solar System and our sun, for example, ranges between 10^{-9} and 10^{-10}, making the detection of planets like Earth or Jupiter around another sun-like star impossible with currently available astronomical instrumentation. Exoplanet spectra have, however, been observed using direct imaging for young giant planets that orbit host stars at large separation and emit strongly at near-infrared because they still irradiate their accretion heat (e.g., Oppenheimer et al., 2013). Many instruments for ground-based facilities are currently being developed to significantly expand our ability to study atmospheres through direction imaging over the next several years (e.g., Macintosh et al., 2008; Hinkley et al., 2011).

Transit Spectroscopy The dominant source of information about exoplanet atmospheres to date is provided by transit and eclipse spectroscopy. For a small subset of exoplanets, the orbit is fortuitously aligned such that the planet crosses in front of and behind the star once on every orbit around the star (Figure). This alignment enables us to detect the planets, measure their sizes relative the sizes of their host stars, and to obtain atmospheric spectra, without the need for spatially resolving the faint planet from the adjacent bright star.

During the primary transit, i.e. when the planet crosses in front of its host star, some of the star light is blocked by the planet, leading to a characteristic dip in the observed brightness of the star (Winn, 2011). Assuming a uniformly bright stellar disk, the transit depth δ, or the relative decrease in observed stellar brightness, can be related the planet's size by

$$\delta = \left(\frac{R_P}{R_*}\right)^2, \tag{1.2}$$

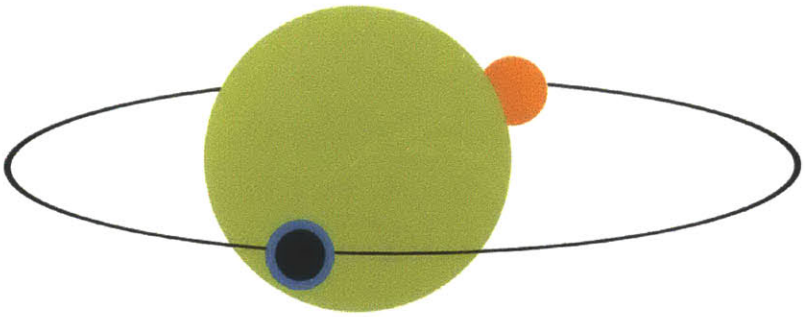

Figure 1-2: Viewing geometry of a transiting planet. Figure adopted from Seager & Deming (2010).

where R_P is the radius of the planet and R_* is the size of the planet's host star. Given an estimate of the stellar radius $R_*$from stellar models, we can thus infer the planetary radius R_P. The magnitude of the transit depth ranges from a few percent for a Jupiter-sized planet around a small star down to ~ 84 parts per million (ppm) for an Earth-sized planet around a sun-like star.

If the transiting planet hosts an atmosphere, some of the star light grazing the planet will be absorbed or scattered at wavelengths characteristic to the atmospheric gases. As a result, the transiting planet will appear slightly bigger at wavelengths with strong absorption. Measurements of the wavelength dependent transit depth $\delta(\lambda)$ form the "transmission spectrum" of the planet.

The event where the planet crosses behind the star is referred as a the occultation of the planet (Figure 1-2). The occultation of the planet also results in a dip in the brightness of the unresolved star/planet system. During the occultation the star blocks the light emitted and reflected by the planet and we only receive light from the star. Subtracting the brightness of the star alone during secondary eclipse from the summed brightness of the star just before and after the occultation provides us with a measurement of the planetary emission. Spectroscopic measurements provide the "occultation spectrum" characteristic of the planet's temperature, albedo, and composition.

Radial Velocity Technique Radial velocity measurements of an exoplanet's host star are very complementary to transit measurements in that they provide constraints

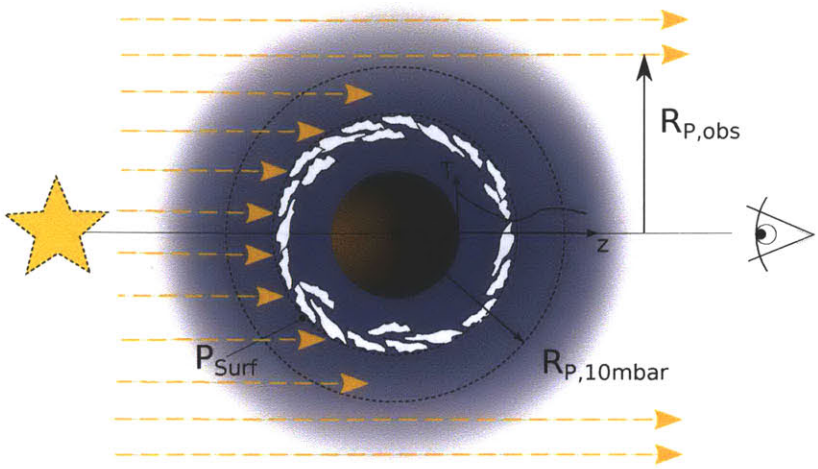

Figure 1-3: Side view of Figure 1-2 during primary transit. The star grazing the planet is transmitted through the atmosphere. At wavelength for which the atmospheric gases are opaque, part of the light is absorbed in deep layers of the atmosphere and does not arrive at the observer. The observed planetary radius $R_{\mathrm{P,obs}}$ varies as a function of wavelength and results in a transmission spectrum $\delta = (R_p/R_*)^2$.

on the mass of the planet. Knowing the mass and radius of transiting planets enables us to calculate the planet's bulk density and surface gravity, and to infer constraints on the composition of the planetary interior. Both surface gravity and interior composition present important information in modeling and constraining the atmospheres of exoplanets.

The radial velocity technique is based on measuring the back and forth wobble of the star as a result of the gravitational tug of the orbiting planet. The line-of-sight component of this motion can be inferred by measuring the Doppler shift of spectral lines in the thermal emission spectrum of the star. The semi-amplitude of the line-of-sight velocity variations is

$$K = \left(\frac{2\pi G}{P}\right)^{1/3} \frac{M_p \sin i}{(M_* + M_p)^{2/3}\sqrt{1-e^2}}, \tag{1.3}$$

where G is the gravitational constant, M_* and M_p are the masses of the star and planet, and P, i, and e are the period, inclination, and eccentricity of the planet's orbit.

Typical semi-amplitudes range from several hundreds of m/s for hot giant planets

close to their host stars to 10 cm/s for an Earth-mass planet around a sun-like star. Today's instruments are able to determine the line-of-sight motion of distant stars with a precision as good as 1 m/s for favorable stars. Given a model estimate of the stellar mass, the measurements provide the product, $M_p \sin i$, of planetary mass and the sine of the orbital inclination of the planet relative to the sky plane. For favorable planets that are also detected through their transit signal, we know the inclination of the planets, and, thus, can infer the planetary mass and calculate the bulk density and surface gravity of the planet. The radial velocity technique has been the most successful technique at detecting exoplanets to date.

1.1.5 Atmospheric Modeling

A wide variety of atmospheric models are used to compute atmospheric spectra of planetary scenarios. Early theoretical work on exoplanet atmospheres has been dominated by self-consistent atmospheric models that take into account the chemistry and dynamics of the atmospheres of giant planets to come up with plausible planet scenarios (e.g. Seager et al., 2000; Burrows & Sharp, 1999).

Despite the early successes of traditional self-consistent models in the interpretation of observational data, limitations become more and more apparent. Model success included the identification of thermal inversion in the atmospheres of hot Jupiters (e.g., Knutson et al., 2008), and a classification system for giant exoplanets (Burrows et al., 2008; Fortney et al., 2008). However, while self-consistent models of atmospheric chemistry aim to provide the physical understanding of the relevant processes in the atmosphere, they are dependent on inputs such as the background atmosphere or the elemental abundances, the boundary conditions at the surfaces, as well as an accurate representation of all relevant chemical reactions, heat transport and cloud formation processes. If we knew all of the inputs and relevant processes a priori, one could compute the chemical composition and state of the atmosphere with self-consistent models. Many of these inputs, however, are not known, especially for planets that do not agree with our preconceived ideas from solar system planets. As a result, self-consistent models will often not be able to match the observations to

within the observational error bars, forcing the modelers to use ad hoc parameters to explain the data (e.g., Knutson et al., 2008). The models are therefore no longer fully self-consistent. The shortcomings of self-consistent modeling in directly interpreting observations are aggravated for planets in the super-Earth regime or smaller. For super-Earths, the elemental abundances are unknown a priori and atmospheric chemistry models have no starting point in determining the atmospheric compositions.

1.1.6 Atmospheric Retrieval

Atmospheric retrieval solves the inverse problem to atmospheric modeling. The question is: What are the constraints on the atmospheric properties given an observed atmospheric spectrum? Atmospheric retrieval deliberately reduces the assumptions in atmospheric modeling by introducing free parameters for atmospheric properties that cannot be determined from physical or chemical principles because too little is known about the planet. The observational data is then used to fit the free retrieval parameters.

Studies of the planetary atmosphere by remote-sensing have a long history in the Solar System and for Earth. Early retrieval methods for remote-sensing the temperature profile of Earth's atmosphere were developed by Smith (1970) and Chahine (1974). Variants of these methods were developed to retrieve the abundances of minor species and temperature profiles in other Solar System planets (e.g. Conrath, 1998; Susskind et al., 2003). The classical theory of inverse problems in atmospheric sounding is reviewed in Rodgers (2000). Similarly, in the astrophysical community, tools were developed to fit observations of stellar spectra with models (Valenti & Piskunov, 1996). A general overview of the inversion strategies for remote-sensed data in the astronomy context can be found in Brown & Craig (1986). Interestingly, the literature reveals that many of the techniques for retrieval problems overlap with techniques developed for optimization in electrical and systems engineering. Methods for retrieval, inversion, and optimization are effectively all methods for parameter estimation and were reinvented independently in different fields.

The main difference between our approach and the "classical" gradient-based tech-

niques developed for Solar System studies is that the traditional techniques benefit from a fairly good knowledge of the environment under investigation and are not particularly applicable to extrasolar planets of entirely unknown composition. Usually, the goal of the classical methods is to derive the abundances of trace gases or to characterize the exact temperature field of the atmosphere in well-characterized atmospheres, while the composition and thickness of the atmosphere is completely known beforehand. The prior information of the main constituents and thickness is used to constrain the initial parameter set, and the gradient-based retrieval method searches for the best possible solution that reproduces the observed spectrum in the local domain of the initial condition. The assumption that the solution needs to belong to the local domain of the initial condition is an unavoidable short-coming of traditional gradient-based methods. For extrasolar planets, there will, in general, be no such prior knowledge of the nature and thickness of the atmosphere. Instead, one aims to identify the main constituents of a completely unknown atmosphere, while being fundamentally constrained by limited data.

1.2 Comparisons to Other Atmospheric Retrieval Methods for Exoplanets

1.2.1 The "Millions of Models" Approach

The approach presented in this work builds on the idea introduced in the pioneering works on hot Jupiters by Madhusudhan & Seager (2009) and Madhusudhan et al. (2011b) to use Monte Carlo methods to explore the parameter space for solutions that are in agreement with the observations. The method presented here is different in the following five ways:

1. The framework described in this work conducts a full Bayesian analysis to determine statistically robust Bayesian credible intervals for the atmospheric parameters. The constraints on individual atmospheric parameters are derived directly by marginalizing the joint posterior probability distribution obtained from ei-

ther the Markov Chain Monte Carlo (MCMC) technique or nested sampling. Madhusudhan et al. (2011a) used the MCMC technique to explore the model parameter space in the search for regions that provide good fits to the data. Based on the parameter exploration they were able to report contours of constant goodness-of-fit in the parameters space. Contours of constant goodness-of-fit, however, cannot directly be related to the confidence regions of the desired parameters.

2. In choosing the atmospheric retrieval model, the questions arise as to how much complexity and how many free parameters should be included in the retrieval model. In this work, we introduce *Bayesian model comparison* to determine which molecular gases and types of aerosols can be inferred from the data and need to be included in the analysis. The approach enables us to rationally adapt the complexity of the retrieval model to the available data. Exquisite observational data with high signal-to-noise ratio (S/N) and high spectral resolution allow the inference of the detailed abundance profiles of the molecular species, the temperature structure, and the presence of particles in the atmospheres. At lower S/N and sparse spectral coverage, however, retrieval models with fewer parameters are employed because complex retrieval would overfit the available data and introduce strong degeneracies.

3. The retrieval method presented in this work is applicable to atmospheres of general composition and considers the presence of clouds, hazes, and a solid surface. We introduce concepts of compositional data analysis, a subfield of statistical analysis, to treat the mixing ratios of all molecular constituents equally while ensuring that the sum of the mixing ratios is unity.

4. We use a radiative-convective model to calculate temperature-pressure profiles that are self-consistent with the molecular compositions of the model atmospheres. Temperature-pressure profiles that are physically inconsistent are not considered in the retrieval analysis.

5. The parallel tempering MCMC scheme and nesting sampling technique used in this work enables a reliable exploring of the full parameter space, even if multiple, distinctly different atmospheric scenarios match the observational data. This is in contrast to the basic Metropolis-Hastings MCMC algorithm used in Madhusudhan et al. (2011a) which can fail to fully explore the parameter space if posterior distribution is multi-modal with widely separated peaks.

1.2.2 Optimum Estimation Retrieval

The retrieval method presented in this work is also very different from optimum estimation retrieval, as recently applied to exoplanets by Lee et al. (2011) and Line et al. (2012), in that we derive the full probability distributions and Bayesian credible regions for the desired atmospheric parameters, while optimum estimation retrieval assumes Gaussian errors around a single best-fitting solution. Highly non-Gaussian uncertainties of the atmospheric parameters need to be considered for noisy exoplanet observations because the observable atmospheric spectra are highly nonlinear functions of the desired atmospheric parameters, and a large volume in the parameter space are generally compatible with noisy exoplanet spectra. Our approach to calculate the joint posterior probability distribution using MCMC is computationally intensive ($\sim 10^5$ model evaluations are required), but it enables us to extract all that can be inferred about the atmospheric parameters from the observational data. The uncertainty of individual atmospheric parameters introduced by complex, non-Gaussian correlations to other parameters is accounted for in a straightforward way by marginalizing over the remaining parameters. Optimum estimation retrieval, in contrast, searches for a single best-fitting solution using the Levenberg-Marquardt algorithm. Gaussian uncertainties are estimated around the best-fitting solution by linear analysis (Rodgers, 2000; Lee et al., 2011) or by performing multiple retrieval runs with individual parameters fixed at particular values (Lee et al., 2011). Optimum estimation retrieval requires fewer model evaluations (typically $\sim 10 - 20$ per retrieval run, multiplied by the number of retrieval runs performed with individual parameters fixed) and may therefore allow the use of more complex atmospheric mod-

els given the same computational resources. For noisy exoplanet spectra, however, the optimal estimation retrieval may not correctly represent the confidence regions of the atmospheric parameters because the uncertainties of the atmospheric parameters are highly non-Gaussian.

1.3 Motivation

This work has two primary motivations. First, for the scientific interpretation of exoplanet observations, there is a strong need for a tool to retrieve atmospheric and surface properties from planetary spectra in a statistically robust way, and independently of preconceived planetary scenarios. Second, for future explorations, we need to understand how to conceptually design a space telescope dedicated to the exploration of exoplanets.

1.3.1 Interpretation of Observed Planetary Spectra

As the first observations of the transmission spectrum of the super-Earth GJ 1214b become available, the current practice in interpreting the observed spectra is to check the observations for their agreement to preconceived atmospheric scenarios (Miller-Ricci & Fortney, 2010; Bean et al., 2010; Croll et al., 2011). We identify two short comings of this approach: First, even if a good fit is reached between the data and the model spectrum of preconceived scenario, we do not know whether we actually understand the nature of the planet or whether we have simply found one out of several possible scenarios matching the data. Second, and even more important, we will not be able to understand planets that disagree with our preconceived ideas. These planets, however, likely represent the most compelling science cases, as they may provide new insights into planetary formation and evolution, atmospheric chemistry, or astrobiology. We therefore identify the need for a tool to analyze exoplanet spectra independently of preconceived planetary scenarios.

1.3.2 Design of Space Telescope Instrumentation

Despite the initial successes of currently available space telescopes in characterizing the atmospheres, their limitations at providing conclusive and unique constraints on the atmospheric composition has become increasingly apparent. One obstacle in the planning of future observations and designing new instruments for the efficient characterization of exoplanets is that we are missing a clear understanding of which individual atmospheric properties, beyond the pure detection of molecular absorbers, can be inferred uniquely from planetary spectra, and what measurements are required to obtain the desired constraints. Most proposals and white papers for space telescopes for exoplanet characterizations (e.g. Shao et al., 2010) state the detection of a molecular absorber as the science objective for characterization, implicitly assuming that the pure detection of a molecular absorption feature is sufficient to answer the significant science questions. Measurement requirements on spectral resolution and S/N level are then set based solely on the detection of the molecular absorption features without taking into account how well the abundances of these species can be determined. The ability to quantitatively constrain the abundances, however, will be essential to answer fundamental science questions such as: What role does non-equilibrium chemistry play in determining atmospheric compositions? What are the elemental abundances, and how do they constrain the formation and evolution histories? What are the conditions for habitable-zone "super-Earths," and is there potential for generating and sustaining life? Therefore, the scientific success of the space mission strongly depends on the ability to characterize the atmosphere beyond the pure detection of molecular absorber features and should be accounted for in the design.

1.4 Research Questions and Objectives

The interpretation of spectroscopic observations of exoplanets requires inverse models to derive statistically robust constraints on the composition and properties of the exoplanet's atmosphere. This thesis is devoted to establishing a Bayesian method to

retrieve atmospheric properties from observations of the planets spectrum. The key research questions of this work are as follows:

1. Uniqueness of exoplanet spectra:

   (a) What can we unambiguously determine about the atmospheres of exoplanets by observing their transmission spectra?

   (b) Is the information nature provides us with in the form of the planetary spectra sufficient to *uniquely* characterize the atmospheric composition of exoplanets?

   (c) What is the required spectral coverage and spectral resolution for a unique characterization?

2. Characterizations of super-Earths:

   (a) What is the nature of the newly discovered class of super-Earth exoplanets?

   (b) How can we characterize super-Earth exoplanets with currently available instrumentation?

3. Evaluations of dedicated space telescope designs:

   (a) What designs of the science instrument on dedicated space telescopes are most effective for characterization the atmospheres of transiting exoplanets?

   (b) Given technological and cost constraints, what are the recommended wavelengths coverage and detector technologies for the dedicated space telescope concept EChO?

The research questions translate into the following research objectives:

1. Develop a Bayesian framework to infer the atmospheric compositions and presence of clouds and hazes directly from spectral observations of exoplanets.

2. Provide a conceptual understanding of which spectral features need to be observed to uniquely constrain the atmospheric composition.

3. Explore pathways for characterizations of super-Earths with currently available instrumentation and their limited spectral coverage. Characterize the atmospheric composition of GJ 1214b, the most observed super-Earth to date.

4. Develop an integrated method to assess alternative designs of the EChO science instrument for their performance in characterizing the atmospheres of exoplanets.

1.5 Thesis Overview

This thesis is divided into a method chapter describing the Bayesian framework for atmospheric retrieval (Chapter 2), three applications of the retrieval method (Chapters 3–5), a conclusions chapter summarizing the thesis contributions and an providing an outlook (Chapter 7).

In Chapter 2, I develop an atmospheric retrieval method based on Bayesian analysis to infer the atmospheric compositions and surface or cloud-top pressures from spectroscopic observations of exoplanets. The approach to infer constraints on atmospheric parameters is to compute their joint posterior probability distributions using the Markov Chain Monte Carlo technique in a parallel tempering scheme. A new atmospheric parameterization is introduced that is applicable to the most general scenario of an atmosphere in which the main constituents are not known a priori and clouds and hazes may be present. I introduce an Bayesian model comparison approach to rationally determine an appropriate model complexity for given data and which molecular species and types of aerosols are present in the atmosphere.

Chapter 3 identifies what can unambiguously be determined about the atmospheres of exoplanets from their transmission spectra by applying the retrieval method to synthetic super-Earth observations. A conceptual picture of which details in transmission spectra are essential for unique characterizations of well-mixed exoplanet at-

mospheres is provided. Our main finding is that a *unique* constraint of the mixing ratios of the atmospheric gases is possible if the observations capture both broadband transit depths in at least one absorption feature for each absorber and the slope and strength of the molecular Rayleigh scattering signature.

In Chapter 4, I present an approach to observationally distinguish between cloudy mini-Neptunes and water- or ice-rich based on the difference in the wing slopes of molecular absorption bands in their NIR transmission spectra. We suggest that the observational distinction can be achieved efficiently for super-Earths orbiting M-dwarfs by observing strong water absorption bands near the peak of the M-dwarf's photon flux spectrum ($\lambda \approx 1\,\mu$m) at moderate resolution ($R \sim 50 \ldots 100$).

In Chapter 5, I study conceptual design of the proposed Exoplanet Characterization Observatory (EChO) and address what spectral coverage is most favorable taking into account the results from chapter 2 as well as engineering aspects such as cooling requirements and reflectances of coatings for optical surfaces. I present a novel integrated design evaluation framework that simultaneously models the astrophysical signal and the engineering aspects of the EChO payload module to evaluate the expected science output of EChO as a function of the detector and instrument design parameters. The main findings are that optical surface materials with high reflectivity at short wavelengths are essential to accomplish the mission objectives. The extra costs of cryogenic cooling to enable transit observations beyond $\sim 11\,\mu$m appear not to be justifiable.

Chapter 6 summarizes the contributions of this thesis and provides an outlook on atmospheric characterization of exoplanets.

The majority of Chapters 2 and 3 are published in Benneke & Seager (2012). Chapter 4 is currently under review at *The Astrophysical Journal.* Chapter 5 is in preparation for submission.

Chapter 2

Bayesian Atmospheric Retrieval

2.1 Overview

This chapter describes a Bayesian atmospheric retrieval framework to infer the atmospheric compositions and properties of clouds and hazes directly from spectral observations of exoplanets. First, a *Bayesian model comparison* approach infers from the observational data which molecular species and types of aerosols are present in the atmosphere and what our confidence in their detections are. Based the model comparison results, a retrieval model with adequate complexity is then selected, and constraints on the mixing ratios of the atmospheric gases and cloud and haze properties are retrieved using *Bayesian parameter estimation.*

The Bayesian analysis is performed using the Markov Chain Monte Carlo (MCMC) or Nested Sampling method in conjunction with an atmospheric "forward" model that computes the atmospheric spectrum for a given atmospheric scenario. Our confidence in having detected a particular molecular gas or aerosol type is quantified by determining the Bayes factor between a model that consider the presence of the species and a less complex model that neglects its presence. Constraints on the atmospheric parameters are inferred by marginalizing the joint posterior probability distribution of the atmospheric parameters derived from the observational data.

2.2 Atmosphere Parameterization

We propose a parametric description of the atmosphere guided by the information available in exoplanet transmission spectra. Our approach is to treat the atmosphere near the terminator as a well-mixed, one-dimensional atmosphere and describe the unknown molecular composition, thickness, and albedo of this atmosphere by free parameters. The motivation for treating the atmosphere as well-mixed is to keep the number of parameters to a minimum to avoid overfitting of the sparse data available in the near future, while ensuring that all atmospheric properties that considerably affect the retrieval from the spectrum are described by free parameters. For atmospheres with a stratified composition, the retrieval method determines an altitude-averaged mixing ratio that best matches the observed transmission spectrum (Section 3.5.2).

The unknown temperature profile at the terminator presents a challenge. While the pressure dependence of the temperature profile has only a secondary effect on the transmission spectrum and can likely not be retrieved given that the molecular composition is unknown a priori, the temperature does affect the scale height and may affect the constraints on other parameters. Our approach is not to retrieve the temperature profile, but to account for the uncertainty introduced by the unknown temperature on the retrieved composition and surface pressure. We therefore introduce a free parameter for the planetary albedo and calculate the temperature profile consistent with the molecular composition and the planetary albedo for each model atmosphere. In the MCMC analysis, the albedo is then allowed to vary over the range of plausible planetary albedos. Marginalizing the posterior distribution over all albedo values allows us to account for the uncertainty of the composition and surface pressure introduced by the unknown albedo.

Our proposed model has the following free parameters.

2.2.1 Volume mixing ratios of atmospheric constituents

We parameterize the composition of the atmosphere by the volume mixing ratios of all plausibly present molecular species. The volume mixing ratio X_i (or equivalently

the mole fraction) is defined as the number density of the constituent n_i divided by the total number density of all constituents in the gas mixture n_{tot}. No assumptions on the elemental composition, chemistry, or formation and evolution arguments are made. In contrast to the work on hot Jupiters by Madhusudhan & Seager (2009), we cannot assume a hydrogen-dominated atmosphere. We therefore reparameterize the mixing ratios with the centered-log-ratio transformations described in Section 2.4.3.2. The transformation ensures that all molecular species are treated equally and no modification is required when applying the retrieval method to atmospheres with different main constituents.

2.2.2 Surface or cloud deck pressure

We introduce the "surface" pressure $P_{\rm surf}$ as a free parameter, where the surface is either the ground or an opaque cloud deck. Solid surfaces and opaque cloud decks have the same effect on the transmission spectrum and we cannot discriminate between them. Our parameterization of the surface is applicable for rocky planets with a thin atmosphere as well as planets with a thick gas envelope. For thick atmosphere, for which there is no surface affecting the transmission spectrum, the inference of the surface pressure parameter provides a lower bound on the thickness of the cloud-free part of the atmosphere.

2.2.3 Planet-to-star radius ratio parameter

We define the planet-to-star radius ratio parameter, $R_{P,10}/R_*$, as the planetary radius at the 10 mbar pressure level, $R_{P,10}$, divided by the radius of the star R_*. Our approach to define the planetary radius at a fixed pressure level rather than at the surface avoids degeneracy between the planetary radius and the surface pressure for optically thick atmospheres for which the surface pressure cannot be constrained. It enables us to perform the retrieval for all types of planets without knowing a priori whether or not the planet has a surface. For planets with a surface pressure lower than 10 mbar, we still model an atmosphere down to the 10 mbar level and consider layers at pressure

levels with $P > P_{\rm surf}$ to be opaque.

2.2.4 Planetary albedo

While the goal is not to infer the planetary albedo, A_p, we wish to account for the uncertainty in the retrieved mixing ratios and surface pressure introduced by the unknown planetary albedo and equilibrium temperature. We therefore define the albedo as a free-floating parameter and assign a prior to the albedo parameter that reflects our ignorance of the albedo.

2.2.5 Fixed input parameters

Additional input parameters that are fixed in this study are the radius of the star, R_*, the planetary mass known from radial velocity measurements, M_p, and the semi-major axis of the planet's orbit, a_p. The effect of the uncertainties associated with these parameters on the retrieval results may be accounted for by letting the parameters float and assigning them a prior distribution.

2.3 Atmospheric "Forward" Model

The objective of the atmospheric "forward" model is to generate transmission spectra for a wide range of different atmospheric compositions and thicknesses. Given a set of atmospheric parameters (Section 2.2), our model uses line-by-line radiative transfer in local thermodynamic equilibrium, hydrostatic equilibrium, and a temperature profile consistent with the molecular composition to determine the transmission spectrum. The output of each model run is a high-spectral resolution transmission spectrum as well as simulated instrument outputs given the response functions of the instrument channels used in the observations. To obtain convergence of the posterior probability distribution in the MCMC inference, the model must efficiently generate $\sim 10^5$ atmospheric model spectra.

2.3.1 Opacities

2.3.1.1 Molecular absorption

We determine the monochromatic molecular absorption cross sections from the HITRAN database (Rothman et al., 2009) below 800 K. At temperatures higher than 800K we account for the high-temperature transitions of the gases H_2O, CO_2, and CO using the HITEMP database (Rothman et al., 2010). We account for H_2-H_2 collision-induced absorption using opacities from Borysow (2002).

To speed up the evaluation of a large number of atmospheric models, we first determine the wavelength-dependent molecular cross sections for each of the considered molecular species on a temperature and log-pressure grid and then interpolate the cross section for the required conditions. In the upper atmosphere, spectral lines become increasingly narrow, requiring a very high spectral resolution to exactly capture the shapes of the thin Doppler-broadened lines (Goody & Yung, 1995). Instead of ensuring that each line shape at low pressure is represented exactly, we choose an appropriate spectral resolution for the line-by-line simulation by ensuring that the simulated observations are not altered by more than 1% of the observational error-bar when the spectral resolution is doubled or quadrupled. While there are many methods proposed in the literature to reduce the computation time (e.g., correlated-k methods and band-models; Goody & Yung, 1995), the accuracy of such methods is hard to assess when the atmospheric composition is completely unknown a priori.

2.3.1.2 Rayleigh scattering

The Rayleigh scattering cross section, $\sigma_{R,i}$, for a molecular species i can be expressed in cgs units as

$$\sigma_{R,i}(\nu) = \frac{24\pi\nu^4}{N^2}\left(\frac{n_\nu^2 - 1}{n_\nu^2 + 2}\right)^2 F_{k,i}(\nu) \tag{2.1}$$

where ν is the wavenumber in cm^{-1}, N is the number density in , n_ν is the refractive index of the gas at the wavenumber ν, and $F_{k,i}(\nu)$ is the King correction factor. The scattering cross section of the gas mixture $\sigma_R(\nu) = \sum X_i \sigma_{R,i}(\nu)$ is the

weighted average from all major atmospheric constituents. The refractive indices and King correction factor functions of N_2, CO, CO_2, CH_4, and N_2O are taken from Sneep & Ubachs (2005), while the refractive index for H_2O is taken from Schiebener et al. (1990).

2.3.1.3 Clouds

Our model accounts for the potential presence of an opaque cloud deck whose upper surface's altitude is described by a free retrieval parameter. We assume a wavelength-independent, sharp cutoff of grazing light beams at the upper end of the cloud deck. The assumption of a sharp cutoff reasonably captures the effects of typical condensation cloud layers because, at ultra-violet to near-infrared wavelengths, such cloud layers become opaque on length-scales that are small compared to the uncertainty in the radius measurements probed by the transit observation. The motivation behind modeling the clouds as a sharp cutoff of grazing light beams is to obtain a zeroth order model capturing the trends of clouds on the transmission spectrum while using only one free parameter for cloudsin the retrieval.

2.3.2 Temperature-Pressure Profile

We use the analytical description for irradiated planetary atmospheres by Guillot (2010) with convective adjustments to approximate a temperature profile that is self-consistent with the atmospheric opacities and Bond albedo of each model atmosphere. The motivation behind this gray-atmosphere approach is that (1) its computational efficiency allows us to obtain temperature-pressure profiles consistent with the molecular composition for a large number of model atmospheres and (2) the uncertainties in the atmospheric temperature are dominated by the uncertainties in the albedo rather than model errors.

The Guillot (2010) model describes the horizontally-averaged temperature profile $\overline{T}$ as a function of optical depth, τ, by

$$\overline{T^4} = \frac{3T_{int}^4}{4}\left\{\frac{2}{3}+\tau\right\} + \frac{3T_{eq}^4}{4}\left\{\frac{2}{3}+\frac{2}{3\gamma}\left[1+\left(\frac{\gamma\tau}{2}-1\right)e^{-\gamma\tau}\right]+\frac{2\gamma}{3}\left(1-\frac{\tau^2}{2}\right)E_2\left(\gamma\tau\right)\right\}, \tag{2.2}$$

where $T_{\rm eq}$ is the planet's equilibrium temperature, $T_{\rm int}$ parameterizes the internal luminosity of the planet (set to 0 in this work), and γ is the ratio of the mean visible and thermal opacity and therefore parameterizes the deposition of stellar radiation in the atmosphere. We determine the mean opacities at visible and thermal wavelengths by averaging the line-by-line opacities weighted by the black body intensity at the effective star temperature and at the planet's equilibrium temperature, respectively.

Given a composition of the model atmosphere and the planetary albedo, we iteratively determine a solution that is self-consistent with the molecular opacities and in agreement with radiative and hydrostatic equilibrium. In the process, we check for the onset of convective instabilities ($-\frac{dT}{dz} > \Gamma = \frac{g}{C_p}$) delimiting the transition to the convective layer. For the specific heat capacity C_p, we assume that the molecular constituents of the atmosphere are ideal gases. In the convective regime, we adopt the adiabatic temperature profile. Our requirement to run a large number of models currently does not allow us to explicitly account for scattering and re-radiation of a solid surface or clouds in the calculation of the temperature profile.

2.3.3 Transmission Model

The atmospheric transmission spectrum of an extrasolar planet can be observed when the planet passes in front of its host star. During this transit event, some of the star's light passes through the optically thin part of the atmosphere, leading to excess absorption at the wavelength at which molecular absorption or scattering is strong. We model the transmission spectrum following the geometry described by Brown (2001). Given the planetary radius parameter,$R_{P,10}$, and the surface pressure parameter (Section 2.2), we calculate the radius at the surface. Below this surface radius, we represent the planet as an opaque disk. Above the surface radius, we calculate

the slant optical depth $\tau(b)$ as a function of the impact parameter b by integrating the opacity through the planet's atmosphere along the observer's line of sight. We account for extinction due to molecular absorption and Rayleigh scattering. Light that is scattered out of the line of sight is assumed not to arrive at the observer. We then integrate over the entire annulus of the atmosphere to determine the total absorption of stellar flux as a function of wavelength. To assess the fit between the observations and the model spectrum for a given set of input retrieval parameters, we integrate the transmission spectrum over the response functions of the individual instrument channels used in the observations. These simulated instrument outputs serve in the MCMC method to evaluate the jump probability as described in the next section.

2.4 Atmospheric Retrieval

Atmospheric retrieval aims at solving the inverse problem of atmospheric "forward" modeling: "Given an observed planetary spectrum, what are the properties of the planetary atmosphere?" The atmospheric retrieval problem can be solved using *Bayesian parameter estimation* by first choosing a retrieval model that defines the hypothesis space in the form of a set of atmospheric parameters and then deriving constraints on those parameters.

In choosing the atmospheric retrieval model, however, questions arise as to how much complexity and how many free parameters should be included in the retrieval model. In this work, we introduce *Bayesian model comparison* to determine which molecular gases and types of aerosols can be inferred from the data and need to be included in the analysis. The approach enables us to rationally adapt the complexity of the retrieval model to the available data. Exquisite observational data with high signal-to-noise ratio (S/N) and high spectral resolution, as are currently only available for solar system planets, allow the inference of the detailed abundance profiles of the molecular species, the temperature structure, and the presence of particles in the atmospheres. At lower S/N and sparse spectral coverage, however, complex models

with large numbers of free parameters would overfit the available data and introduce strong degeneracies. It is therefore required to reduce the number of free parameters.

2.4.1 Bayesian Estimation of Atmospheric Parameters

An atmospheric retrieval model M_i in our Bayesian framework is defined as a set of atmospheric parameters $\boldsymbol{\theta} = [\theta_1, \ldots, \theta_n]$ and their prior probability distribution $\pi(\boldsymbol{\theta}|M_i)$. The atmospheric parameters in the retrieval models considered in this work are the volume mixing ratios of the atmospheric gases, the cloud or haze-top pressure, and the radius at a reference pressure level. Since we generally have little prior knowledge of the state of the exoplanetary atmosphere, we assign non-informative priors to the atmospheric parameters (Section 2.4.3)

Given an observational data set $\boldsymbol{D}$, we can then infer the constraints on the atmospheric parameters in the retrieval model by computing their joint posterior probability distribution $p(\boldsymbol{\theta}|M_i, \boldsymbol{D})$ (Benneke & Seager, 2012). Using Bayes' Law, we write the posterior distribution of the atmospheric parameters as

$$p(\boldsymbol{\theta}|M_i, \boldsymbol{D}) = \frac{\pi(\boldsymbol{\theta}|M_i)\mathcal{L}(\boldsymbol{D}|M_i, \boldsymbol{\theta})}{\mathcal{Z}(\boldsymbol{D}|M_i)}, \tag{2.3}$$

where $\mathcal{L}(\boldsymbol{D}|M_i, \boldsymbol{\theta})$ is the likelihood function and $\mathcal{Z}(\boldsymbol{D}|M_i)$ is the Bayesian evidence of the model M_i. The likelihood function $\mathcal{L}(\boldsymbol{D}|M_i, \boldsymbol{\theta})$ is the probability of observing the data $\boldsymbol{D}$, given that the atmospheric parameters are $\boldsymbol{\theta}$. The likelihood function is modeled using the atmospheric "forward" model and estimates of the observational uncertainty of the spectral data points. For independent Gaussian errors in the spectral observations, the likelihood function is

$$\mathcal{L}(\boldsymbol{D}|M_i, \boldsymbol{\theta}) = \prod_{k=1}^{N} \frac{1}{\sigma_k\sqrt{2\pi}} \exp\left\{-\frac{[D_{k,obs} - D_{k,model}(\boldsymbol{\theta})]^2}{2\sigma_k^2}\right\}, \tag{2.4}$$

where $D_{k,obs}$ is the k-th observational data point in the spectrum, $D_{k,model}(\boldsymbol{\theta})$ is the model prediction for the k-th data point given a set of atmospheric parameters $\boldsymbol{\theta}$, and$N$ is the total number of data points in the observed spectrum. The Bayesian

evidence is central to model comparison, but merely a normalization constant in Equation (2.3).

2.4.2 Identification of Gases and Aerosols using Bayesian Model Comparison

One of the questions that arises when interpreting spectra of planetary atmospheres is which molecular species and aerosol types can be inferred from a given data set. Spectral signatures of molecular gases or aerosols are often hidden in the noisy observations of exoplanets. In addition, strong overlap between absorption features of different molecules and the lack of a flat continuum for thick atmospheres may further complicate the identification of individual gases.

Bayesian model comparison offers a rational way of determining which atmospheric species can be inferred from the data. *Bayesian model comparison* has widely been used in cosmology.

In our atmospheric retrieval application, we quantify our confidence in having detected the presence of a particular atmospheric constituent m by computing the posterior odds ratio (or Bayes factor) between a simpler retrieval model that neglect the presence of the species m and a more complex retrieval model that includes an additional parameter to describe the abundances of the constituent m. If the posterior odds ratio is strongly in favor of the more complex model, we can safely conclude that the atmospheric constituent is present.

In practice, the required comparisons for all relevant atmospheric constituents are achieved by computing the Bayesian evidence for one retrieval model that covers the full prior hypothesis space and comparing it to a list of retrieval models for which individual molecular species and types of aerosols were removed from the prior hypothesis space. The approach ensures that a high confidence in the presence of a particular atmospheric constituent is reported only if no other constituent in the prior hypothesis space can have resulted in the observed data.

2.4.2.1 Bayesian evidence

The quantity central to all Bayesian model comparisons is the Bayesian evidence

$$\mathcal{Z}\left(\boldsymbol{D}|M_i\right) = \int_{all\,\boldsymbol{\theta}} \pi(\boldsymbol{\theta}|M_i)\,\mathcal{L}\left(\boldsymbol{D}|M_i,\boldsymbol{\theta}\right)\,d^n\boldsymbol{\theta}. \tag{2.5}$$

The Bayesian evidence quantifies the adequacy of a retrieval model M_i, specified by a set of atmospheric parameters $\boldsymbol{\theta}$ and their prior probability distribution $\pi(\boldsymbol{\theta}|M_i)$, in the light of the data $\boldsymbol{D}$. Comparing the Bayesian evidences of alternative retrieval models with parameterizations of lower and higher complexities enables one to assess which atmospheric constituents and effects are important and which model complexities ought to be removed.

The underlying idea of the Bayesian model comparison is thereby that additional complexity of the parameter space ought to be avoided whenever a simpler model provides an adequate representation of the data. While it is obvious that a best fit of a retrieval model with more free parameters will always be better (or at least as good as) the best fit of a model with fewer parameters, the Bayesian evidence only favors the more complex model if the improvement in the best fit due to additional parameters is large enough to overcome the Occam penalty for the more complex model parameter space.

2.4.2.2 Posterior odds ratio / Bayes factor

Using Bayes' law we can express the posterior odds ratio between two alternative models $\mathrm{M}_{\text{"m present"}}$ and as $\mathrm{M}_{\text{"m not present"}}$

$$\frac{p\left(\mathrm{M}_{\text{"m present"}}|\boldsymbol{D}\right)}{p\left(\mathrm{M}_{\text{"m not present"}}|\boldsymbol{D}\right)} = B_m \frac{p\left(\mathrm{M}_{\text{"m present"}}\right)}{p\left(M_{\text{"m not present"}}\right)} \tag{2.6}$$

where the Bayes factor B_m is the ratio of the model's Bayesian evidences

$$B_m = \frac{\mathcal{Z}\left(\boldsymbol{D}|M_{m\,\text{present}}\right)}{\mathcal{Z}\left(\boldsymbol{D}|M_{\text{"m not present"}}\right)}, \tag{2.7}$$

and $p\left(\mathrm{M}_{\text{"m present"}}\right)/p\left(M_{\text{"m not present"}}\right)$ is the prior odds ratio, which we assume to

be 1 in the absence of prior information.

The posterior probability for the present species m is

$$p(\text{“}m \text{ is present”}|\boldsymbol{D}) = \frac{B_m}{1+B_m}. \tag{2.8}$$

The Bayes factor B_m plays a pivotal role in a Bayesian model comparison. A value of $B_m > 1$ means that the data provide support in favor of the presence of the atmospheric constituent m. Bayes factors are generally interpreted against the Jeffrey scale (ref). Values of the odds of 3:1, 12:1, and 150:1 represent weak, moderate, and strong support in favor of the presence of additional molecular gas or aerosol species (Table 2.1).

2.4.2.3 Calibration between Bayesian and Frequentist Detections

The increase in availability of computational resources over the last decades has led to a widespread of Bayesian techniques in the analysis of astrophysical observations. Parameter estimation problems are frequently solved in a Bayesian framework using Markov Chain Monte Carlo (MCMC) techniques. Yet, the significance of detections of atmospheric absorption features is generally still reported in terms of the frequentist measures of confidence such as the p-value or the “sigma”-significance (see Section). As a result, many scientists are accustomed to the interpretation of sigma significance, but not Bayes factors.

A useful calibration between the Bayes factor and the frequentist measures of confidence is provided by the expression

$$B_m \leq -\frac{1}{\mathrm{e}\cdot\rho\cdot\ln\rho}, \tag{2.9}$$

where e is the exponential of one and ρ is the p-value(Sellke et al., 2001). The p-value, in turn, can be related to the sigma significance n_σ using the expression

$$\rho = 1 - \mathrm{erf}\left(\frac{n_\sigma}{\sqrt{2}}\right), \tag{2.10}$$

p-value	B_m	$\ln B_m$	"sigma"	interpretation
0.05	2.5	0.9	2.0σ	
0.04	2.9	1.0	2.1σ	"weak" detection
0.01	8.0	2.1	2.6σ	
0.006	12	2.5	2.7σ	"moderate" detection
0.003	21	3.0	3.0σ	
0.001	53	4.0	3.3σ	
0.0003	150	5.0	3.6σ	"strong" detection
$6 \cdot 10^{-7}$	43000	11	5.0σ	

Table 2.1: Translation table between frequentist significance values (p-values and "sigma" significance) and the Bayes factor (B_m) in favor of the more complex model. Adopted from Trotta (2008). A Bayes factor of $B_m = 150$ for the more complex model, for example, would correspond to detection significance of at least 3.6σ.

where erf is the error function. Representative values for a range of confidence values are listed in Table 2.1. Equation (2.9) presents an upper bound on the Bayes factor, e.g., a Bayesian factor $B_m = 21$ corresponds at least to a 3.0σ detection. Equation (2.9) is valid for $\rho < \mathrm{e}^{-1}$ and under the assumption of a mild principle of indifference as to the value of the added parameter in the more complex model (Sellke et al., 2001).

2.4.3 Bayesian Priors

2.4.3.1 Ignorance Priors

One challenge in atmospheric retrieval is that even for the most simple atmospheric parameterizations, some parameters describing the composition and state of the atmosphere might not be constrained well by the observations. In this regime, it is important to choose an appropriate, non-informative prior probability distribution on the parameters. One advantage of the Bayesian approach over traditional frequentist approaches is that we can explicitly state our choice of the prior probability distribution. Many approaches, e.g., constant-$\Delta\chi^2$ boundaries, usually implicitly assume a uniform prior. While in many cases the uniform prior seems like a reasonable choice, it is worth noting that the uniform prior is variant under reparameterization. For example, a uniform prior for $\log(x)$ will not be a uniform prior for x (Gelman et al.,

2003), therefore the obtained results can depend on the choice of parameterization.

In this work, we use a uniform prior on the radius ratio parameter, $(R_p/R_*)_{10}$, and the planetary albedo, A. The surface pressure, P_{surf}, is a "scale parameter" for which we do not know the order of magnitude a priori. We therefore choose a Jeffrey prior for the surface pressure, i.e., a uniform prior for $\log(P_{\text{surf}})$. Since an infinite surface pressure may agree with the observational data in the same way a sufficiently high finite value does, the posterior distribution can remain unnormalizable unless a normalizable prior distribution is chosen. To ensure a normalizable posterior, we set an upper bound on the prior at $p = 100\,\text{bar}$. Higher surface pressures are not considered because atmospheres of plausible compositions will be optically thick to the grazing star light at higher pressure levels.

The mixing ratios of the molecular gases are also scale parameters, suggesting that the usage of a Jeffrey prior for each of the mixing ratios would be appropriate. The constraint that the mixing ratios must add up to unity, however, prevents the assignment of a Jeffrey prior for the individual mixing ratio. We therefore introduce a reparameterization as discussed in the following section.

2.4.3.2 Centered-Log-Ratio Transformation for Mixing Ratios of Atmospheric Constituents

Since the mixing ratios of the molecular species in the atmosphere present parts from a whole, they must satisfy the constraints

$$0 < X_i < 1 \,\text{and} \tag{2.11}$$

$$\sum_{i=1}^{n} X_i = 1, \tag{2.12}$$

where n is the number of gases in the atmosphere. For the statistical analysis of the mixing ratios, it is important to recognize that the sample space of a composition is *not* the full Euclidean space $\mathbb{R}^n$, for which most statistical tools were developed, but only the restricted $(n-1)$-dimensional space formally known as the simplex of n parts, $\mathbb{S}^n$.

The simplex includes only sets of mixing ratios for which the components sum up to 1. As a result, the total number of free parameters describing the molecular composition is reduced by one. The mixing ratio of the nth species X_n can be calculated directly from the mixing ratios $X_1 ... X_{n-1}$.

In this subsection, we present a reparameterization for the mixing ratios that allows for efficient sampling of the full simplex with MCMC, while ensuring that all n molecular species may range across the complete detectable range, e.g., $10^{-12} < X_i < 1$, with a non-zero prior probability, and that the results are permutation invariant, i.e., independent of which molecule was chosen to be the nth species.

Previous work on atmospheric retrieval implicitly accounted for the constraints in Equations (2.11) and (2.12) by using free parameters only for mixing ratios of the minor atmospheric gases and assuming that the remainder of the atmosphere is filled with the a-priori known main constituent. This approach is feasible for the inference of gas mixing ratios in hot Jupiters and Solar System planets because the main constituents of the atmospheres, i.e., H_2, are known a priori. In a Bayesian retrieval approach, in which we do not know the main constituent of the atmosphere, however, parameterizing the abundances of minor species and assuming a main species is unfavorable. Assigning a Jeffrey prior, i.e. a uniform prior on the logarithmic scale, for $n - 1$ mixing ratios leads to a highly asymmetric prior that favors a high abundance of the nth species (Figure 2-1(top)). In addition, in cases with a low abundance of the nth species, we find that the asymmetric parameterization leads to serious convergence problems in the numerical posterior simulation with MCMC.

To circumvent the drawbacks of highly asymmetric priors in the interpretation of the results as well as the numerical convergence problems due a highly asymmetric parameterization, we use the centered-log-ratio transformation to reparameterize the composition (Aitchison, 1986; Pawlowsky-Glahn & Egozcue, 2006). The centered-log-ratio transformation is commonly used in geology and social sciences for the statistical analysis of compositional data (e.g., Pawlowsky-Glahn & Egozcue, 2006), we find that it also enables the MCMC technique to efficiently explore the posterior distribution of the atmospheric composition across the complete simplicial sample space.

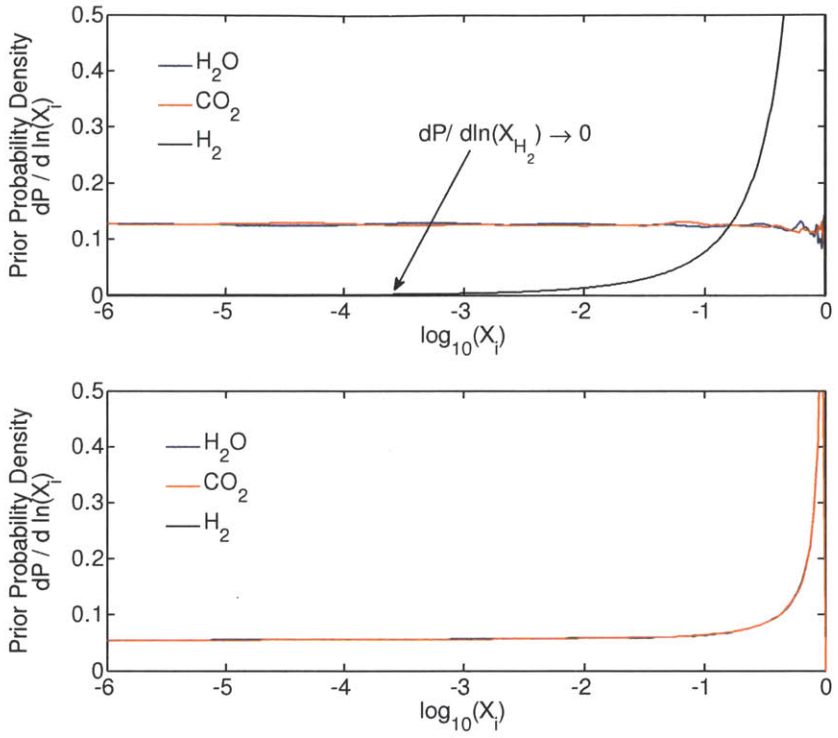

Figure 2-1: Marginalized prior probability distribution for the mixing ratios in a mixture of three gases. The upper panel illustrates the prior probabilities for a parameterization in which the gases H_2O and CO_2 are described by free parameters and H_2 is set to fill the remainder of the atmosphere. Assigning a Jeffrey prior, i.e., $dP/d\ln(X_i) = \text{const}$ to all gases except one leads to a description that is permutation variant and strongly favors compositions with a high abundance of the remaining gas. Compositions with low amount of H_2 are excluded by the prior because the prior probability rapidly approaches zero for $X_{H_2} < 1\%$. The bottom panel shows the prior probabilities for the mixing ratios using the center-log-ratio transformation introduced in this work. The prior probability for all gases in the mixture is identical, thereby providing permutation-invariant results. The prior probability distribution of *all* gases approaches the Jeffrey prior at mixing ratios below ~20%, and is, therefore, highly favorable for scale parameters. The divergence to infinity is only of theoretical nature. Once the signature of one gas is detected in the spectrum, the posterior probability of all other gases at $X_i = 100\%$ will go to zero.

For a mixture of n gases, the centered-log-ratio transformation of the i-th molecular species is defined as

$$\xi_i = \mathrm{clr}\,(X_i) = \ln \frac{X_i}{g(\boldsymbol{x})}, \tag{2.13}$$

where

$$g(\boldsymbol{x}) = \left(\prod_{j=1}^{n} X_i\right)^{1/n} = \exp\left(\frac{1}{n}\sum_{j=1}^{n} \ln X_i\right) \tag{2.14}$$

is the geometric mean of all mixing ratios $X_1 ... X_n$.

Each of the compositional parameters ξ_i may range between $-\infty$ and $+\infty$, where the limit $\xi_i \to -\infty$ indicates that ith species is of extremely low abundance with respect to the other molecular species, while $\xi_i \to +\infty$ indicates that the i-th species is abundant in the atmosphere. The composition $\boldsymbol{\xi} = [0, 0, \ldots, 0]$describes the center of the simplex at which all molecular species are equally abundant (Figure 2-2). The only constraints on the transformed compositional parameters is $\sum_{i=1}^{n} \xi_i = 0$.

A fully permutation-invariant description is obtained by using the centered-log-ratio transformed mixing ratios $\xi_1 \ldots \xi_{n-1}$ as the free parameters and assigning a uniform prior for all vectors in the ξ-space for which $X_i > 10^{-12}$ for all $i = 1 \ldots n$. As the distances in the sample space spanned by $\xi_1 \ldots \xi_{n-1}$ scale with the differences in $\ln X_i$ for small mixing ratios, the MCMC can efficiently sample the complete space, even if the mixing ratios vary over several orders of magnitude.When transformed back into the Euclidean space of the mixing ratios, X_i, we obtain prior probabilities for each of the mixing ratios that have the properties of a Jeffrey prior below $X_i \lesssim 20\%$ (Figure 2-2). The properties of a Jeffrey prior are highly favorable for scale parameters such as the mixing ratios. The increase in the prior toward mixing ratios $\gtrsim 0.1$ is a direct consequence of the fact that one or more molecular species in the atmosphere inevitably needs to have a significant abundance. The divergence toward infinity at $\log X_i$ is of no practical relevance. If a single molecular species is detectable in the spectrum, then mixing ratios of 100% are excluded for all other species by the data .

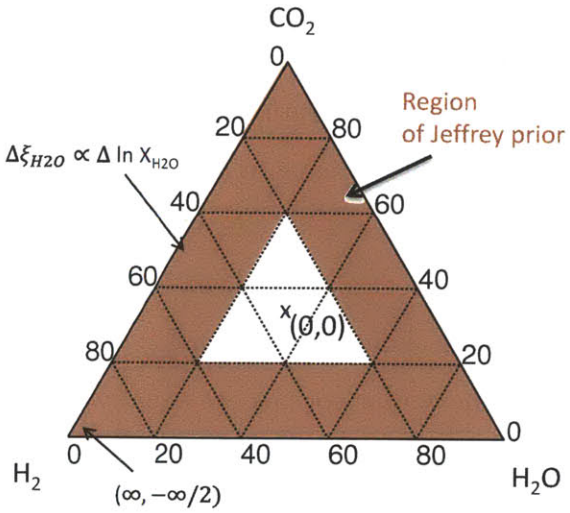

Figure 2-2: Simplicial sample space for a mixture of three gases illustrated in a ternary diagram. Using the centered-log-ratio transformation for the mixing ratios of the atmospheric gases, we obtain a symmetric parameterization of the composition in which all molecular species are treated equally, while simultaneously ensuring that the sum of the mixing ratios is unity. The zero point of the transformed mixing ratios, ξ_i, is at the center of the simplex. Toward the edges of the sample space, i.e., for low mixing ratios of one or more gases, the differences in the transformed mixing ratio, ξ_i, scale with $\ln(X_i)$. The scaling provides a region in which the prior probability $dP/d\ln(X_i)$ remains constant (red) and allows the MCMC to efficiently sample down to exponentially small mixing ratios for all molecular species.

2.5 Numerical Methods for Atmospheric Retrieval

Two numerical methods were implemented in this work to perform the computations required for the Bayesian inference. The joint posterior probability of the retrieval parameters can obtained using either the Markov Chain Monte Carlo (MCMC) technique (Section 2.5.1) or nested sampling (Section 2.5.2). The MCMC technique is generally more efficient for constrained problem with a single-modal posterior distribution. MCMC, however, does not provide the Bayesian evidence of retrieval models and, thus, does not allow us to determine our confidence in detections of molecular gases and aerosols in statistically robust way. The nested sampling algorithm is arguably the most efficient algorithm to compute the Bayesian evidence necessary for Bayesian parameter estimation. Its advantages for Bayesian parameter estimation are that it does get trapped in local minima, but traverses the complete multi-dimensional parameter space searching for regions with good fit to the data.

2.5.1 Markov Chain Monte Carlo (MCMC)

The MCMC technique using the Metropolis-Hastings algorithm offers an efficient method of performing the integration necessary for the Bayesian analysis in Equation (??) (Gelman et al., 2003). It has been applied to several other astronomical data sets and problems (e.g., Ford, 2005, and references therein). We use the MCMC technique to determine the best estimates and Bayesian credible regions for the atmospheric parameters by computing the joint posterior probability distribution of the atmospheric parameters. The uncertainty of individual parameters introduced by complicated, non-Gaussian correlations with other parameters is accounted for in a straightforward way by marginalizing the joint posterior distribution over all remaining parameters.

The goal of our MCMC simulation is to generate a chain of states, i.e., a chain of sets of atmospheric parameters $\boldsymbol{\theta}$, that are sampled from the desired posterior probability distribution $p(\boldsymbol{\theta}|\boldsymbol{D})$. Using the Metropolis-Hastings algorithm, such a chain can be computed by specifying an initial set of parameter values, $\boldsymbol{\theta}_0$, and a

proposal distribution, $p(\boldsymbol{\theta}'|\boldsymbol{\theta}_n)$. At each iteration, a new proposal state $\boldsymbol{\theta}'$ is generated and the fit between the transit observations and the model transmission spectrum for the proposed set of atmospheric parameters is computed. The new proposal state $\boldsymbol{\theta}'$ is then randomly accepted or rejected with a probability that depends on (1) the difference between the χ^2-fits of the previous state and the proposal state and (2) the difference in the prior probability between the previous state and the prior state. A proposal state that leads to an improvement in the χ^2-fit and a higher prior probability compared to the previous state is always accepted. A proposal state that leads to a worse fit or a lower prior probability is accepted according to the jump probability

$$p(\boldsymbol{\theta}_{n+1} = \boldsymbol{\theta}') = \exp\left\{-\frac{1}{2}\left[\chi^2(\boldsymbol{\theta}') - \chi^2(\boldsymbol{\theta}_n)\right]\right\} \cdot \frac{p(\boldsymbol{\theta}')}{p(\boldsymbol{\theta}_n)}, \tag{2.15}$$

where we assumed Gaussian uncertainty in the observations and

$$\chi^2 = \sum_{k=1}^{n_{\text{obs}}} \frac{(D_{k,\text{model}} - D_{k,\text{obs}})^2}{\sigma_k^2} \tag{2.16}$$

is the measure of fit between the observed transit depths, $D_{k,\text{obs}}$, and the model output, $D_{k,\text{model}}$. The probabilities $p(\boldsymbol{\theta}_n)$ and $p(\boldsymbol{\theta}')$ are the prior probabilities of the previous and the proposal state. If the proposal state is rejected, the previous state will be repeated in the chain.

2.5.1.1 Parallel Tempering

A simple Metropolis-Hastings MCMC algorithm can fail to fully explore the target probability distribution, especially if the distribution is multi-modal with widely separated peaks. The algorithm can get trapped in a local mode and miss other regions of the parameter space that contain significant probability. The trapping problem is expected for atmospheric retrieval of extrasolar planets for which only very sparse data are available. The challenge faced is similar to the one encountered in finding the global minimum of a nonlinear function.

We address the challenge of a potentially multi-modal probability distribution by

adopting a parallel tempering scheme (Gregory, 2005) for our atmospheric retrieval method. In parallel tempering, multiple copies of the MCMC simulation are run in parallel, each using a different "temperature" parameter, β. The tempering distributions are described by

$$p(\boldsymbol{\theta}|D,\beta) = p(\boldsymbol{\theta})p(D|\boldsymbol{\theta})^{\beta} \tag{2.17}$$

One of the simulated distributions, the one for which we choose $\beta = 1$, is the desired target distribution. The other simulations correspond to a ladder of distributions at higher temperature with β ranging between 0 and 1. For $\beta \ll 1$, the simulated distribution is much flatter and a wide range of the parameter space is explored. Random swaps of the parameter states between adjacent simulations in the ladder allow for an exchange of information across the different chains. In the higher temperature distributions ($\beta \ll 1$), radically new configurations are explored, while lower temperature distributions ($\beta \sim 1$) allow for the detailed exploration of new configurations and local modes.

The final inference on atmospheric parameters is based on samples drawn from the target probability distribution ($\beta = 1$) only. To probe the convergence, we perform multiple independent parallel-tempering simulations of the target probability distribution with starting points dispersed throughout the entire parameter space.

2.5.2 Nested Sampling for Atmospheric Retrieval

We employ the multimodal nested sampling algorithm (MultiNest) to efficiently compute the Bayesian evidences of alternative retrieval models (Skilling, 2004; Feroz & Hobson, 2008; Feroz et al., 2009). The joint posterior probability distribution of the atmospheric parameters for a given retrieval model are obtained as a by-product. The MultiNest algorithm was developed as a Bayesian inference tool for cosmology and particle physics, and we find that it can provide substantial advantages for atmospheric retrieval over techniques based on Markov Chain Monte Carlo (MCMC).

2.5.2.1 Nested Sampling versus MCMC

Parameter estimations in many astrophysical contexts are typically performed using the MCMC technique with the Metropolis-Hastings algorithm or its variants such as the Gibbs sampler. The two main disadvantages of the MCMC techniques are, however, that MCMC does not directly provide the Bayesian evidence for comparing retrieval models of different complexities, and that MCMC becomes inefficient when sampling from a posterior distribution with multiple separate modes or elongated curving degeneracies. In Benneke & Seager (2012), we were able to search for separated modes in the posterior distribution using the parallel tempering MCMC technique. Calculating the Bayesian evidences for Bayesian model comparisons, however, requires a second step, such as a Restricted Monte Carlo (RMC) integration. Restricted Monte Carlo (RMC) becomes extremely inefficient, however, when the joint posterior distribution shows strongly curved correlations, such as those encountered in atmospheric retrieval problems.

2.5.2.2 The Nested Sampling Algorithm

Nested sampling is an alternative Monte Carlo technique for Bayesian inference. It enables one to efficiently compute the Bayesian evidence and provides the posterior distribution for parameter estimations as a by-product. A full discussion is provided in (Skilling, 2004; Feroz & Hobson, 2008). Here, we provide a brief description of the main ideas. For clarity, we do not explicitly state the model M_i and the data $\boldsymbol{D}$ because the calculation of the Bayesian evidence is conducted for each model and data set individually.

The basic idea behind nested sampling is to transform the multi-dimensional integral for the computation of the Bayesian evidence (Equation (??)) into the one-dimensional integral

$$\mathcal{Z} = \int_0^1 \mathcal{L}^*(V)\, dV. \tag{2.18}$$

The integration variable V in Equation (2.18) is defined as the "prior volume",

$$V\left(\mathcal{L}^*\right) = \int_{\mathcal{L}(\boldsymbol{\theta})>\mathcal{L}^*} \pi(\boldsymbol{\theta}) d^n\boldsymbol{\theta}. \tag{2.19}$$

The prior volume V as a function of $\mathcal{L}^*$ is the total prior probability mass contained within the iso-likelihood contour $\mathcal{L}\left(\boldsymbol{D}|M_i, \boldsymbol{\theta}\right) = \mathcal{L}^*$. It is a monotonically decreasing function of the likelihood limit $\mathcal{L}^*$ because the volume contained in the iso-likelihood contour decreases as $\mathcal{L}^*$ increases and the likelihood restriction become tighter. The extreme values are $V = 1$ for $\mathcal{L}^* = 0$, in which case the integration is performed over the entire prior parameter space, and $V = 0$ for $\mathcal{L}^* \to \infty$. The function $\mathcal{L}^*\left(V\right)$ in Equation 2.18 is the inverse function of the prior volume $V\left(\mathcal{L}^*\right)$ and is thus also monotonically decreasing.A graphical interpretation of the integration in Equation (2.18) is illustrated for a two-dimensional parameter space in Figure ??.

The Bayesian evidence in Equation 2.18 can be approximated using standard quadrature methods if the inverse function $\mathcal{L}^*\left(V\right)$ of Equation (2.19) can be evaluated at a sequence of values $0 \leqslant V_M < \ldots < V_i < \ldots < V_1 \leqslant 1$. Using the trapezium rule, we obtain

$$\mathcal{Z} = \sum_{i=1}^{M} w_i \mathcal{L}_i. \tag{2.20}$$

where $\mathcal{L}_i$ is the likelihood limit $\mathcal{L}^*\left(V_i\right)$ corresponding to V_i, the weights w_i are given by $w_i = \frac{1}{2}\left(V_{i-1} - V_{i+1}\right)$, and M is the number of values in the sequence.

In nested sampling a sequence of $\mathcal{L}^*\left(V_i\right)$ values is generated as follows. The algorithm is initialized by randomly drawing a user-specified number of "active samples" ($N \approx 50 \ldots 10000$) from the full prior probability distribution $\pi(\boldsymbol{\theta})$ and computing their likelihood $\mathcal{L}\left(\boldsymbol{\theta}\right)$ according to 2.4. These samples are distributed randomly across the full prior parameter space and the prior volume $V_0 = V\left(\mathcal{L}^* = 0\right)$ is 1. The first iteration is started by sorting the samples in order of their likelihood. The sample with the lowest likelihood $\mathcal{L}_1$, i.e. the sample with the worst fit to the data, is then removed and replaced by a new sample. The new sample is again drawn from the prior distribution, but subject to the constraint that the likelihood of the new sample is higher than $\mathcal{L}_1$. If necessary, the drawing of the new sample is repeated until a

sample is found with $\mathcal{L}(\boldsymbol{\theta}) > \mathcal{L}_1$. After the replacement, all active samples meet the condition $\mathcal{L}(\boldsymbol{\theta}) > \mathcal{L}_1$ and they are uniformly distributed within the iso-likelihood contour $\mathcal{L}^* = \mathcal{L}_1$. The new prior volume V_1 contained within the iso-likelihood contour $\mathcal{L}^* = \mathcal{L}_1$ can be written as $V_1 = t_1 V_0$, where the shrinkage ratio t_1 is a random number smaller than 1. The probability distribution of the shrinkage, $p(t_1)$, is the distribution for the largest of n samples drawn from a uniform distribution between 0 and 1. The distribution $p(t_1)$ describes the decrease in prior volume between subsequent iso-likelihood contours $\mathcal{L}^* = V_0$ and $\mathcal{L}^* = V_1$ in a probabilistic way because the active samples are uniformly distributed within the iso-likelihood contours.

In subsequent iterations, the process of replacing the sample with the lowest likelihood $\mathcal{L}_i$ is repeated, and the corresponding prior volume $V(\mathcal{L}_i)$ is repeatedly tightened. The nested sampling algorithm thus progresses through nested shells of iso-likelihood contours with continually decreasing prior volumes, until the regions of the highest likelihoods are localized. The prior volume $\mathrm{V_i}$ after iteration i can be approximated as

$$V_i = \exp(-i/N). \tag{2.21}$$

Equation (2.21) approximate the prior volume at iteration i because each value of t_i is independent and the mean and standard deviations of $\log(t)$ are $\mathrm{E}[\log(t)] = -1/N$ and $\sigma[\log(t)] = 1/N$, resulting in $\log(V_i) \approx \left(i \pm \sqrt{i}\right)/N$.

2.5.2.3 Simultaneous Ellipsoidal Nested Sampling

The main challenge in efficiently computing the Bayesian evidence is to efficiently generate random samples within the iso-likelihood contour $\mathcal{L}^* = \mathcal{L}_i$. If one continued to draw random samples from the full prior probability distribution $\pi(\boldsymbol{\theta})$ as in the first iteration, the chance of randomly finding one that is within the iso-likelihood contour $\mathcal{L}^* = \mathcal{L}_i$ would decrease exponentially as the likelihood limit $\mathcal{L}_i$ is raised.

The algorithm employed in this work uses the simultaneous ellipsoidal nested sampling method developed in Feroz et al. (2009). At each iteration, the full set of

active samples is partitioned according to local clustering and an optimum number of ellipsoids are constructed such that the union of the ellipsoidal volumes tightly encompasses all samples. At early iterations, a small number of large ellipsoids cover almost the entire prior parameter space. As the active sample become confined to the regions within tighter iso-likelihood contours, the ellipsoids encompass only the region(s) of high likelihood $\mathcal{L}(\boldsymbol{\theta})$. New random samples are drawn from within the ellipsoids, thus the random samples have a high likelihood $\mathcal{L}(\boldsymbol{\theta})$ with higher probability, resulting in a higher sample acceptance rate and higher efficiency of the nested sampling algorithms. The algorithm is robust to multimodal posterior distributions and elongated curving degeneracies, while remaining efficient for simpler distributions. Refer to Feroz et al. (2009) for a detailed description of the algorithm employed for partitioning and construction of the ellipsoids.

2.5.2.4 Numerical Uncertainty of Computed Results

The iterations are continued until the Bayesian evidence is determined to a specified precision $\Delta\mathcal{Z}$. In this work, we terminated once the logarithm of the evidence did not change by more than $\Delta(\log(\mathcal{Z})) = 0.01$. The final uncertainty can be estimated following Sivia & Skilling (2006) as

$$\log(\mathcal{Z}) \approx \log\left(\sum_{i=1}^{M} w_i \mathcal{L}_i\right) \pm \sqrt{\frac{\mathcal{H}}{N}}, \tag{2.22}$$

where $\mathcal{H}$ is the *information,* or *negative entropy,*

$$\mathcal{H} \approx \sum_{i=1}^{M} \frac{w_i \mathcal{L}_i}{\mathcal{Z}} \log\left(\frac{\mathcal{L}_i}{\mathcal{Z}}\right). \tag{2.23}$$

2.5.2.5 Parameter Estimation

Once the Bayesian evidence $\mathcal{Z}$ is determined, the joint posterior distribution of the atmospheric parameters can be constructed using all active and discarded samples that were generated during the nested sampling iterations. Each sample is assigned

a weight according to

$$W_i = \frac{w_i \mathcal{L}_i}{\mathcal{Z}}. \tag{2.24}$$

The weighted samples can be used to plot the posterior distributions and calculate the statistical measures such as the mean and covariances matrix.

2.6 Inputs

The primary inputs to the retrieval method presented here are spectral and/or photometric observations of the wavelength dependent transit depths during the primary transit, $(R_p/R_*)^2$. Accurate estimates of the observational error bars are of particular importance because they can significantly affect the constraints and conclusions made from the observations. Ideally, the spectral data would not be binned to reduce the apparent error bars. Binning of spectral data always leads to a loss of information and should only be done if is required to compensate for systematics.

The spectra from the primary transit can be augmented by secondary eclipse measurements constraining the planetary albedo (or the atmospheric temperature) by including the information in the prior probability distribution. An improved estimate of the temperature or planetary albedo can lead to improved constraints in all composition parameters. If no such observations are available, the retrieved uncertainties in the composition will fully account for the uncertainty in the planetary albedo.

2.7 Outputs

The output of the atmospheric retrieval is the posterior probability density distribution, $p(\boldsymbol{\theta}|M_i, \boldsymbol{D})$, of the retrieval parameters discussed in Section 2.2. This multidimensional distribution encodes our complete state of knowledge of the atmospheric parameters in the light of the available observations.. To illustrate our state of knowledge of a single parameter, we marginalize the posterior density distribution over all remaining parameters. For well-constrained parameters, one can summarize our

knowledge of the parameter in just a few numbers, i.e., the most likely estimates and a set of error-bars and correlation coefficients. Depending on the nature of the observational data, however, we may obtain a posterior distribution that is not well-described by single best estimate plus the uncertainty around this estimate. For example, a multi-modal distribution would be indicative of multiple possible solutions. Highly asymmetric posterior distributions or only one-sided bounds will be obtained if the observations constrain the parameter only in one direction.

We can also compute the constraints on atmospheric properties that do not serve as free parameters in our retrieval methods, such as the mean molecular mass, the total atmospheric mass above the surface, the mixing ratios by mass, or the elemental abundances. A set of the retrieval parameters introduced in Section 2.2 entirely describes the state of well-mixed, one-dimensional atmospheres. For each set of retrieval parameters in the chain obtained from the MCMC simulations, we can, therefore, compute the any other atmospheric property from the retrieval parameters. In this way, we obtain a new chain for the desired atmospheric property that, interpreted as a sample from the marginalized distribution of the atmospheric property, can be used to infer constraints on the atmospheric properties by comparing the distribution to the equivalently obtained prior distribution.

In this work, we present constraints on the mean molecular mass, total atmospheric mass above the cloud-deck/surface, and relative elemental abundances (Equations 10-12),

$$\mu_{\text{ave}} = \sum_{i=1}^{n} \mu_i X_i \tag{2.25}$$

$$M_{\text{atm}} = \int 4\pi r^2 \rho\left(r\right) dr \tag{2.26}$$

$$q_j = \frac{\sum_i^{n_{\text{mol}}} X_i n_{i,j}}{\sum_j^{n_{\text{elem}}} \sum_i^{n_{\text{mol}}} X_i n_{i,j}} \tag{2.27}$$

where q_j is the mole fraction of the elemental species j, X_i is the mixing ratio of molecule i, and $n_{i,j}$ is the number of atoms of elemental species j in molecule i.

2.8 Discussion

2.8.1 Atmospheric Retrieval as a Mean of Studying Exoplanets

The objective in the development of the new retrieval methodology is to remain independent of model assumptions as much as possible and let the observational data speak for themselves. By not employing any assumptions on the elemental composition, chemical equilibrium, or formation and evolution arguments in the retrieval process, our results remain independent of preconceived ideas for the planet under investigation. The atmospheric composition is, instead, completely described by free parameters and no hidden biases or asymmetries favoring a particular molecular species in the Bayesian prior are introduced.

The main assumptions in our approach are limited to the principles of radiative transfer in local thermodynamic equilibrium, hydrostatic equilibrium, and the correctness of the molecular line lists. For cases in which no secondary eclipse measurements are available, we added radiative-convective equilibrium to determine a reasonable temperature structure. However, since the exact temperature profile has a secondary effect on the transmission spectrum, we find that this temperature modeling has little effect on the retrieval results we obtain. In order to reasonably constrain the atmosphere given the limited data available in the near future, another guideline in the development was to keep the number of parameters to a minimum, while still ensuring that the parameters uniquely define the state of the model atmosphere. In this study, we assigned a single free parameter for the effective mixing ratio of each molecular species in the atmosphere, effectively comparing well-mixed atmospheres to the observation (see Section 3.5.2).

The main advantage of our retrieval approach for super-Earths over detailed modeling of atmospheric chemistry and dynamic models is that it provides an opportunity to discover unexpected types of planets and atmospheres that do not agree with our current understanding of formation, evolution and atmospheric processes. For

example, no self-consistent atmospheric chemistry model would predict that the atmosphere of a terrestrial planet like Earth has an O_2 mixing ratio as high as 21%. Only the direct interpretation of observations can tell us about the existence of such unusual atmospheric compositions. The identification of absorption lines of the O_2 absorption without constraining the high mixing ratio would not be a biosignature because low abundances of O_2 can be a result of photochemical composition.

2.8.2 Atmospheric Retrieval versus Detailed Atmospheric Modeling

The atmospheric retrieval method and detailed, self-consistent modeling of a planetary atmosphere (Burrows et al., 1997; Seager et al., 2005; Burrows et al., 2008) present two completely complementary approaches to the study of planetary atmospheres. For studies of solar system planets, it is common practice to use observational constraints from remote sensing to motivate or validate detailed modeling of chemistry or dynamics. For a classic example, the retrieved temperature-pressure profile from radio occultation measurements on Titan motivated and guided detailed modeling of the thermal structure to explain the measured temperature profile (McKay et al., 1989). Similarly, the observational detection and abundance constraints on the methane plume in the Martian atmosphere motivated a multitude of studies on potential sources and sinks (e.g., Lefevre & Forget, 2009; Krasnopolsky et al., 2004).

We envision the same kind of complementarity for the characterization of exoplanets. The strategy would be to use the retrieval method as presented in this work to identify quantitative constraints on the atmospheric composition provided by the observations. Then, the constraints on elemental or molecular abundances can serve as inputs to help guide the detailed atmospheric modeling to explore physical processes that would explain the findings. Conversely, atmospheric retrieval can be complemented by self-consistent forward models in that self-consistent modeling can further constrain the parameter space by checking the physical plausibility of the atmospheric scenarios.

Chemistry-Transport and Photochemistry Models While self-consistent forward models of atmospheric chemistry aim to provide the physical understanding of the relevant processes in the atmosphere, self-consistent forward models are dependent on inputs such as the background atmosphere or elemental abundances, the boundary conditions at the surfaces, as well as an accurate representation of all relevant chemical reactions, heat transport and cloud formation processes. If we knew all inputs and relevant processes a priori, one could compute the chemical composition and state of the atmosphere with a self-consistent model. However, many of these inputs will not be known for exoplanets, especially for planets that do not agree with our preconceived ideas.

Atmospheric retrieval provides an alternative to self-consistent modeling for obtaining the composition and state of the atmosphere, but is based on observations rather than detailed modeling. It can, therefore, guide the development and application of self-consistent models in providing constraints on the background atmosphere as well as constraints on the minor species in atmosphere. As the background atmospheres of super-Earth planets are not known a priori, it appears that most self-consistent models of atmospheric chemistry will require that one uses atmospheric retrieval to infer at least the main species in the atmospheres of these objects. If the self-consistently modeled atmospheric properties deviate from the ones provided by the retrieval analysis of given a set of observations, then the analysis of the deviation may motivate the inclusion of additional physical or chemical processes to the self-consistent model (e.g., additional sources and sinks for molecular species). The combination of self-consistent modeling and atmospheric retrieval to interpret observations can, therefore, enhance our understanding of the physical processes in the atmospheres of extrasolar planets.

Atmospheric Dynamics One of the most critical factors affecting atmospheric circulation models is determining the pressure level at which the bulk of the stellar energy is deposited (Heng, 2012; Perna et al., 2012). Atmospheric retrieval may provide a useful input to determine this pressure level for an observed exoplanet

because it allows the constraint of the molecular composition of the atmosphere, which strongly affects the opacity of the atmosphere to the incident stellar flux. For hot Jupiters, previous studies (e.g., Showman et al., 2009) assumed chemical equilibrium in combination with solar composition as a fiducial estimate of the composition. When modeling a specific planet, the danger is that these assumptions for the composition introduce inaccuracies in the deposition of stellar light and therefore alter the results.

For circulation modeling of super-Earth atmospheres, obtaining observational constraints on the atmospheric properties is critical. Without observations or a better understanding of super-Earth planets, even the main constituents of these atmospheres are unknown, and therefore no fiducial assumptions on the composition and stellar flux deposition can be made. For rocky planets, the presence of a solid surface and the pressure level at the surface play a major role in the atmospheric circulation. The retrieved surface pressure from observations may, therefore, also provide an essential input for circulation models.

Chapter 3

Unique Characterization of Atmosphere using Transmission Spectroscopy

3.1 Introduction

In this chapter, we first conceptually identify the features in the spectrum that are required to uniquely constrain the compositions of general exoplanet atmospheres (Section 3.2). Based on the conceptual understanding, we then present numerical results from the MCMC retrieval analysis for synthetic *JWST* NIRSpec observations of three scenarios for the super-Earth GJ 1214b (Section).

Our most significant finding is that a *unique* constraint on the mixing ratios of the absorbing gases and up to two spectrally inactive gases is possible with moderate-resolution transmission spectra. Assuming a well-mixed atmosphere and that N_2 and a primordial mix of H_2 + He are the only significant spectrally inactive components, we can fully constrain the molecular composition of the atmosphere. We also find, however, that even a robust detection of a molecular absorption feature ($>10\sigma$) can be insufficient to determine whether a particular absorber is the main constituent of the atmosphere ($X_i > 50\%$) or just a minor species with a mixing ratio of only a less

than 0.1%, if we do not observe the signature of gaseous Rayleigh scattering.

3.2 Conceptual Picture: Uniquely Constraining Exoplanet Atmospheres

Identifying absorbing molecules by their spectral features is conceptually straightforward, as molecules generally absorb at distinct wavelengths. Constraining the mixing ratios of the atmospheric gases is more complicated because the observable transmission spectrum depends not only on the mixing ratios of the absorbers, but also on the exact planetary radius (as measured by the radius at the reference pressure level, $R_{P,10}$), the surface or cloud-top pressure, and the mean molecular mass of the background atmosphere. The absorber mixing ratios may therefore remain unconstrained over several orders of magnitude despite strong detections of a molecular absorption features in the near-infrared wavelength range. The difficulty in constraining the mixing ratios of the atmospheric constituents was not discovered in previous work on atmospheric retrieval because hot Jupiters were assumed to be cloud-free and the mean molecular mass of their hydrogen-dominated atmospheres was known a priori (e.g., Madhusudhan & Seager, 2009). In the following, we explain which observables from different parts of the spectrum must be combined to successfully constrain the composition of a *general* exoplanet atmosphere.

The transmission spectrum of an atmosphere with n relevant absorbers provides $n + 4$ independent observables (Figure 3-1). Combined, these $n + 4$ observables can be used to constrain the n unknown mixing ratios of the absorbing gases, the mixing ratios of up to two spectrally inactive gases (e.g., N_2 and primordial $H_2 + He$), the planetary radius at reference pressure level, and the pressure at the surface or upper cloud deck. The remaining information in the transmission spectrum is highly redundant with the $n + 4$ independent observables.

The $n+4$ independent observables are as follows. For each of the n absorbers, the broadband transit depths in the strongest features provide one independent observ-

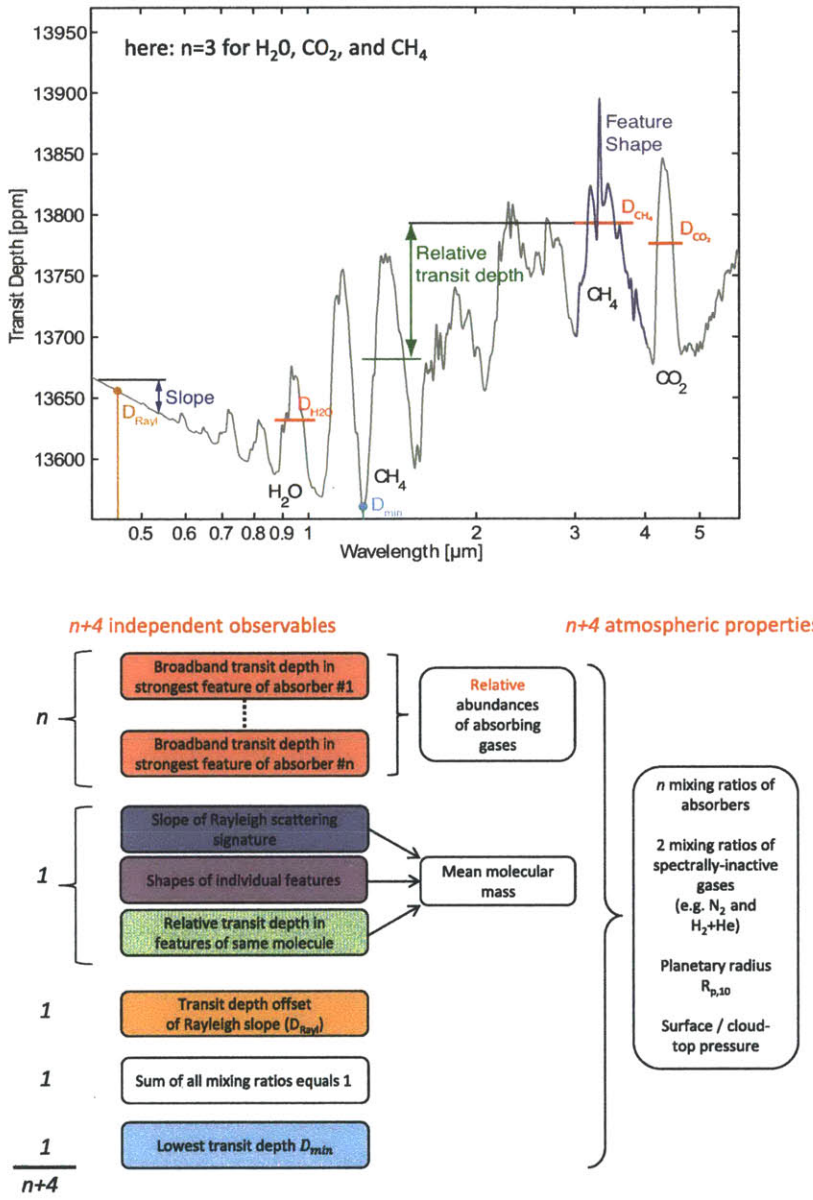

Figure 3-1: Unique constraints on the atmospheric properties based on observables in the transmission spectrum. The transmission spectrum of an atmosphere with n relevant absorbers contains $n+4$ independent pieces of information that constrain the n mixing ratios of these absorbers, up to two mixing ratios of the two spectrally inactive components H_2+He and N_2, the planetary radius at a reference pressure level, $R_{P,10}$, and the surface/cloud-top pressure. The left panel illustrates conceptually the individual observables in the transmission spectrum that carry the n+4 pieces of information for an example with $n = 3$ absorbers. For well-mixed atmospheres, the three observables "Slope of the Rayleigh signature,", "Shapes of individual features," and "Relative transit depths in features of same molecule" are redundant and provide only one independent piece of information. Note that to uniquely constrain *any* of the $n+4$ atmospheric properties on the far right, *all* $n+4$ pieces of information need to be available, unless additional assumptions are made.

able. By measuring and comparing the broadband transit depths in the absorption features of different molecules, we can directly determine the *relative* abundances of the absorbing gases in the atmosphere (Section 3.2.1). For example, given the broadband transit depths in the 3.3 μm CH_4 feature and in the 4.3 μm CO_2 feature, we can determine that there must be "x" times more CO_2 than CH_4 in the atmosphere. If the feature of one molecular absorber is not present, transit depth measurements at wavelengths for which the absorption cross sections of the molecular species are high can still provide an upper limit on the absorber abundance *relative* to the other absorbers.

Next, we have a total of *one* additional piece of information from either (1) the linear slope of the Rayleigh signature, (2) the shapes of individual features, or (3) the relative transit depths in features of the same molecule. The information from the three observables is highly redundant. From one of the three observables, we can directly constrain the scale height, and, given an approximate estimate of the atmospheric temperature, we can obtain an estimate of the mean molecular mass (Section 3.2.2). Importantly, for general atmospheres that may contain clouds, it is the slope at which the transit depth changes as a function of the extinction cross section thatenables us to measure the mean molecular mass. The overall transit depth variation as currently discussed in many papers on the super-Earth GJ 1214b (e.g., Miller-Ricci & Fortney, 2010; Bean et al., 2011; Croll et al., 2011) measures the mean molecular mass only for cloud-free atmospheres.

Three additional independent constraints are provided by the transit depth offset of the Rayleigh slope, the fact that all mixing ratios must sum to 1, and the measure of the lowest transit depths in the spectrum. Comparing the transit depth offset of the Rayleigh slope and the transit depths at near-infrared wavelengths provides us with a measure of the amount of spectrally inactive gas in the atmosphere. Given all previously discussed observables, the lowest transit depths in the spectrum allow us to independently constrain the surface/cloud-top pressure (Section 3.2.4). If the surface/cloud-top is at a deep layer in the atmosphere and the molecular opacities across the observed wavelength range are high, a direct detection of a surface is not

possible. In this case, the minimum transit depth will provide a lower limit on the surface/cloud-top pressure.

Note that we need *all* $n+4$ observables together in order to determine *any* of the atmospheric parameters uniquely. If a single piece of the puzzle is missing, e.g., the transit depths at short wavelengths are not observed, then the composition, including the volume mixing ratios of the absorbers, will stay weakly constrained, even if we have detected the feature with high significance.

3.2.1 Relative Abundances of Absorbing Gases

The infrared part of the transmission spectrum provides a good tool to constrain the relative abundances of the molecular absorbers. Constraining the absolute value of the volume mixing ratios, however, might not be possible to within orders of magnitude, even with low-noise observations capturing the shapes of the absorption features because the infrared part of the spectrum lacks an absolute reference for the transit depth.

The measured transit depths in the absorption features are mainly related to the number density of the absorbing molecule, $n_i(r)$, as a function of the radius from center of the planet, r. The function $n_i(r)$, however, provides little useful insight unless we are able to determine a surface radius or the number density of a second gas for comparison. In other words, if we do not detect a surface, then only the mixing ratios of the atmospheric gases have a meaningful interpretation, not the absolute number densities, because we are missing an absolute pressure scale. Obtaining the mixing ratios of an absorbing gas directly by observing the absorption features of this gas is complicated, however, because different combinations of the absorber mixing ratio, X_i, and the planetary radius, $R_{P,10}$, can lead to the same number density, $n_i(r)$, and, therefore, to virtually the same absorption feature shape. To constrain the mixing ratio of a particular gas independently, a reference for the planetary radius needs to be obtained from a different part of the spectrum.

For a quantitative example, we show the 4.3 μm absorption feature of CO_2 for two different atmospheric compositions in Figure 3-2. The compositions are 90% N_2 and

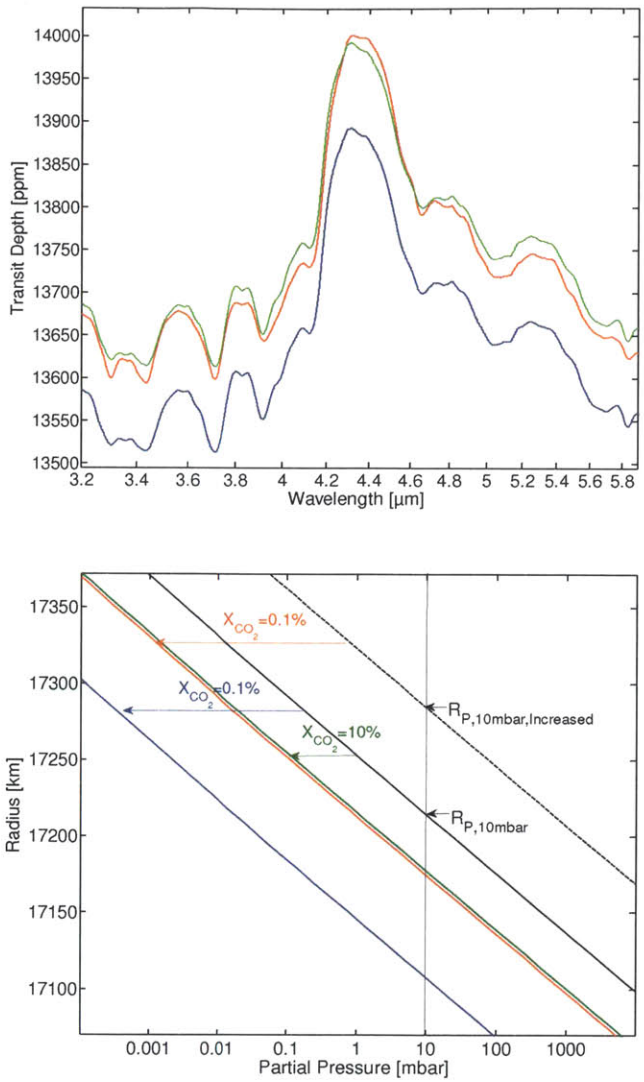

Figure 3-2: Degeneracy between the absorber mixing ratio, X_{CO_2}, and the planetary radius at the reference pressure level, $R_{P,10}$. The upper panel illustrates the modeled transmission spectra in the 4.3μm CO_2 absorption feature for two different atmospheric compositions. The atmospheric composition of scenario 1 (red) is 10% CO_2 and 90% N_2. For the same planetary radius, the transit depth in the absorption feature of scenario 2 (blue; 0.1% CO_2 and 99.9% N_2) is lower by $\sim$ 100 ppm across the entire feature. Increasing the planetary radius for scenario 2, however, leads to a transmission spectrum (green) that closely resembles scenario 1. As a result of this degeneracy between X_{CO_2} and $R_{P,10}$, the mixing ratio of CO_2 cannot be determined to within several orders of magnitude even for low-noise observations of the feature. The lower panel shows the total pressures for planets with two different planetary radii (black) and the partial pressure of CO_2 as a function of the distance from the planetary center (colors match left panel). Two atmospheres with different absorber mixing ratios (red and green) can have the same partial pressure/number density as function of distance from the planetary center leading to similar absorption features.

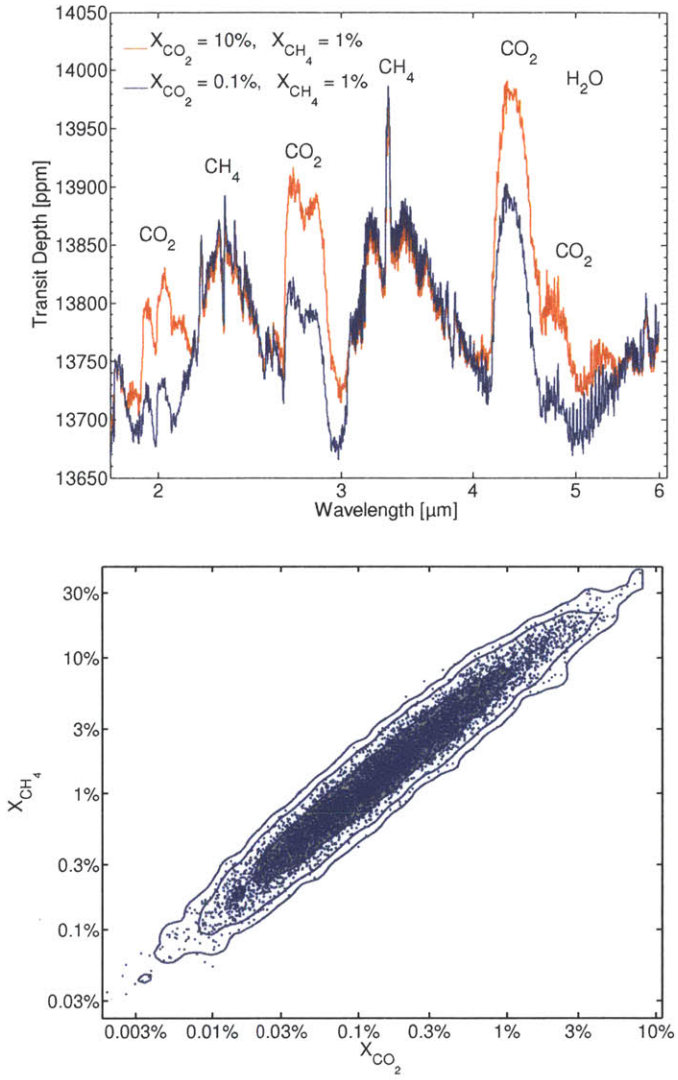

Figure 3-3: Constraining the relative abundances of absorbing gases from the near-infrared spectrum. The left panel shows the transmission spectrum for the atmospheric scenarios 1 (red, 10% CO_2) and 2 (blue, 0.1% CO_2) as described in Figure 3-2, but with 1% N_2 replaced by the absorbing gas CH_4. While the CO_2 features have a vertical offset between scenario 1 and scenario 2, the CH_4 features are unaffected by the CO_2 mixing ratio. The transit depth in CH_4 features can, therefore, serve as a relative reference for the CO_2 mixing ratio. The right panel shows the two-dimensional marginal posterior probability distribution of the mixing ratios, X_{CO_2} and X_{CH_4} as retrieved from low-noise synthetic observations of the near-infrared spectrum (R=100, $\sigma_{(Rp/R*)^2} \approx 20$ ppm, $\lambda = 2$-$5\,\mu$m) of scenario 1. The solid lines indicate the 1σ, 2σ, and 3σ credible regions. Measuring the transit depth in infrared features of CO_2 and CH_4 provides good constraints on the relative abundance ratios of the two gases. The volume mixing ratios of the gases, however, are strongly correlated. The individual mixing ratios remain unconstrained across three orders of magnitude despite robust detections of the infrared features and sufficient spectral resolution to observe the feature shapes.

10% CO_2 for scenario 1 and 99.9% N_2 and 0.1% CO_2 for scenario 2. If the planetary radius, $R_{P,10}$, for the two scenarios is the same, more starlight is blocked in scenario 1 due to the higher number density $n_{CO_2}(r)$. The transit depth inside the spectral features of CO_2 is therefore higher than for scenario 2. If the planetary radius $R_{P,10}$ in scenario 2 is increased by only 70 km ($\approx 0.4\%$), however, then the number density $n_{CO_2}(r)$ in scenarios 2 equals the one in scenario 1, and the absorption feature of scenario 1 closely resembles the absorption feature of the new scenario 2. The remaining small difference in the transmission spectra is due to the effect of pressure and temperature on the absorption line broadening. The effect of changes in line broadening is of secondary order though, which makes the distinction between scenarios 1 and 2 difficult, even with extremely low-noise observations. Determining the mixing ratio of CO_2 by observing *only* CO_2 features is, therefore, highly impractical.

A relative reference to break the degeneracy between the planetary radius and the mixing ratio is provided by the transit depths in absorption features of different absorbers. Conceptually, this is possible because a change in the planetary radius affects the absorption features of both gases equally, while a change in the mixing ratio of one of the absorbers only affects the features of that absorber. The transit depth difference between two features of different absorbers is independent of the planetary radius and only dependent on the relative abundance ratios of the absorbers and their absorption cross sections in the features. As the absorption cross section are known from the molecular databases, comparing the transit depths in features of different absorbers allows one to constrain the relative abundance of these absorbers. For a numerical example, we return to our N_2-CO_2 atmosphere and replace 1% N_2 by CH_4. In the spectral region around the 3.5 μm CH_4 feature (Figure 3-3), the spectrum remains unaffected by the change in the CO_2 mixing ratio and can serve as a reference to probe the relative abundances of CO_2 and CH_4.

The infrared part of the transmission spectrum covering multiple absorption features of different molecular species, therefore, provides good constraints on the relative abundances of the molecular absorbers, but hardly contains any information on the volume mixing ratios of the absorbers. Even low-noise NIR observations capturing

the shapes of the absorption features might not constrain the absolute value of the mixing ratio to within orders of magnitude because the infrared part of the spectrum provides little information on the abundances of spectrally inactive gases.

In our example, the abundance ratio $\frac{X_{CH_4}}{X_{CO_2}}$ is constrained to within a factor of a few at 3σ, while the volume mixing ratio of CH_4 compatible with the simulated observation can vary over three orders of magnitude between 0.03% and 30%. Note that the reason for the correlation between X_{CO_2} and X_{CH_4} is *not* the overlap of absorption features of the molecular species. Overlapping features would cause an *anti*-correlation between the abundances of the two absorbers.

3.2.2 Mean Molecular Mass

It has been shown that, for clear atmospheres, measuring the change in transit depth, $\Delta\delta$, across spectral features gives an order of magnitude estimate of the scale height and, therefore, the mean molecular mass (Miller-Ricci et al., 2009). For a general atmosphere, however, the depth of the absorption features cannot be used to constrain the mean molecular mass because clouds, hazes, and a potentially present surface also affect the depths of spectral features. Here we show for general atmospheres that the value of the mean molecular mass can be determined by measuring the slope, $\frac{dR_{P,\lambda}}{d(ln\sigma_\lambda)}$, with which the "observed" planet radius, $R_{P,\lambda}$, changes as a function of the extinction cross section, σ_λ, across different wavelengths. In practice, good observables to independently constrain the mean molecular mass are (1) the slope Rayleigh scattering signature at short wavelengths, (2) the relative sizes of strong and weak absorption features of the same molecule, and (3) the shape of the wings of a strong molecular absorption feature.

For the optically thick part of the spectrum, the observed radius of the planet changes linearly with the logarithm of the extinction cross section (Etangs et al., 2008) and the slope $\frac{dR_{P,\lambda}}{d(ln\sigma_\lambda)}$ is directly related to the atmospheric scale height,

$$H = \frac{dR_{P,\lambda}}{d(\ln \sigma_\lambda)}. \tag{3.1}$$

A measurement of the observed planet radius, $R_{P,\lambda}$, at two or more wavelengths with different absorption or scattering cross sections, σ_λ, therefore, permits the determination of the scale height. Given an estimate of the atmospheric temperature, e.g. $T \approx T_{eq}$, we can observationally determine an estimate of the mean molecular mass

$$\mu_{\rm mix} = \frac{k_B T}{g} \left(\frac{dR_{p,\lambda}}{d(\ln \sigma_\lambda)} \right)^{-1} \times \left(1 \pm \frac{\delta T}{T} \right), \tag{3.2}$$

where the factor $\left(1 \pm \frac{\delta T}{T}\right)$ accounts for the inherent uncertainty due to the uncertainty, δT, in modeling the atmospheric temperature, T, at the planetary radius $r = R_{P,\lambda}$ (Appendix). Even if the uncertainty in the temperature estimate is several tens of percents of the face value, we will find useful constraints on the mean molecular mass because the mean molecular mass varies by a factor on the order of $8 - 20$ between hydrogen-dominated atmospheres and atmospheres mainly composed of H_2O, N_2, or CO_2.

The most straightforward way to determine the mean molecular mass is to measure the slope of the Rayleigh scattering signature at short wavelengths. The Rayleigh scattering coefficient varies strongly with wavelength as $\sigma(\lambda) \propto \lambda^{-4}$. From $\sigma(\lambda) \propto \lambda^{-4}$, we obtain

$$\mu_{mix} = \frac{4 k_B T}{g R_*} \frac{\ln\left(\frac{\lambda_1}{\lambda_2}\right)}{\left(\frac{R_p}{R_*}\right)_{\lambda_2} - \left(\frac{R_p}{R_*}\right)_{\lambda_1}} \times \left(1 \pm \frac{\delta T}{T} \right), \tag{3.3}$$

Measuring the transit depth $D_\lambda = \left(\frac{R_p}{R_*}\right)^2_\lambda$ at two different wavelengths λ_1 and λ_2 that are dominated by Rayleigh scattering, therefore, provides the mean molecular mass. For a quantitative example, we show the transmission spectra of a CO_2-dominated atmosphere (95% CO_2+ 5% N_2) and a N_2-dominated atmosphere with small amount of CO_2 as the only absorber (0.15% CO_2, 99.85% N_2) in Figure 3-4. Despite the difference in mean molecular mass, the feature depths are similar due to the different total amounts of the absorber CO_2; thus, the feature depth cannot be used to determine the scale height. The Rayleigh slope at short wavelength

($\lambda < 0.8\mu$m), however, is only affected by the scale height and can serve as a good measure of the mean molecular mass.

A second way of constraining the mean molecular mass is based on analyzing the detailed shape of the wing and core of spectral features. The absorption cross section varies strongly from the center to the outer wings. Measuring the detailed shape of a spectral feature at sufficient spectral resolution, therefore, probes a large range of cross sections and allows the constraint of the mean molecular mass. In our example, the detailed shape of the 4.3 μm CO_2 feature shows the difference between the scenarios (Figure 3-4). For smaller mean molecular mass, the feature is higher at the center with narrow wings, while the large mean molecular mass leads to broader features. The measurement of this difference requires at least a moderate spectral resolution ($R \sim 50$) and a high signal-to-noise ratio (S/N).

A third way to probe the mean molecular mass is to quantitatively compare the broadband transit depths in different spectral features of the same absorber. Again, we probe the planetary radius at wavelengths for which the cross sections are different: strong absorption features have large absorption cross sections, while weaker features of the same absorber have smaller cross sections. A quantitative comparison of the depths of individual features therefore provides the gradient $\frac{dR_{P,\lambda}}{d(ln\sigma_\lambda)}$ and constrains the scale height and mean molecular mass. For atmospheres with small mean molecular masses, the gradient $\frac{dR_{P,\lambda}}{d(ln\sigma_\lambda)}$ is large, resulting in greater differences in the transit depths between the strong and the weak features (Figure 3-4).

3.2.3 Volume Mixing Ratios of the Atmospheric Constituents

The primary quantities affected by the abundance of spectrally inactive gases are the estimate of the mean molecular mass, $\mu_{\rm mix}$, discussed in Section 3.2.2 and the transit depth offset of the molecular Rayleigh scattering slope, $D_{\rm Rayl}$. Combining the information on $\mu_{\rm mix}$ and $D_{\rm Rayl}$ with the constraints on the relative abundances of the absorbers from the NIR spectrum (Section 3.2.1) provides unique constraints on the

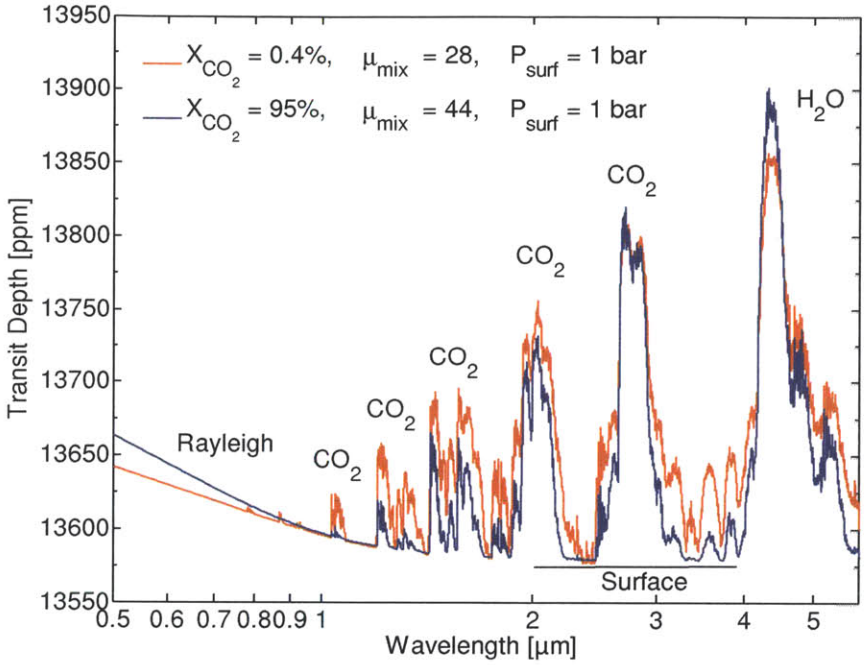

Figure 3-4: Visible to near-infrared transmission spectra for two atmospheric scenarios with similar absorption feature sizes. The first scenario (blue) is a N_2-rich atmosphere (0.15% CO_2, 99.85% N_2). The second scenario (red) is CO_2 dominated (95% CO_2 and 5% N_2). Despite the different mean molecular mass (28 vs. 44) the infrared absorption feature sizes are similar because the difference in the vertical extent of the atmosphere due to the different scale heights is compensated for by the difference in the total amount of the absorbing CO_2 gas. A reliable way to determine the scale height is to measure either the Rayleigh scattering slope $\frac{dR_{P,\lambda}}{d(\ln \lambda)}$ at short wavelengths, the slope $\frac{dR_{P,\lambda}}{d(ln\sigma_\lambda)}$ in strong absorption features, or the relative feature depths between strong and weak features of the same molecule. The lower mean molecular mass atmosphere (blue) shows a steeper Rayleigh scattering slope, larger differences in the CO_2 absorption features depth, and narrower features than the higher mean molecular mass atmosphere (red).

volume mixing ratios of both the spectrally inactive gases and molecular absorbers.

The atmospheres of Jupiter-sized planets present a simplified case for atmospheric retrieval. From their radius and mass measurements, we can conclude that they have accreted a hydrogen-dominated atmosphere, thus we know the mean molecular mass a priori. Constraining the volume mixing ratios of the molecular species in the atmosphere, nonetheless, requires the observation of the transit depth offset of the molecular Rayleigh scattering slope, $D_{\rm Rayl}$ at short wavelength.

Neglecting for now the effect of refractive index variations between different gas mixtures, the transit depth offset of the molecular Rayleigh scattering slope, $D_{\rm Rayl}$, is only a function of planetary radius at the reference pressure, $R_{P,10}$. The transit depth offset of the Rayleigh scattering signature can, therefore, serve as a reference transit depth to obtain an absolute scale for the atmospheric pressure and to determinethe volume mixing ratios of the absorbers from the absorption features in the NIR. In general, atmospheres rich in absorbing gases will show transmission spectra for which the transit depth in the Rayleigh scattering signature is small with respect to the transit depth in the NIR, while atmospheres dominated by spectrally inactive gases will show transmission spectra that have a strong Rayleigh scattering signatures and absorption features in the NIR at a lower transit depth levels.

Obtaining the absolute abundances for all relevant absorbing gases enables us to constrain the total mixing ratio of the spectrally inactive gases to be $X_{\rm inactive} = 1 - \sum_{i=1}^{n} X_i$, where n is the number of absorbers in the atmosphere. Conceptually, the estimate of the mean molecular mass, $\mu_{\rm mix}$, can then be used to determine the individual mixing ratios of the spectrally inactive components, N_2 and H_2 + He. We obtain the volume mixing ratios of N_2 and primordial gas from

$$\mu_{mix} = \mu_{N_2} X_{N_2} + \mu_{H_2+He} \left(X_{inactive} - X_{N_2} \right) + \sum_{i=1}^{n} \mu_i X_i \tag{3.4}$$

and

$$X_{\rm H_2+He} = X_{\rm inactive} - X_{\rm N_2}. \tag{3.5}$$

Individual constraints on H_2 and He are not possible because only two spectrally inactive gases can be fit. Three or more individual spectrally inactive components inherently lead to degeneracy because the same mean molecular mass of the spectrally inactive gases can be obtained by different combinations of the mixing ratios of the gases.

In reality, the effective refractive index of the gas mixture varies depending on the composition and affects the transit depth offset of the Rayleigh scattering signature (Section 2.3.1). When simultaneously retrieving the mixing ratios of all gases, however, we also determine the refractive index in the process because the refractive index is a direct function of only the mixing ratios and not an additional unknown.

3.2.4 Surface Pressure

We can discriminate between a thick, cloud-free atmosphere and an atmosphere with a surface, where the surface is either the ground or an opaque cloud deck. For atmospheres with an upper surface at pressures lower than $P_{\rm surf} \lesssim 100\,{\rm mbar} \ldots 5\,{\rm bar}$ (depending on composition), we can quantitatively constrain the pressure at this surface. For a thick atmosphere, we can identify a lower limit on the surface pressure.

A surface strongly affects the part of the spectrum without absorption features while having only a weak or negligible effect on the part of the transmission spectrum with strong molecular absorption or scattering. In the spectral regions with weak absorption, a thin atmosphere has a relatively constant continuum because the surface cuts off the grazing light beams at a radius that is independent of the wavelength (Des Marais et al., 2002; Ehrenreich et al., 2006). A thick atmosphere without a surface lacks a flat continuum.

Conceptually, the optically-thick regions of the spectrum, those for which the transit depth is independent of the surface pressure, constrain the mixing ratios of the molecular species in the atmosphere as described in Section 3.2. The surface pressure can then be determined from the transit depths in the parts of the spectrum in which absorption and scattering are weak (Figure 3-1). For a noise-free spectrum, the strongest constraint on the surface pressure is provided by the minimum transit

depth, $\delta_{\rm min}$, measured across the spectrum. The minimum transit depth determines the deepest pressure level for which light is transmitted through the atmosphere and, therefore, provides a lower limit on the surface pressure. In practice, the retrieval of the mixing ratios, surface pressure, and other parameters is performed simultaneously based on the information in the entire spectrum.

Taking the example of a N_2-CO_2 atmosphere (Figure 3-5), the shape of the spectral features in the 2-6 μm range is mostly unaffected by changes in surface pressure, as long as the surface pressure is higher than 100 mbar. For exquisite data, the composition of the atmosphere can, therefore, be retrieved from the 2 to 6 μm range independently of the surface pressure. Conversely, the spectral region between 0.5 and 2 μm is strongly affected by surface pressure, but the effects of surface pressure and mixing ratios are usually degenerate. Taking the retrieved mixing ratios from the part of the spectrum unaffected by surface pressure, allows a unique determination of the surface pressure.

3.3 Synthetic Observations of Super-Earth Transmission Spectra

The goal of the quantitative analysis presented in this work is to explore which constraints on the atmospheric properties of super-Earth exoplanets can be extracted from low-noise transmission spectra in the coming decades. In this section, we describe synthetic, low-noise observations of the transmission spectra of three different, hypothetical types of hot super-Earths transiting nearby M-stars as they may be obtained with the *James Webb Space Telescope* (*JWST*). To make the results most relevant in the context of current observational efforts, we adopt the stellar, orbital, and planetary parameters of the super-Earth GJ 1214b (Charbonneau et al., 2009).

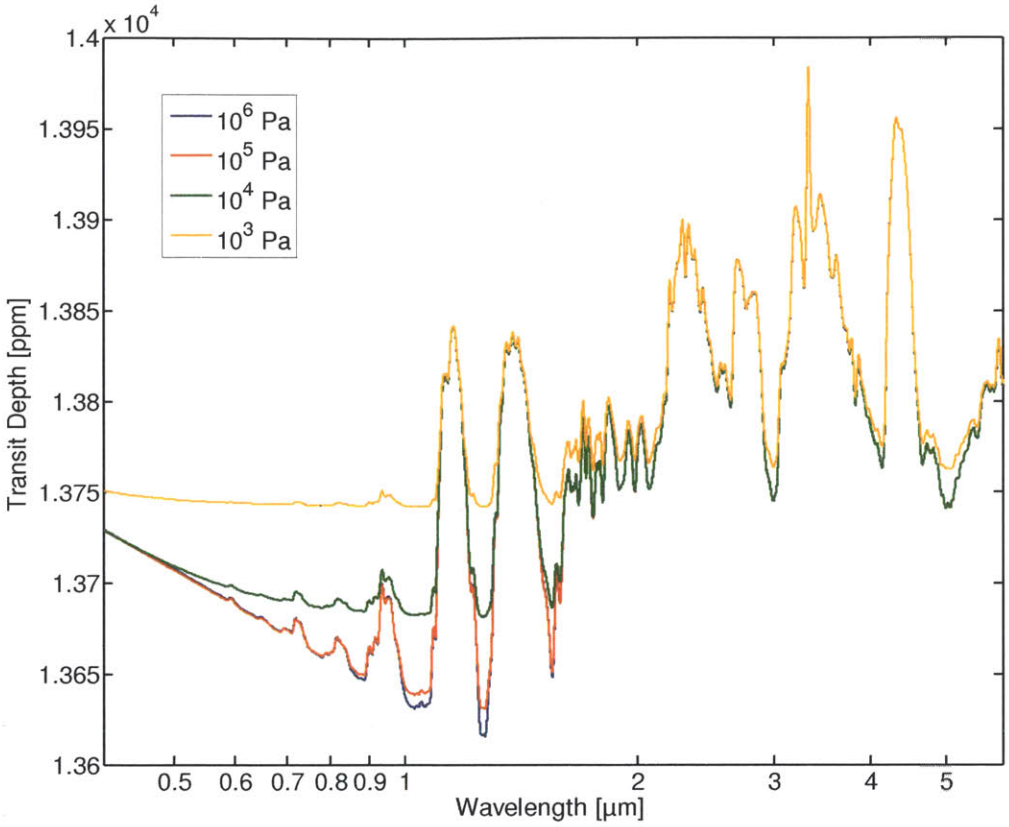

Figure 3-5: Effect of the surface pressure on the transmission spectra of exoplanets. The transmission spectra of model atmospheres with 99% N_2 and 1%CO_2 are depicted for four different surface pressures. The radius, $R_{P,10}$, at which the atmospheric pressure is 10 mbar is set to the same value for all four. With $R_{P,10}$ set to the same value, the transit depths in the strong CO_2 absorption bands (e.g., around 2.7, 3.3, and 4.3μm) are independent of the surface pressure since the grazing star light at these wavelengths does not penetrate to lower layers of the atmosphere. Conversely, the parts of the spectrum ($< 1.6\,\mu$m) with little molecular absorption and scattering show a strong dependence on the surface pressure. Combining information from parts of the spectrum that are sensitive to surface pressure and parts of the spectrum that are insensitive to surface pressure enables one to find independent constraints on atmospheric composition and surface pressure. At sufficiently high surface pressures, even the spectral regions with low absorption cross sections become optically thick for a grazing light beam and the complete spectrum becomes insensitive to further increases in the surface pressure. For these thick atmospheres, only a lower limit on the surface pressure can be found.

3.3.1 Atmospheric Scenarios

3.3.1.1 Hot Halley world

The first scenario we consider is a volatile-rich super-Earth (Kuchner, 2003; Léger et al., 2004). The motivation for this scenario is to investigate the retrieval results for an atmosphere that is predominately composed of absorbing gases. For our specific case, we consider a scenario in which the planet has accreted ices with the elemental abundances of the ices identical to those in the Halley comet in the Solar System (Jessberger & Kissel, 1991). Some of the ices may have evaporated at the high equilibrium temperature and formed an atmosphere around the planet. We assume a well-mixed atmosphere around the planet whose chemical composition is calculated from chemical equilibrium at the 1 bar level. The resulting atmosphere is composed of H_2O (69.5%), CO_2 (13.9%), H_2 (11.8%), CH_4 (2.6%), and N_2 (2.2%). All mixing ratios are givenas volume mixing ratios. The atmosphere is assumed to be clear and sufficiently thick such that no surface affects the transmission spectrum in this scenario. (Table 3.1).

3.3.1.2 Hot nitrogen-rich world

For the second scenario we consider a nitrogen-dominated atmosphere representative of a rocky planet with an outgassed atmosphere similar to the atmospheres of Earth and Titan. The motivation for this scenario is to investigate the retrieval results for an atmosphere that is predominately composed of a spectrally-inactive gas that has no directly observable features in the spectrum. We chose an atmosphere dominated by N_2 (95.4%) and rich in CH_4 (3.5%), CO_2 (1%) and H_2O (0.1%) with a rocky surface at 1 bar.

3.3.1.3 Hot mini-neptune

The third scenario is a super-Earth with a thick hydrogen/helium envelope that has experienced a formation history similar to those of the giant planets. While we assume a primordial atmosphere, we deliberately chose an example that is away from

Planet Scenario	X_{H_2O}	X_{CO_2}	X_{CH_4}	X_{H_2}	X_{He}	X_{N_2}	Surface
Hot Halley world	69.5%	13.9%	2.6%	11.8%	≈ 0	2.2%	None
Hot nitrogen-rich world	0.1%	1%	3.5%	≈ 0	≈ 0	95.4%	Rocky surface atl bar
Hot mini-neptune	2%	10^{-6}	10^{-7}	84.9%	13.1%	≈ 0	Cloud deck at 100 mbar

Table 3.1: Mixing Ratios Of Molecular Constituents and Surface Pressure for the Three Super-Earth Scenarios Used to Generate Synthetic Transmission Spectra.

solar abundance and chemical equilibrium. The motivation for this scenario is to demonstrate the retrieval for a scenario that does not correspond to our preconceived ideas. The atmosphere we consider is composed of 84.9% H_2, 13.1% He, and 2% H_20, and has small mixing ratios of CO_2 (10^{-6}) and CH_4 (10^{-7}). We consider the presence of an opaque cloud deck of unknown nature at the 100 mbar level.

3.3.2 Observation Scenarios

For each of the three atmospheric scenarios, we simulate high-resolution transmission spectra ($R > 10^5$) and model the output of the *JWST* NIRSpec instrument covering the spectral range between 0.6 and 5 μm. We assume that the transit depths in the individual channels of *JWST* NIRSpec can be determined to within 20% of the shot noise limit. To compute the photon flux for each spectral channel individually, we scale the spectrum of a typical M4.5V star (Segura et al., 2005) to the apparent brightness of GJ 1214. For *JWST*, we adopt an effective diameter of the primary mirror of 6.5 m and a throughput before the instrument of 0.88 (Deming et al., 2009). We consider the spectral resolution for observations using the R=100 CaF_2 prism on NIRSpec ($R = 30 \ldots 280$). Our noise model adopts a total optical transmission for the NIRSpec optics after the slit of 0.4 and a quantum efficiency for the HgCdTe detector of 0.8 (Deming et al., 2009). We do not include any slit losses because the large aperture of *JWST* will encompass virtually all of the energy in the point source function. We find that read noise (6 e^-per Fowler 8) and dark current (0.03 e^- s^{-1}) are insignificant compared to photon noise. We account for a $\sim$ 20% loss of integration time due to the resetting and reading-out of the detector, based on the expected

saturation time of 0.43 sec for the brightest pixels on the NIRSpec detector for GJ 1214 (de Wit, personal communication). For a first order estimate of the observational errors, we neglect the wavelength dependence of the grating blaze function.

Given the instrument properties, we calculate the expected variances of the in-transit and out-of-transit fluxes due to shot noise and calculate the expected error in the observed transit depth. We assume that the total observation time used to measure the baseline flux before and after the transit equals the transit duration. We stack 10 synthetic transit observations for the high mean molecular mass atmospheres of the "hot Halley world" and "hot nitrogen-rich world" scenarios and use only a single transit observation for the more easily detectable hydrogen-dominated "hot mini-neptune" scenario.

3.4 Numerical Retrieval Results

3.4.1 Constraints on Composition

In this section, we present numerical results for synthetic *JWST* NIRSpec observations of the transmission spectrum of the super-Earth GJ 1214b. In all three atmospheric scenarios studied, we find that the analysis of moderate spectral resolution ($R \approx 100$) transmission spectra covering the spectral range between 0.6 and 5 μm can provide narrow probability posterior distributions for all absorbing gases with mixing ratios of several ppm or higher. (Figures 3-6-3-8). The well-constrained probability distributions allow a direct inference of the most likely estimate and credible regions (Bayesian equivalent to confidence intervals) for the mixing ratios of the individual molecular species. Spectrally inactive gases can also be constrained if their abundances are sufficient to affect the mean molecular mass and the Rayleigh scattering signature at short wavelengths.

For a given transmission spectrum, the relative uncertainties in the mixing ratios $\frac{\Delta X_i}{X_i}$ of absorbing gases (e.g., H_2O, CO_2, CH_4) are only weakly dependent on the absolute values of the mixing ratios. In other words, minor gases with mixing ratios as low

as tens of ppm can be constrained as well as the major atmospheric constituents (e.g., Figure 3-7(a)). The reason for this is that the long geometric path length of the grazing stellar light through the atmosphere of the extrasolar planet leads to significant spectral features in the transmission spectrum even for low-abundance gases (Brown, 2001). Increasing the mixing ratio increases the transit depth across the feature, but the uncertainty in the observed transit depth and, therefore, the uncertainty on the logarithm of the mixing ratio remains mostly unchanged. A detection limit does exist at low abundances, however because overlapping features of other absorbers may mask the features of extremely low-abundance gases. If all spectral regions in which the absorber is active are occupied by stronger features of other absorbers, then only an upper limit on the mixing ratio of the gas can be found (Figure 3-8).

In constrast to the absorbing gases, the uncertainties in the mixing ratios of spectrally inactive gases (e.g., N_2, H_2) are strongly dependent on their mixing ratios. Spectrally inactive gases affect the transmission spectrum only through changing the mean molecular mass and changing the transit depth difference between the Rayleigh scattering signature and the NIR spectrum (Section 3.2.3). If the mixing ratio of a spectrally inactive gas is a few tens of percent or more, the effect of the spectrally inactive gas on the atmospheric mean molecular mass is strong and, therefore, it is relatively easy to identify the spectrally inactive gas and constrain its mixing ratio (Figures 3-7 and 3-8). For lower mixing ratios, however, only weak constraints or an upper limit can be placed on the mixing ratios of spectrally inactive gases because their effect on the spectrum becomes negligible (e.g., Figure 3-6). This is particularly true for N_2 whose molecular mass (28 u) differs only by a factor of ~ 1.6 or less from the molecular masses of the most common spectrally active gases, e.g., H_2O (18 u), CH_4 (18 u), and CO_2 (44 u). Constraining the mixing ratio of H_2 is achieved down to lower mixing ratios because its molecular mass is lower than that of most absorbing gases by a factor of six or more.

3.4.2 Constraints on Surface Pressure

In the retrieval output, a thin atmosphere with a surface and a thick, cloud-free atmosphere show distinct posterior probability distributions for the surface pressure parameters. For atmospheres that are thin or have an upper cloud deck at low pressure levels, the probability distribution resembles a well-constrained, single-modal distribution (Figure 3-8(d)). For thick atmospheres that lack an observable surface, only an upper limit to the surface pressure can be retrieved (Figure 3-6(d))The posterior probability of the surface pressure plateaus toward high pressures, indicating that further increases in surface pressure lead to equally likely scenarios. We emphasize that, for a terrestrial planet, the two scenarios of a thin atmosphere with a solid surface or a thick atmosphere with an opaque cloud deck are not distinguishable from the transmission spectrum.

3.4.3 Effect of Unobserved Temperature

An inherent correlation arises between the planetary albedo and the mean molecular mass (Figure 3-9) if no direct measurements of the planetary temperature or the planetary albedo are available. While the correlation does not lead to uncertainties of individual parameters that range over orders of magnitude, it can be the dominant source of uncertainty on the composition if small error bars are achieved for the observations of the primary transit, but no direct measurements of the brightness temperature or the planetary albedo are available from secondary eclipse observations

.

The reason for the correlations between mean molecular mass and albedo is that the primary observables for the mean molecular mass (see Section 3.2.2) constrain the scale height rather than the mean molecular mass directly. Given the observational constraints for the scale height, different combinations of the atmospheric temperature and mean molecule mass may agree equally well with the scale height constraints imposed by the spectrum. The atmospheric temperature, in turn, is primarily determined by the planetary albedo, giving rise to the correlation between planetary

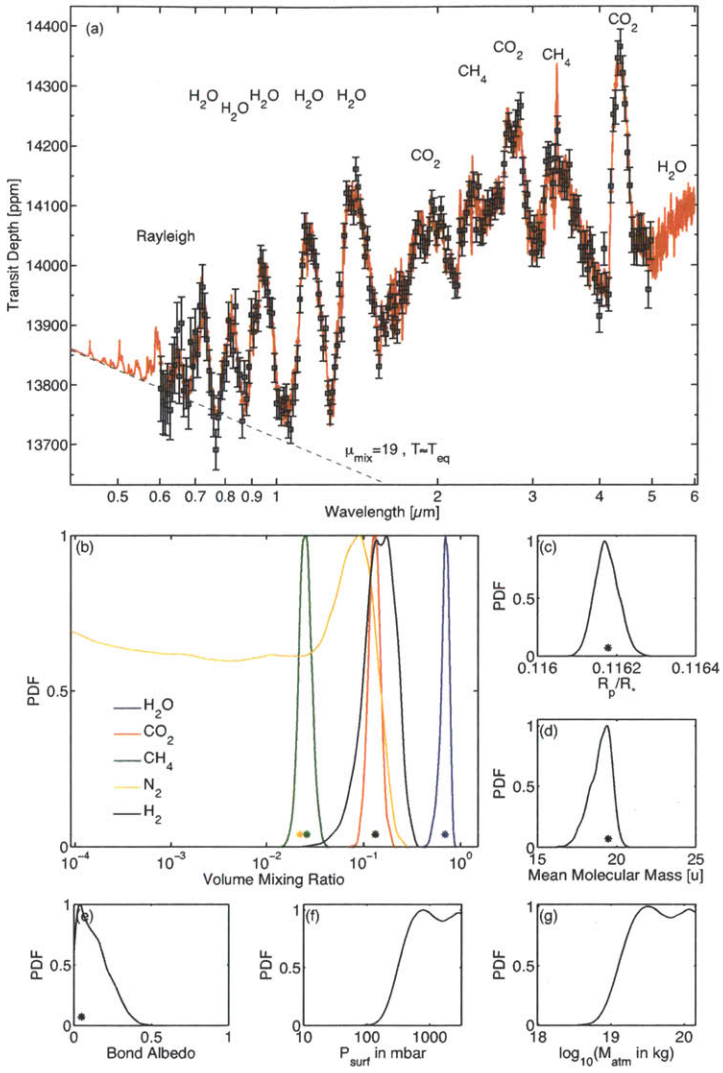

Figure 3-6: Synthetic transit observations and atmospheric retrieval results for the "Hot Halley world" scenario for the super-Earth GJ 1214b. The synthetic observations shown in panel (a) were simulated considering 10 transit observations with *JWST* NIRSpec and assuming that observational uncertainties within 20% of the shot noise limit are achieved (see Section 3.3.2). The dashed line shows the analytical Rayleigh scattering slope for comparison. Panels (b)-(g) illustrate the marginalized posterior probability distribution for the atmospheric parameters retrieved from the synthetic observations. For illustrative purposes, the distributions are normalized to a maximum value of 1. The asterisks indicate the values of the atmospheric parameters used to simulate the input spectrum. The narrow, single-peaked, posterior probabilities for the mixing ratios of H_2O, CO_2, CH_4, and H_2 in panel (b) indicate that unique constraints on the abundance of these gases can be retrieved in agreement with the atmospheric parameters used to simulate the input spectrum. H_2O can be identified as the main constituent. Only an upper limit on the mixing ratio of N_2 can be found because small amounts of the spectrally inactive N_2 have a negligible effect on the observed transmission spectrum. Constraints are also obtained for the surface/cloud-top pressure and total atmospheric mass above the surface/cloud-top (Panels (f) and (g)). In this scenario, the atmosphere is cloud-free down to high pressure levels, thus only a lower bound on the surface pressure can be found. No upper bound can be inferred as indicated by the posterior probability distributions approaching the flat prior distribution at high surface pressures.

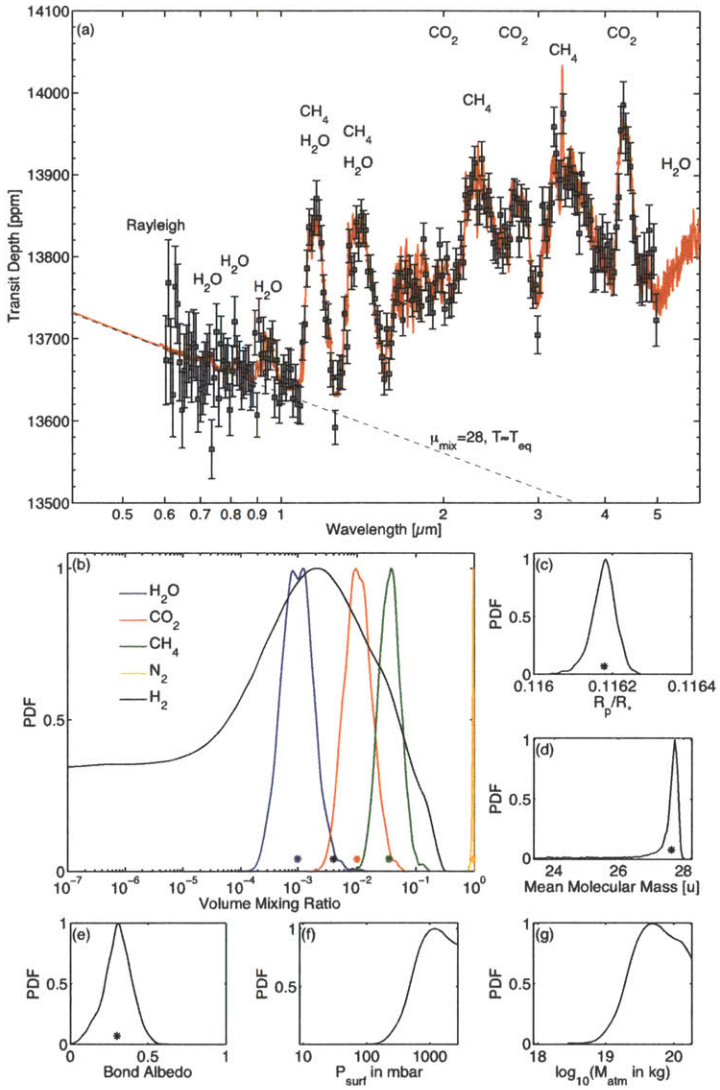

Figure 3-7: Synthetic transit observations and atmospheric retrieval results for the "Hot nitrogen-rich world" scenario of a super-Earth with the physical properties of GJ 1214b. The panels identities are identical to Figure 3-6. Observational errors were modeled for 10 transit observations with *JWST*. The narrow posterior distributions for the mixing ratios of H_2O, CO_2, CH_4, and N_2 indicate that unique constraints on the abundance of these gases can be retrieved in agreement with the atmospheric parameters used to simulate the input spectrum. N_2 can be identified to be the main constituent of the atmosphere due to its effect on the mean molecular mass and the Rayleigh signature. While atmospheric models with $X_{H_2} \approx 0.1 \ldots 1\%$ are favored by the synthetic observations, atmospheric models with $X_{H_2} \to 0$ retain a significant probability and no lower bound on X_{H_2} can be found. The most likely value for the surface pressure is in agreement with the surface pressure parameter used to simulate the input spectrum, suggesting that the atmosphere is optically thin at some wavelengths. The synthetic observations are not sufficient, however, to find a statistically significant upper limit on the surface pressure and fully exclude a thick envelope.

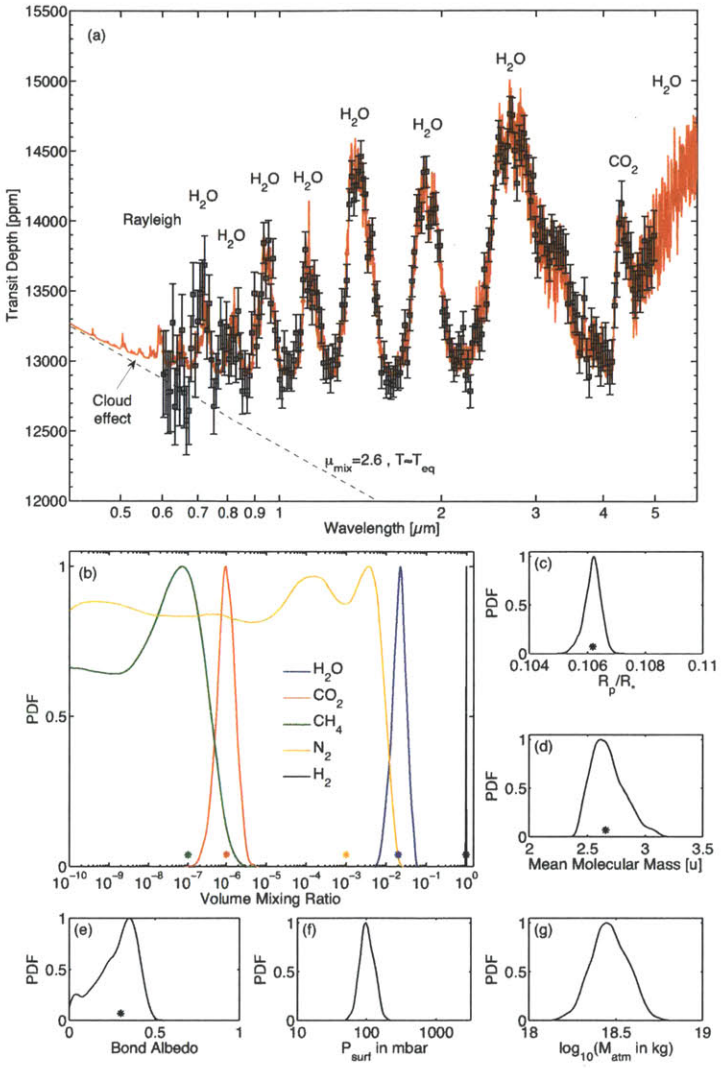

Figure 3-8: Synthetic transit observations and atmospheric retrieval results for the "Hot mini-neptune" scenario of a super-Earth with the physical properties of GJ 1214b. The panels identities are identical to Figure 3-6. Observational errors were modeled for a single transit observation with *JWST* NIRSpec. Note the difference in the scale of the transit depth axis compared to Figures 3-6 and 3-7. The narrow posterior distributions for the mixing ratios of H_2O, CO_2, and H_2 indicate that unique constraints on the abundance of these gases can be retrieved in agreement with the atmospheric parameters used to simulate the input spectrum. Based on the low mean molecular mass, H_2 can clearly be identified as the main constituent of the atmosphere. N_2 mixing ratios larger than a few percent can be excluded. An upper limits at the ppm level can be found for the mixing ratio of CH_4. A surface (here: due to the opaque cloud deck) can be identified at a pressure level between 65 and 150 mbar with 3σ confidence.

albedo and mean molecular mass.

A higher mixing ratio of H_2 lowers the mean molecular mass without creating new absorption features. An atmosphere with more H_2 and less of the main constituent (here: H_2O) in conjunction with an increased planetary albedo shows virtually the same transmission spectrum as the one shown in Figure 3-6. As a result, the posterior distribution shows a significant correlation between X_{H_2} and the Bond albedo as well as between X_{H_2} and X_{H_2O} (Figure 3-9).

3.4.4 Elemental Abundances

The ability to constrain the mixing ratios of both the absorbing and the spectrally inactive gases in the atmosphere provides us with the opportunity to probe the relative abundances of the volatile elements H, C, O, and N of the atmospheres of exoplanets. Conceptually, the retrieval of the elemental abundances in the atmosphere is directly linked to the retrieval of the molecular mixing ratios, since the constraints on elemental abundances are derived from the probability density distribution of the molecular mixing ratios (Section 2.7). Following the result in the previous subsections, low-noise observations of moderate to high spectral resolution lead to well-constrained molecular mixing ratios and therefore also allow determination of well-constrained elemental abundances.

For quantitative constraints, we return to our three scenarios for hot super-Earth atmospheres. The transmission spectra can clearly discriminate the different relative abundances of the volatile elements in the three scenarios (Figure 3-10) and may be used to probe their formation history and evolution. The hot mini-Neptune scenario can be identified to have accreted and retained a primordial atmosphere dominated by hydrogen, similar to gas and ice giants in our solar system. At the other end of the parameter space, the elemental composition of the second scenario indicates an atmospheric composition dominated by nitrogen. The third scenario shows an atmosphere that has retained some hydrogen in heavier molecular species.

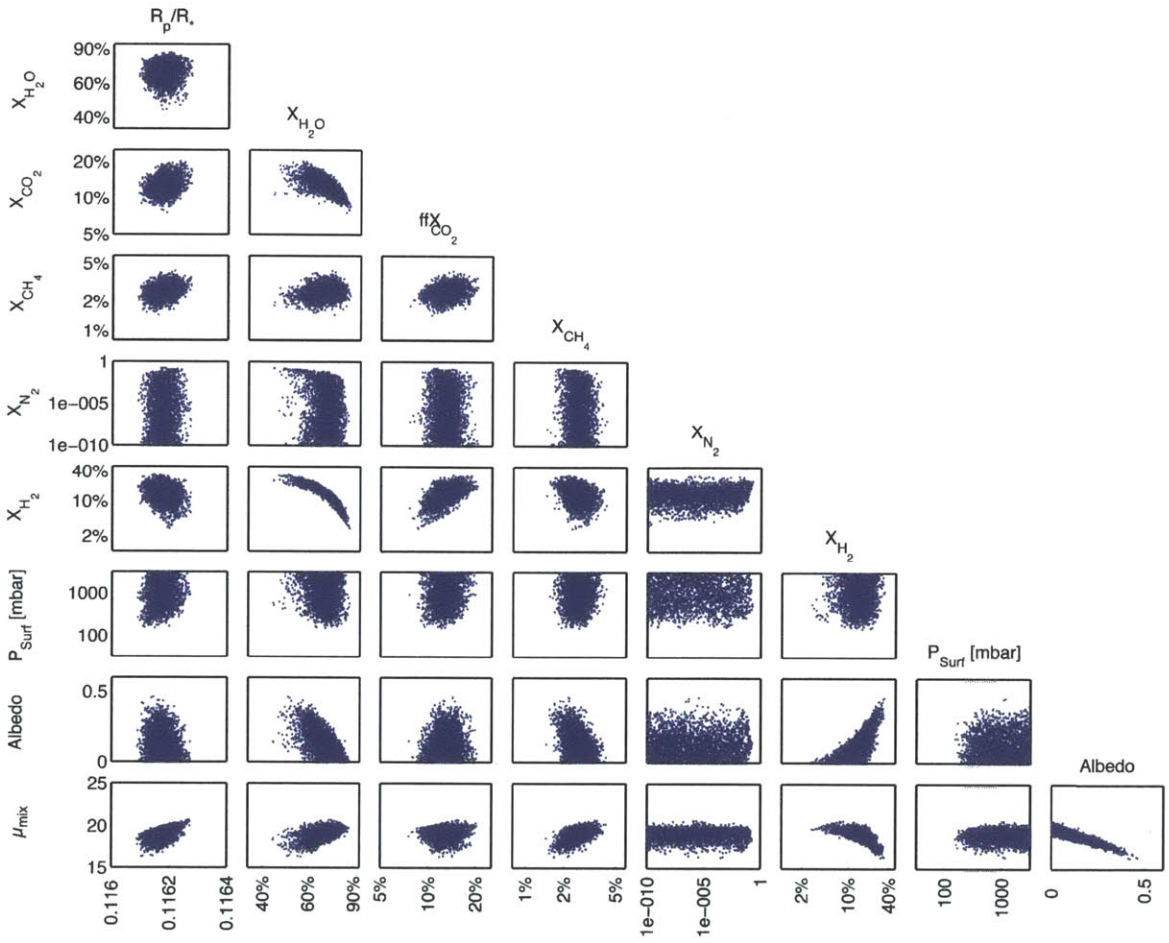

Figure 3-9: Two-dimensional marginalized probabilities for pairs of atmospheric properties for simulated *JWST* NIRSpec observations of the "Hot Halley world" scenario for GJ 1214b. The synthetic observation used for the atmospheric retrieval is illustrated in Figure 3-6. For observations that cover all $n + 4$ observables discussed in Section 3.2, the posterior distribution of the atmospheric parameters retrieval lacks degeneracies or strong correlations that would keep individual parameters unconstrained over orders of magnitude (Figure 3-9). Planetary albedo and the mean molecular mass show a correlation because different combinations of atmospheric temperature and mean molecular mass may lead to the same scale height and, therefore, to similar spectral feature shapes.

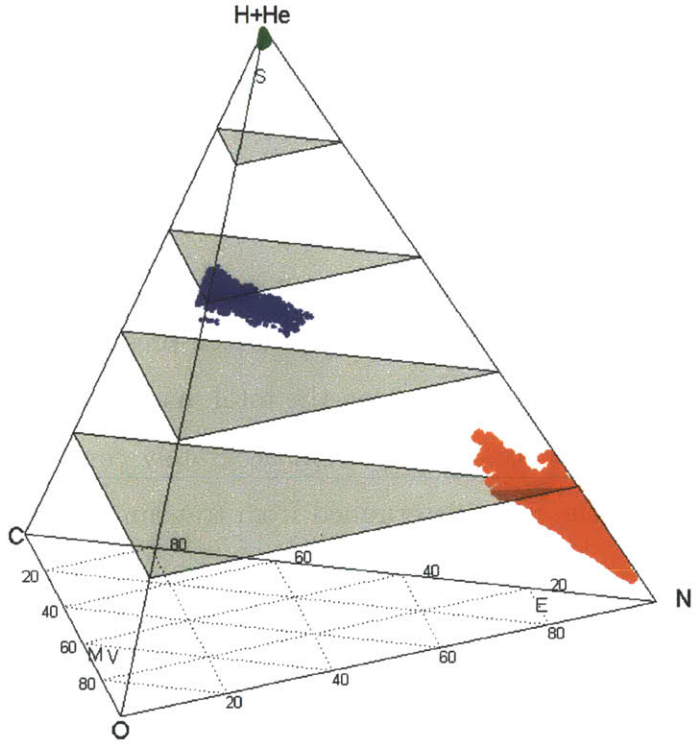

Figure 3-10: Quaternary diagram illustrating the posterior probability distributions for the relative abundances of the elements H, C, O, and N. The colored volumes represent the 2σ Bayesian credible regions of the elemental composition for the "hot Halley world" (blue), the "hot nitrogen-rich world" (red) and the "hot mini-Neptune" (green). The symbols E, M, V, and S indicate the elemental abundances in the atmospheres of the Solar System planets Earth, Mars, Venus and Saturn, respectively, for comparison. The four vertices of the diagram represent an atmosphere that is fully composed of H, C, O, or N. The opposing faces are surfaces on which the fraction of H, C, O, or N is zero. At each point inside the tetrahedron, the elemental fraction is given by the distances perpendicular to the faces.

3.4.5 Total Atmospheric Mass

We find that transmission spectra present an opportunity to determine a lower limit for the total mass of the atmosphere of extrasolar planets based purely on observations. Conceptually, the constraints on the total atmospheric mass are derived from the constraints on the composition and the surface pressure of the atmosphere. The ability to constrain mixing ratios of both the absorbing and the spectrally inactive gases in the atmosphere enables us to constrain the mean molecular mass and therefore the mass density in the atmosphere as a function of pressure. Combined with the independent constraints on the surface pressure, we can integrate the mass density to estimate the total column density of the atmosphere. Under the assumption of an approximately uniform bulk composition and surface pressure around the spherical planet, we therefore obtain a constraint on the total mass of the atmosphere.

Two fundamental limits prevent one from accurately constraining the total atmospheric mass. First, the mass determined from transmission spectra corresponds to the total atmospheric mass above the uppermost surface (see Figure 3-8(f) for a quantitative example). Second, following the arguments on the retrieval of the surface pressure (Section 3.2.4), we will not be able to detect the uppermost surface explicitly if the cloud-free part of the atmosphere is sufficiently thick (Figures 3-6 and 3-7). In conclusion, we can always determine a lower limit on the atmospheric mass once we have detected spectral features, but determining an upper limit is only possible if the atmosphere is sufficiently thin for the surface to be detected and an opaque cloud deck can be excluded from theoretical principles.

3.5 Discussions

3.5.1 Non-Unique Constraints for Hazy Atmospheres

Photochemically-produced hazes may have a significant opacity at short wavelengths and may mask the signature of molecular Rayleigh scattering if they are present in the upper atmosphere, . While we may still be able to probe the near-infrared spectrum

and identify molecular absorbers, we will not be able to probe the transit depth offset of Rayleigh scattering due to *molecular* scattering. Without making further assumptions, we will, therefore, lose the ability to constrain the mixing ratio of the molecular species over orders of magnitude, even for the major constituents of the atmosphere (see Section 3.2).

By measuring either the slope of the Rayleigh scattering signature or the shapes of molecular absorption features, we will still obtain information on the scale height of the atmosphere and, therefore, obtain an estimate on the mean molecular mass (Section 3.2.2). We will not, however, be able to constrain the total amount of the spectrally inactive gases. Since the near-infrared spectrum only constrains the *relative* abundances of the *absorbing* gases (Section 3.2.1), we can hypothesize different atmospheric mixtures of H_2, N_2, and absorbing gases in the correct ratios that produce nearly identical transmission spectra. As a result, we obtain a degeneracy that prevents us from constraining the molecular abundances uniquely.

One assumption that could be made to compensate for the lack of information is to not consider the simultaneous presence of nitrogen gas, N_2, and hydrogen gas, H_2. In general, however, the simultaneous presence of N_2 and H_2 cannot be excluded, even though the preferred chemical form of the two elements N and H in chemical equilibrium is ammonia NH_3 at a wide range of temperatures and pressures because the energy barrier for the reaction is too large due to strong triple bonds in nitrogen molecules.

3.5.2 Stratified Atmospheres

Our parameterization of the atmosphere in the retrieval process assumes a well-mixed atmosphere. Given the limited amount of data available in the near-future, the motivation for the assumption of well-mixed atmospheres is to keep the number of free parameters, which make use of similar information in the spectrum, small. Observations of the Solar System planets justify the approach because $\gtrsim$95% of the gas in each of the Solar System atmospheres is composed of long-lived, chemically stable species that were mixed by turbulence and diffusion for a sufficiently long time (see Lodders

& Jr, 1998; Pater & Lissauer, 2010, and reference therein). If exquisite observations become available in the future, however, it may be useful to extend the parameterization to retrieve compositional gradients. For some molecular species, such gradients may be identified as biomarkers caused by sources at or in the planetary surface.

Physical effects that lead to compositional stratifications of the gaseous species in the Solar System atmospheres are (1) condensation of gases that condense at pressure and temperature levels encountered in the atmosphere, or (2) production or destruction of gas by photochemistry or geology, or (3) variation of chemical equilibrium with altitude due to the altitude dependencies of pressure and temperature. Changes of gas concentration with altitude that are caused by condensation, however, are usually not relevant for our retrieval because transmission spectroscopy only probes layers above the condensation clouds. Similarly, strong changes in the chemical equilibrium usually occur at deep levels in thick envelopes that are unlikely to be probed in transmission. In addition, the mixing ratios of gases that do vary with altitude often only vary over less than one order of magnitude, e.g., CO, H_2O, SO_2 in the atmosphere of Venus (Hunten, 1983). Observational data that are less noisy than the synthetic *JWST* observations considered in Section 3.4 are necessary to robustly detect such gradients because the retrieved mixing ratios for minor species in the synthetic *JWST* observations are uncertain to within one order of magnitude, even for well-mixed atmospheres (Section 3.4). Photochemistry or surface sources, however, may lead to concentration gradients that are substantial at pressure levels probed by transmission spectroscopy (e.g., ozone in Earth's atmosphere) and may justify extensions to our parameterization in the future.

For atmospheres with a stratified composition, our retrieval method determines an altitude-averaged mixing ratio that best matches the observed transmission spectrum. In test cases, we verified that the atmospheric retrieval method remains robust in providing a reasonable estimate for the mixing ratios for stratified atmospheres. We simulated transmission spectra for stratified atmospheres and performed the retrieval assuming a well-mixed atmosphere (Figure 3-11). We found that, the method remains robust and the retrieved mixing ratios for stratified gases correspond to the mixing

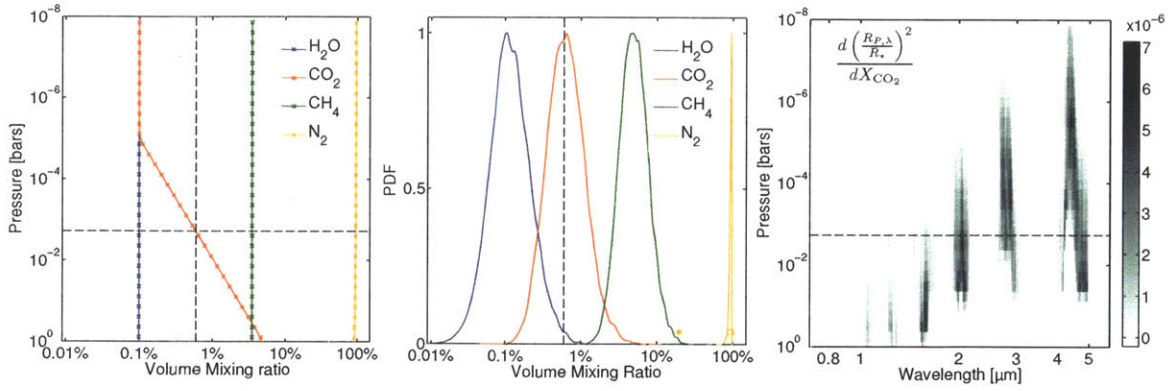

Figure 3-11: Atmospheric retrieval for stratified atmospheres. The left panel illustrates the volume mixing ratio profiles used to simulate the synthetic *JWST* observations for a stratified atmosphere scenario. In this scenario, the volume mixing ratio X_{CO_2} is chosen to decrease log-linearly from 5% at 1 bar down to 0.1% at 0.01 mbar. The error bars of the observations are similar to ones in Figure 3-7 (synthetic observations are not shown). The middel panel illustrates the marginalized posterior probability density as obtained when performing atmospheric retrieval on the synthetic observations. The abundances of all molecular species are robustly retrieved. The most likely value for X_{CO_2} matches the value at the 1-10 mbar level because the functional derivatives—averaged across the observed spectrum—are highest for this pressure level (right panel).

ratios at the pressure levels at which the functional derivatives with respect to the mixing ratio are the highest. Using the functional derivatives, we can, therefore, estimate a posterior at which pressure level we have probed the atmospheric mixing ratio of the gas.

3.6 Summary and Conclusion

In this work, we have applied the retrieval method to synthetic observations of the super-Earth GJ 1214b. We investigated which constraints on the atmospheres of super-Earth exoplanets can be inferred from future observations of their transmission spectra. Our most significant findings are summarized as follows.

- A *unique* constraint of the mixing ratios of the absorbing gases and up to two spectrally inactive gases is possible with moderate-resolution ($R \sim 100$) transmission spectra, if the spectral coverage and S/N of the observations are

sufficient to quantify (1) the transit depths in, at least, one absorption feature for each absorbing gas at visible or near-infrared wavelengths and (2) the slope and strength of the *molecular* Rayleigh scattering signature at short wavelengths. Assuming that the atmosphere is wellmixed, and that N_2 and a primordial mix of H_2 + He are the only significant spectrally inactive components, one can therefore uniquely constrain the composition of the atmosphere based on transit observations alone.

- We can discriminate between a thick, cloud-free atmosphere and an atmosphere with a surface, where the surface is either the ground or an opaque cloud deck. For an atmosphere with a surface at low optical depth, we can quantitatively constrain the pressure at this surface. A unique constraint of the composition is also possible for an atmosphere with a surface.

- An estimate of the mean molecular mass made independently of the other unknown atmospheric parameters is possible by measuring either the slope of the Rayleigh scattering signature, the shape of individual absorption features, or the relative transit depths in different features of the same molecular absorber. For super Earths, discriminating between hydrogen-rich atmospheres and high mean molecular mass atmospheres is, therefore, possible, even in the presence of clouds.

- Determining the volume mixing ratios of the absorbing gases relies on observations of the molecular Rayleigh scattering signature. Although the presence of most molecular species can be identified in the near-infrared, only the relative abundances of the absorbing molecules can be determined from the infrared spectrum, not their volume mixing ratios in the atmosphere. The Rayleigh signature of molecular scattering is required because it enables the measurement of the abundances of spectrally inactive gases. If the molecular Rayleigh scattering cannot be observed or is masked by haze scattering at short wavelengths, we will not be able to determine the volume mixing ratio of the gases in the atmosphere to within orders of magnitude. The drastic inability to constrain the

mixing ratio was not discovered in previous work on atmospheric retrieval because hot Jupiters were assumed to be cloud-free and the mean molecular mass in a hydrogen-dominated atmosphere was known a priori (e.g., Madhusudhan & Seager, 2009).

- The retrieval of the mixing ratios of spectrally inactive gases is fundamentally limited to two independent components. An inherent degeneracy arises if the atmosphere contains three or more independent spectrally inactive gases because the same mean molecular mass and the same strength of the Rayleigh scattering signature can be obtained with different combinations of the gases.

- Non-Gaussian treatments of the uncertainties of atmospheric parameters are essential for atmospheric retrieval from noisy exoplanet observations. Even given low-noise synthetic observations as considered in this work, only one-sided bounds and highly non-Gaussian correlations exist for some atmospheric parameters. Non-Gaussian effects will become stronger for observational data sets noisier than the synthetic data considered in this work because the relation between the observables and the desired atmospheric parameters is highly nonlinear and larger volumes of the parameter space become compatible with noisier observations. A limitation of optimum estimation retrieval (Lee et al., 2011; Line et al., 2012) for the analysis of noisy exoplanet spectra is, therefore, that the extent of the confidence regions of atmospheric properties cannot correctly be described by Gaussian errors around a single best-fitting solution.

Our findings indicate that the retrieval method presented here, combined with low-noise observations, will provide the opportunity to observationally characterize atmospheres of individual super-Earth planets and uniquely identify their molecular and elemental compositions. Similar to observational constraints on the atmospheres of the Solar System planets obtained over the last decades, the quantitative constraints obtainable with our atmospheric retrieval will generally be independent of preconceived ideas of atmospheric physics and chemistry as well as planet formation scenarios and atmospheric evolution. The unbiased constraints can, therefore, motivate the

detailed study of the new phenomena in atmospheric dynamics and chemistry, identify habitability and biosignatures, or provide clues to planet formation and atmospheric evolution.

Chapter 4

Distinguishing between Cloudy Neptunes and Water or Ice-Rich Planets

One of the most profound questions about the newly discovered class of low-density super-Earths is whether these exoplanets are predominately hydrogen-dominated sub-Neptunes or icy worlds planets with envelopes rich in water vapor or other ices. Transit observations of the super-Earth GJ 1214b rule out cloud-free hydrogen-dominated atmospheres but are not able to determine whether the lack of deep spectral features is due to high-altitude clouds or the presence of a high mean molecular mass atmosphere. Here we demonstrate that one can unambiguously distinguish between cloudy sub-Neptunes and water- or ice-rich worlds based on the differences in the wing slopes and relative feature depths of molecular absorption bands in their NIR transmission spectra. We suggest that the observational distinction can be achieved efficiently for super-Earths orbiting M-dwarfs by observing strong water absorption bands near the peak of the M-dwarf's photon flux spectrum ($\lambda \approx 1\,\mu$m) at moderate resolution ($R \sim 50 \ldots 100$). In a numerical retrieval study of synthetic transmission spectra, we show that a strong detection of a clear water vapor atmosphere on GJ 1214b will be possible if the observational error bar can be reduced by a factor of 2 to 3 compared to the published *HST WFC3* and *VLT* transit observations. We discuss that

the required reduction in observational uncertainty may be achievable with currently available instrumentation by stacking repeated transit observations. We provide a scaling law that scales our quantitative results to other transiting super-Earths or Neptunes.

4.1 Introduction

Super-Earth exoplanets, with masses between 1 and 10 Earth masses, lie in the intermediate mass range between terrestrial planets and gas/ice giants in the solar system. Compelling questions arise as to the composition and nature of these objects and whether they are capable of harboring life. According to theoretical studies, (e.g., Seager et al., 2007; Rogers & Seager, 2010a; Nettelmann et al., 2011) many super-Earth exoplanets show a bulk density that is high enough to require a larger ice or rock fraction than the solar system ice giants, but far too low to be explained by an entirely Earth-like rocky composition. Rogers & Seager (2010b) showed that their bulk density may, instead, be explained by either planets that have accreted and maintained a thick H_2/He envelope atop an ice and rock core or, alternatively, by a new class of "water worlds" which contain a large fraction of water or ices in their interior and are surrounded by a dense water vapor atmosphere (Kuchner (2003) and Léger et al. (2004)).

One way of answering questions about the nature and habitability of super-Earths is to identify their atmospheric thicknesses and molecular compositions by observing their transmission and/or thermal emission spectra. Miller-Ricci et al. (2009) showed that cloud-free, hydrogen-dominated atmospheres would display absorption features in the transmission spectrum that are several times larger than those expected for atmospheres dominated by H_2O, N_2 or CO_2 due to the lower mean molecular mass and resulting larger scale height.

Many observational attempts to detect an atmosphere around the super-Earth GJ 1214b and characterize its composition have been made, but the individual observational data sets were found to be insufficient to identify the presence of atmospheric

features to within observational uncertainty (Bean et al., 2010; Désert et al., 2011; Crossfield et al., 2011; Bean et al., 2011; Berta et al., 2012) . An initial finding of a difference in the transit depths between the J and Ks band by Croll et al. (2011) could not be confirmed by Bean et al. (2011).

The absence of deep features in the transmission spectrum of GJ 1214b excludes the presence of a cloud-free hydrogen-dominated atmosphere, but the obtained observational data were shown to be compatible with high mean molecular mass atmospheres, such as water vapor-dominated atmospheres, as well as with a hydrogen-dominated atmosphere in the presence of high altitude clouds (Berta et al., 2012). The interpretation of the observational data for GJ 1214b revealed the limitations of the absorption feature depths as a measure of the atmosphere's hydrogen content in the presence of clouds.

For general atmospheres that may contain clouds, Benneke & Seager (2012) showed the unambiguous effect of the mean molecular mass $\mu_{\rm ave}$ on the transmission spectrum is not the overall depths of the molecular features, but the gradient $dR_{P,\lambda}/d(\ln\sigma_\lambda)$ with which the observed planetary radius $R_{P,\lambda}$ changes as the atmospheric opacity σ_λ changes across the spectrum:

$$\mu_{\rm ave} = \frac{k_B T}{g}\left(\frac{dR_{P,\lambda}}{d(\ln\sigma_\lambda)}\right)^{-1} \times \left(1 \pm \frac{\delta T}{T}\right). \tag{4.1}$$

The surface gravity g can be determined directly from the transit light curve (Winn, 2011), k_B is Boltzmann's constant, and the atmospheric temperature T can be approximated by the equilibrium temperature or modeled by a radiative-convective model. The term $(1 \pm \delta T/T)$ accounts for the inherent uncertainty on the mean molecular mass due to the uncertainty, δT, in estimating the temperature T at the planetary radius $R_{P,\lambda}$.

In practice, an estimate of the mean molecular mass can be determined at visible or NIR wavelengths by measuring the slope of molecular feature wings or comparing the relative transit depths in two or more absorption features of the same molecule. The decrease in opacity σ_λ from the center of the absorption features to wing can be

modeled based on molecular line list of the absorber.

Measuring the slope of gaseous Rayleigh scattering signature at UV/visible wavelengths also provide constraints on the mean molecular mass; however, cloud and haze opacities can mask the signature of gaseous Rayleigh scattering and the distinction between a shallow slope due to a high mean molecular mass or clouds may be difficult.

Equation (4.1) demonstrates that, if sufficient observations of the transmission spectrum are available, the mean molecular mass can determined to the same relative precision as that at which we are able to estimate the temperature T. Since the mean molecular mass varies by a factor of ~ 8 or more between hydrogen-rich atmospheres and atmospheres dominated by water vapor or other ices, we can distinguish between cloudy hydrogen-rich and water-rich atmospheres even if the temperature T is known only with an uncertainty of several tens of percent.

The ability to measure the mean molecular mass at NIR wavelengths is of particular interest for the near-term characterizations of super-Earths because planets orbiting small M-dwarfs are the ones with the strongest transit signatures and are most amenable to study at infrared wavelengths due to the low stellar flux of M-dwarfs at short wavelengths. In this work, we demonstrate using quantitative simulations that NIR transit observations near the peak of the stellar spectrum of M-stars provide a practical means to distinguish between cloudy hydrogen-dominated atmospheres and water- or ice-dominated atmospheres. We determine what precision in the transit depth measurements is required (1) to detect the absorption features in the transmission spectrum of a water-dominated super-Earth and (2) to unambiguously distinguish between water-dominated atmospheres and hydrogen-dominated atmospheres based on the different wing slopes of the water absorption bands.

4.2 Method

The main goal of this work is to determine what precision in NIR super-Earth transmission spectra is required to unambiguously distinguish between hydrogen-dominated and water- or ice-rich atmospheres. We address this question by computing

synthetic transit observations derived from super-Earth model transmission spectra and analyzing them using a Bayesian atmospheric retrieval framework (Chapter 2).

We use the 1D exoplanetary atmosphere "forward" model to compute model transmission spectra and synthetic observations. Our model uses line-by-line radiative transfer in local thermodynamic equilibrium, hydrostatic equilibrium, and a temperature-pressure profile consistent with the atmospheric composition.

The input to the atmospheric "forward" model is an adaptable set of free model parameters describing the gas composition and aerosol properties in the model atmosphere. A difference between the model used in Benneke & Seager (2012) is that the aerosols considered in this work encompass small particles hazes as well as larger cloud particles. Absorption and scattering of the particles are modeled using Mie theory for spherical particles (Hansen & Travis, 1974). The complex refractive indices of the condensates species used in this work (Potassium Chlorid (KCl) or Zinc Sulfide (ZnS)) are taken from Querry (1987).

Synthetic observations are generated by first specifying the chemical composition and aerosol opacities of the individual atmospheric layers. Synthetic observations are then derived from the model transmission spectra by integrating the model spectra over flat instrument response functions with spectral coverage equivalent to the spectral points from the *VLT* observations by Bean et al. (2010) and the *HST WFC3* observations byBerta et al. (2012). Gaussian noise ranging from ~ 180 ppm down to ~ 45 ppm is added to the data to generate synthetic observations of different precision.

The three main scenarios we aim to unambiguously distinguish in this work are hydrogen-rich atmospheres with high-altitude clouds, water- or ice-rich atmospheres, and planets with flat transmission spectra due to the lack of atmospheres or the presence of an extremely high cloud decks that mask all molecular absorption. As representative examples for the three scenarios, we select a methane-depleted solar composition atmosphere with a water mole fraction of 400 ppm and high altitude clouds at 5 mbar pressure, a clear water-dominated atmosphere composed of 95% H_2O and CO_2, and a featureless spectrum. The level of the high altitude clouds in the solar composition scenario is chosen such that the overall depths of the absorption

features resemble that of a clear water-rich atmosphere. Methane is removed from the atmospheric scenario to demonstrate that the distinction between water-rich scenarios and the hydrogen-rich scenarios is possible based solely on the wing steepnesses and relative sizes of the water features.

The atmospheric scenarios for the synthetic observations are chosen to be plausible scenarios, but are not calculated from a fully self-consistent model. The goal of this work is to demonstrate the retrieval for exoplanetary atmospheres for which we do not have a full understanding of the physical and chemical effects prior to the observations. A selection of the resulting spectra and synthetic observations are shown in Figures 4-3(a, c, e), 4-4(a) and ??(a, b) .

4.3 Results: Analysis of Synthetic Super-Earth Observations

Our main result is that an unambiguous distinction between a cloudy hydrogen-rich atmosphere and a clear water-dominated atmosphere will be possible for a GJ 1214b-like planet if the observational uncertainty in the transit depth measurements can be reduced by a factor of 2-3 compared with the published observations by Bean et al. (2010) and Berta et al. (2012). We suggest that the distinction may be achievable by stacking ten or more repeated transit observations with currently available instrumentation if the observational uncertainties continue to scale as one over the square of the number of transit observations (see Section 4.5.2 for a discussion). The results can be generalized to other super-Earths using a scaling law provided in Section 4.5.1. For clarity, we assume gray clouds in Section 4.3 and show the general validity of the results for non-gray clouds in Section 4.3.1.4.

4.3.1 Distinction based on NIR water absorption features

4.3.1.1 Detectability of Water Absorption Features

The distinction between hydrogen-rich atmospheres and water- or ice-dominated atmospheres based on water absorption features requires a strong confidence that an observed transit depth variation is indeed caused by absorption of water vapor. For GJ 1214b, we find that a strong detection of water vapor ($\sim 5\sigma$) in a clear water-dominated atmosphere is possible if the observational error bar of observations as performed by Bean et al. (2010) and Berta et al. (2012) can be reduced from the currently published ~180-200 ppm to ~90 ppm at a resolving power of $\lambda/\Delta\lambda = 70$ (Figure 4-1). The detection significances of molecular features then scales approximately with the inverse of the error-bar of the observations. In other words, reducing the observational uncertainty by a factor of two results in a doubling of the detection significance for the same object and same atmospheric scenario.

For the following discussions, we take synthetic observations of a water-rich atmosphere (95% H_2O + 5% CO_2) on GJ 1214b as our example data set (see Figure 4-3(a)) The assumed uncertainty of the spectral data points is 90 ppm, as may be achieved by stacking 12 transit observations as performed using the VLT by Bean et al. (2010) and using HST WFC3 Berta et al. (2012). Stacking 12 transit observations would enable the inference of water absorption at 5.55σ (Figure 4-2(b) and Table 4.1). The Bayes factor between the cloud-free water model and the flat spectrum is found to be $4.51 \cdot 10^{10}$ for this baseline case, clearly favoring the clear model over the null hypothesis of a flat spectrum (Table 4.1).

Methane and water have two strongly overlapping absorption bands at 1.15 μm and 1.4 μm. The overlap covers most of the spectral range of the WFC3 bandpass and can provide a significant obstacle when characterizing exoplanets in this wavelength range. An unambiguous detection of water vapor does not only require the detection of the absorption bands, but also to distinguish whether the absorption was caused by water, methane, or both. Distinction is possible based on the difference at $\lambda > 1.6\,\mu$m, the exact shape of the absorption features, and the different opacities in the bandpass

of the VLT observations. It is obvious, however, that better observations are required to distinguish between a water absorption and the similarly shaped methane features than is necessary to distinguish between water absorption and a flat spectrum.

The Bayesian framework presented in Section 2.4.2 inherently accounts for the overlap between water and methane absorption features. It assigns a high probability for the presence of water vapor only if the observed feature resembles the expected shapes for a water features considerably closer than it resembles the expected shapes of methane features. Taking again the example of our 90 ppm synthetic observations (Figure 4-3(a)), we find that our confidence in having detected water absorption is lowered by the possibility that methane is responsible for the absorption features. The Bayes factor between an atmosphere with water absorption and an atmosphere without water but with methane and clouds is found to be 10^7, considerably smaller than $4.51 \cdot 10^{10}$ for the Bayes factor between a water vapor atmosphere and a flat spectrum model. The largest portion of the false detection probability for water is caused by the alternative hypothesis that methane absorption has led to the features (Figure 4-2). If methane was not considered as an alternative explanation in the prior hypothesis space, the detection significance for water absorption in our baseline synthetic data set would increase from 5.5σ to 6.65σ. For observations with larger observational uncertainties this effect can make the difference of whether water absorption can be claimed with high significance or not. At 130 ppm, for example, the detection significance of water absorption would be 4.4σ when methane absorption is not accounted for, but only 3.54σ when methane is considered an alternative explanation for the data.

4.3.1.2 Distinction of H_2-dominated and H_2O-dominated atmospheres

An efficient strategy to distinguish between cloudy hydrogen-rich atmospheres and a water- or ice-rich atmospheres is to observe the shapes of the molecular absorption bands near the peak of stellar spectrum at moderate spectral resolution ($R \sim 100$). The shape information of individual absorption bands provides independent constraints on the scale height and cloud-top pressure, thus enabling one to distinguish

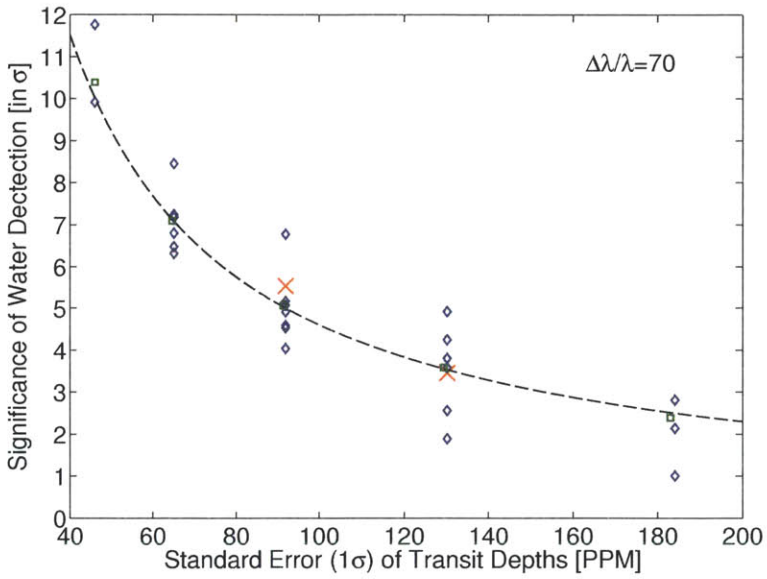

Figure 4-1: Significance of water detection as a function of the observational uncertainty for synthetic observations of GJ 1214b with a water-dominated atmosphere. The spectral coverage of the synthetic observations used for the estimations of the detection significances is $0.78 - 1.0\,\mu$m and $1.1 - 1.7\mu$m, equivalent to the spectral observations by Bean et al. (2010) and Berta et al. (2012). The resolving power is $\lambda/\Delta\lambda = 70$. Each marker indicates the detection significance for a realization of . The two red crosses highlight the synthetic observations displayed in Figures 4-3(a) and 4-4(a). At each level of uncertainty, several realizations were generated to illustrate the natural variations in the inferred detection significance due to the random scatter of the face values. The green diamonds indicate special cases for which the face values of the synthetic observations were set equal to the transmission model output without random scatter. A reliable detection of water absorption ($\gtrsim 5\sigma$) will be possible for water-dominated atmospheres on GJ 1214b if the error bar can be reduced to 90 ppm at $\lambda/\Delta\lambda = 70$.

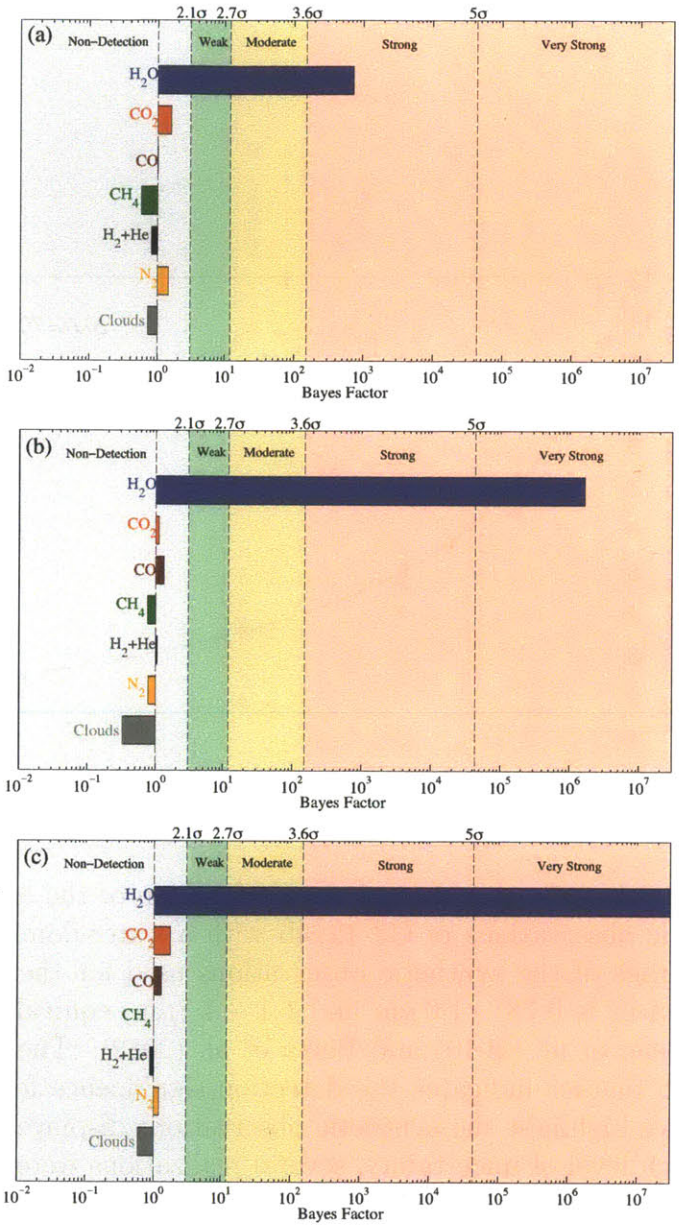

Figure 4-2: Bayes factors as measures of detection confidences for molecular gases and clouds for the three synthetic sets of transit observations of water-dominated scenario for GJ 1214b. The observational uncertainty of the synthetic data points are σ =120, 90, or 45 ppm for panels (a),(b), or (c) respectively. The synthetic data sets for panel (a) and (b) are shown in Figures 4-3(a)), and 4-4(a)), while the low-noise synthetic data set for panel (c) is not displayed. The horizontal bars illustrate the Bayes factor between a Bayesian retrieval model that includes the molecular species (or type of aerosol) and a less complex retrieval that does not consider the molecular species. Water vapor can be detected at $> 5\sigma$ significance for observations with error bars below 90 ppm at $R = 70$. The presence of 5% CO_2 cannot be detected even at $\sigma = 45$ ppm because water absorption masks the absorption of CO_2 between 0.8 and 1.8 μm.

Retrieval model	Retrieval model parameters	Evidence $\ln(\mathcal{Z}_i)$	Best-fit $\chi^2_{\mathrm{best-fit}}$	Bayes factor $B_i = \mathcal{Z}_0/\mathcal{Z}_i$
Full hypothesis space	$\frac{R_p}{R_*}$, P_{clouds}, $\boldsymbol{\xi} = \mathrm{clr}(X_{\mathrm{H_2O}}, X_{\mathrm{CO_2}}, X_{\mathrm{CH_4}}, X_{\mathrm{CO}}, X_{\mathrm{H_2+He}}, X_{\mathrm{N_2}})$	-266.49	15.61	Ref.
H_2O removed	$\frac{R_p}{R_*}$, P_{clouds}, $\boldsymbol{\xi} = \mathrm{clr}(X_{\mathrm{CO_2}}, X_{\mathrm{CH_4}}, X_{\mathrm{CO}}, X_{\mathrm{H_2+He}}, X_{\mathrm{N_2}})$	-280.80	43.55	$1.63 \cdot 10^6$ (5.7σ)
CO_2 removed	$\frac{R_p}{R_*}$, P_{clouds}, $\boldsymbol{\xi} = \mathrm{clr}(X_{\mathrm{H_2O}}, X_{\mathrm{CH_4}}, X_{\mathrm{CO}}, X_{\mathrm{H_2+He}}, X_{\mathrm{N_2}})$	-266.59	16.54	1.11
CH_4 removed	$\frac{R_p}{R_*}$, P_{clouds}, $\boldsymbol{\xi} = \mathrm{clr}(X_{\mathrm{H_2O}}, X_{\mathrm{CO_2}}, X_{\mathrm{CO}}, X_{\mathrm{H_2+He}}, X_{\mathrm{N_2}})$	-266.77	15.70	1.31
CO removed	$\frac{R_p}{R_*}$, P_{clouds}, $\boldsymbol{\xi} = \mathrm{clr}(X_{\mathrm{H_2O}}, X_{\mathrm{CO_2}}, X_{\mathrm{CH_4}}, X_{\mathrm{H_2+He}}, X_{\mathrm{N_2}})$	-266.21	15.62	0.76
N_2 removed	$\frac{R_p}{R_*}$, P_{clouds}, $\boldsymbol{\xi} = \mathrm{clr}(X_{\mathrm{H_2O}}, X_{\mathrm{CO_2}}, X_{\mathrm{CH_4}}, X_{\mathrm{CO}}, X_{\mathrm{N_2}})$	-266.54	15.71	1.05
H_2 + He removed	$\frac{R_p}{R_*}$, P_{clouds}, $\boldsymbol{\xi} = \mathrm{clr}(X_{\mathrm{H_2O}}, X_{\mathrm{CO_2}}, X_{\mathrm{CH_4}}, X_{\mathrm{CO}}, X_{\mathrm{H_2+He}})$	-266.24	15.65	0.77
Clouds removed	$\frac{R_p}{R_*}$, $\boldsymbol{\xi} = \mathrm{clr}(X_{\mathrm{H_2O}}, X_{\mathrm{CO_2}}, X_{\mathrm{CH_4}}, X_{\mathrm{CO}}, X_{\mathrm{H_2+He}}, X_{\mathrm{N_2}})$	-265.37	15.76	0.33

Table 4.1: Quantitative comparison of retrieval models for synthetic observations of the water-dominated scenario for GJ 1214b, assuming 90 ppm uncertainty in the transit depth measurements. The synthetic observations are depicted in Figure 4-4(a). Values that are directly referred to in Section 3 are marked in bold.

between the cloudy hydrogen-rich atmospheres and a water- or ice-rich atmospheres based on their different mean molecular masses.

Observations with smaller uncertainties are required for the distinction between hydrogen-rich and water-rich atmospheres than are required for the pure detection of the NIR water absorption bands because the distinction is based on the subtle shape information of the absorption bands. Our retrieval analysis of synthetic observations reveals that water-rich and hydrogen-rich scenarios can unambiguously be distinguished at observational error bars that provide a 5-6σ detection of the water absorption feature, while a 3-4σ detection of water absorption can leave the water fraction unconstrained between 100% and a small fractions of 1%.

Taking again our example of synthetic observations of GJ 1214b in the spectral ranges of 0.78-1 µm and 1.1-1.8 µm, we find that observational error bars below 90 ppm at a resolving power of $\lambda/\Delta\lambda = 70$ would suffice to distinguish between a clear water-rich atmosphere and a cloudy hydrogen-rich atmosphere with identical depths in the absorption features, and a featureless spectrum due to the absence of an atmosphere or extremely high altitude aerosols that block any atmospheric signature (Figure 4-3).

Water-dominated scenario. Observations with an observational error of 90 ppm would constrain the water mixing ratio between 55% and 100%, corresponding to a mean molecular weight of >10 (Figure 4-3(a-b)). The lower limit on the cloud-top pressure would be $\sim$ 10 mbar at 3σ. The posterior probability density would be maximum for water fractions above 90% and cloud top pressures above 100 mbar. Changes in the observable transmission spectrum are negligible if the water fraction is increased above 90% because the mean molecular mass remains largely unchanged. An increase in cloud top pressure, similarly, has negligible effects on the observable spectrum because the opacity is significant throughout the spectral range covered, preventing us from probing deeper layers through transmission spectroscopy.

Hydrogen-rich scenario with high-altitude clouds. For a cloudy, hydrogen-rich scenario with feature depths similar to a water-dominated scenario (Figure 4-3(c-d)), observations with an error bar of 90 ppm would constrain the water mixing ratio between 0.002% to 40% at 95% confidence. In other words, the mean molecular mass can be constrained to within 2.319 and 7. The observations at 90 ppm would also require the presence of an upper cloud deck with a cloud-top pressure between 0.2 mbar and 200 mbar at 95% confidence.

Stronger independent constraints on water mixing ratio would not be available despite the clear detection of water absorption because of a strong correlation between the water mixing ratio and the cloud-top pressure. The strong correlation is present because model atmospheres with different combinations of mean molecular masses and cloud-top pressures can lead to identical feature depths. The effect of the mean molecular mass on the feature shape is sufficient, however, to exclude scenarios with mean molecular masses above approximately 7, and thus to exclude water- or ice-dominated scenarios.

Featureless spectra. A planet's transmission spectrum may be featureless if the planet lacks a gaseous atmosphere or clouds are presents at high altitude. For such planets with featureless spectra, observations with an observational uncertainty of

90 ppm would be sufficient to exclude the presence of cloud-free, water-rich atmospheres at high significance (Figure 4-3(e-f)). The posterior probability of atmospheric models would significant only for cloud top pressures below 1 mbar, for the all water mixing ratios between solar composition ($X_{H_2O} \sim 0.04\%$) and water-dominated ($X_{H_2O} \rightarrow 100\%$). The observations would additionally rule out scenarios with cloud-top pressures down to 0.01 mbar for water mixing ratios between 1% and 10%.

4.3.1.3 Weak Constraints on Water Abundance Despite Clear Detection of Water Absorption

At larger observational uncertainties (Figure 4-4), a clear distinction between hydrogen-dominated and water-dominated atmospheres may be impossible despite a 3-4σ detection of water absorption. While the detection of water relies on the combined information from observations across a relatively wide spectral range, e.g., from 1.3-1.5 μm for the water feature centered 1.4 μm, the distinction between hydrogen-dominated and water-dominated relies on the subtle shape information of the features. Observations with a higher precision at sufficient resolution are, therefore, required to resolve the shape of the features and enable the distinction between water-dominated and hydrogen-dominated atmospheres based on mean molecular mass.

Taking the example of a water-dominated scenario observed at 120 ppm uncertainty (Figure 4-4(a)), we find that the detection of the presence of water would still be possible, however, we would not be able to distinguish between cloud-free, water-rich atmospheres and cloudy, hydrogen-rich atmospheres. Observations that provide a detection of the water absorption feature at low significance (here: 3.5σ) lead to a characteristic correlation between water mixing ratio (or mean molecular mass) and cloud top pressure (Figure 4-4(b)). High posterior probabilities exist along a line of constant feature depth because the feature depths are constrained relatively well by the observations. In the hydrogen-rich regime, the feature size remains constant along lines of constant water column density. The cloud-top pressure compatible with the synthetic observations decreases as the water mixing ratio in the atmosphere is increased (negative correlation). In the transition region between 10% and 90% water

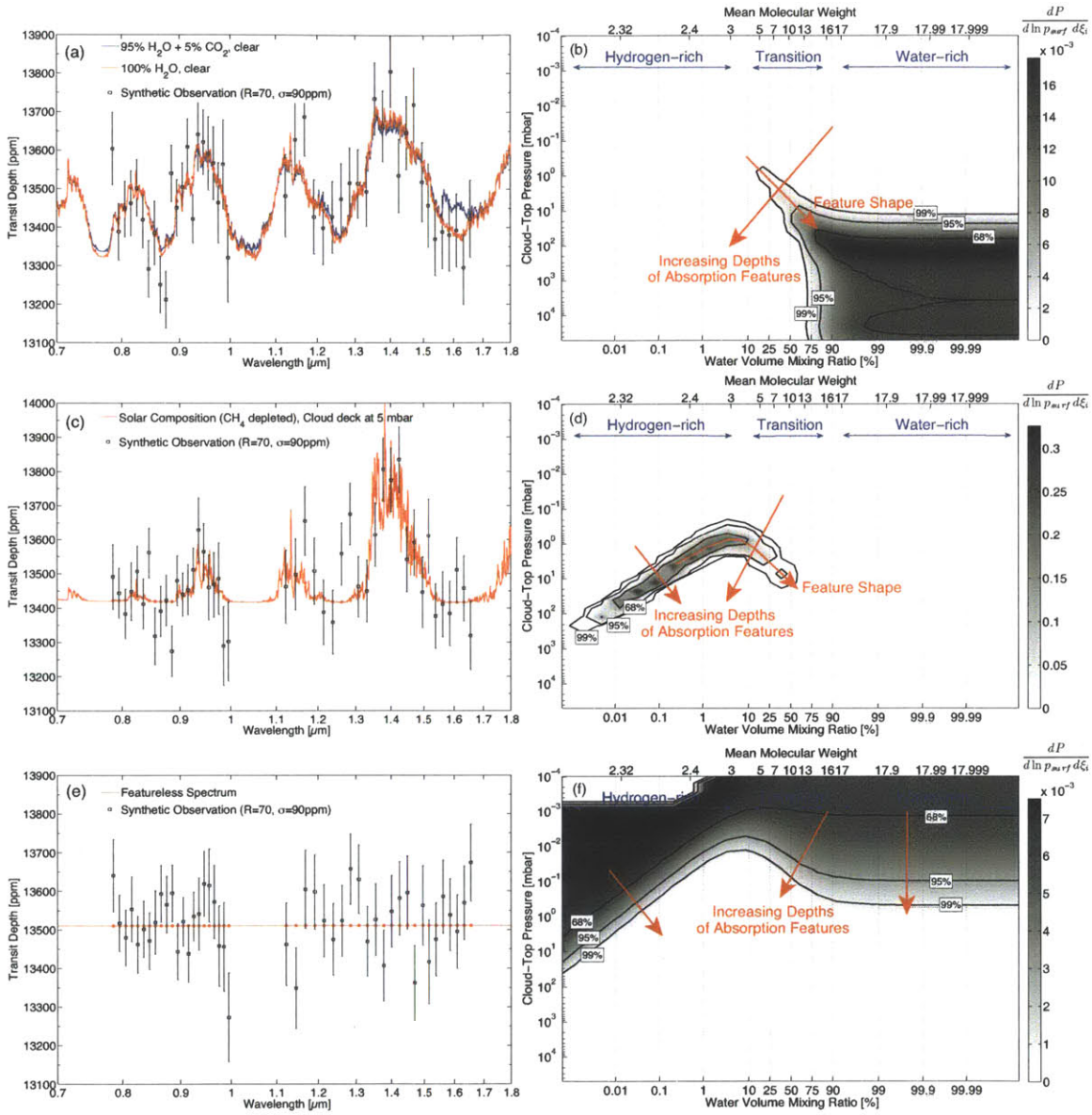

Figure 4-3: Distinguishing between water-dominated atmospheres and cloudy, hydrogen-dominated atmospheres based on their transmission spectra. Model spectra and synthetic observations with an observational error bar of 90 ppm are displayed for a clear water dominated atmospheres (Panel (a)), a cloudy, hydrogen-dominated atmosphere (Panel (c)), and a featureless spectrum (Panel (e)). Panels (b),(d),(f) illustrate the marginalized posterior probability as a function of water volume mixing ratio (or mean molecular mass) and cloud top pressure for atmospheric mixtures of H_2O and H_2. The black contour lines indicate the 68%, 95%, and 99% Bayesian credible regions retrieved from the synthetic observations. The gray shading illustrates the regions of high posterior probability density. The horizontal axes is scaled as the centered-log-ratio parameter $\xi_1 = \log\left(X_{H2O}/\sqrt{X_{H2O} \cdot X_{H2}}\right)$ (Benneke & Seager, 2012). The prior probability is uniform in the parameter space spanned by $\log\left(p_{surf}\right)$ and ξ_1. Transmission spectra as published by Bean et al. (2010) and Berta et al. (2012) but with observational uncertainties of 90 ppm would enable to distinguish whether GJ 1214b is surrounded by a clear water-rich atmosphere or a cloudy, hydrogen-dominated atmosphere.

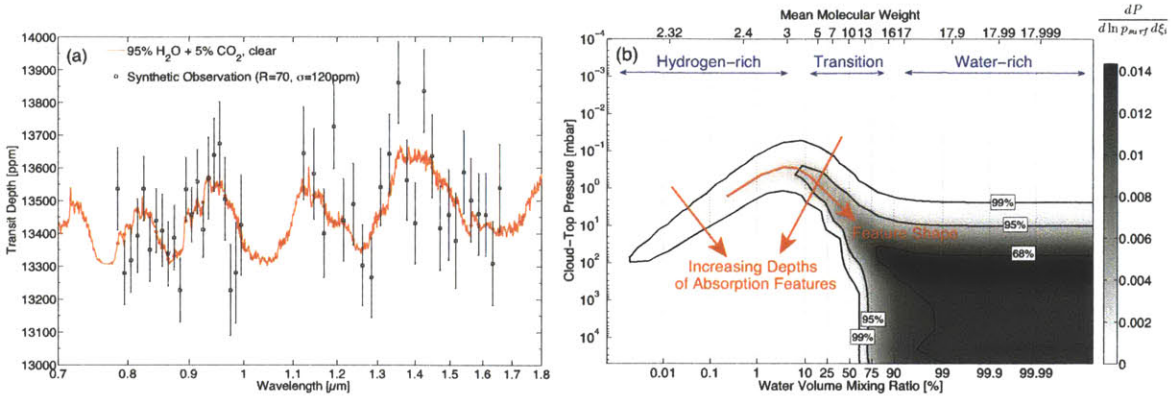

Figure 4-4: Weak constraints on the water-to-hydrogen ratio despite a 3.5σ detection of water absorption in the synthetic data set. The model spectrum and synthetic observations for a water-dominated scenario for GJ 1214b are displayed in panel (a). The spectral coverages of the individual channels are identical to Figure 4-3(a), however, the uncertainty in the synthetic observation is increased to 130 ppm, corresponding to stacking of only 6 independent transit observations. The constraints on retrieved atmospheric constraints in panel (b) are plotted as described in Figure 4-3. A robust distinction between hydrogen-dominated and water-dominated atmospheres is not possible, despite a 3.54σ detection of water absorption (Figure 4-2(a)). The noisy synthetic observation lead to a characteristic degeneracy between the mean molecular mass (or water mixing ratio) and the cloud-top pressure. Model spectra along a contour of constant absorption feature depths are in agreement with the synthetic observations. The 130 ppm synthetic observation do not provide sufficient information to constrain the mean molecular mass based slope of the absorption band wings at high significance.

mixing ratio, the change in the mean molecular mass dominates the change in the feature size. Maintaining the same feature sizes requires higher cloud top pressures as the water fraction is increased (positive correlation). Changes in feature size are small if the water mole fraction is increased above 90% because the mean molecular mass remains largely unchanged and deeper layers in the atmosphere are optically thick independent of the exact water mole fraction.

4.3.1.4 Effects of Non-Gray Aerosols

In Section 4.3.1, we made the assumption of gray clouds when we demonstrated the distinction between clear water-rich atmospheres and cloudy hydrogen-rich atmospheres. Here, we model cloud scattering using Mie theory and demonstrate that the fundamental approach of determining the mean molecular mass based on wing slopes of molecular absorption bands or by comparing features of the same absorber

remains viable in the general case of non-gray aerosols. We find that the cores of molecular absorption bands in transmission spectra are largely unaffected by the type and spectrum of the particles. The molecular absorption bands provide unambiguous constraints on the mean molecular mass as long as there is a significant detectable molecular absorption feature penetrating the "continuum" spectrum of the haze or cloud particles.

We demonstrate the unambiguity of the wing slopes and relative sizes of absorption features as a measure of mean molecular mass by presenting two representative spectra of hydrogen-rich atmospheres with high altitude hazes and comparing them to cloud-free water atmospheres (Figure 4-5). We consider haze high-altitude particles composed of condensed Potassium Chlorid (KCl) or Zinc Sulfide (ZnS) as two potential explanation that would mute the spectral features of a hydrogen-rich atmosphere. The condensation temperature of KCl and ZnS are between 500 K and 700 K at pressures below 100 mbar (Morley et al., 2012). KCl and ZnS may therefore condense in the upper atmosphere of GJ 1214b.

There is no straightforward way of predicting the particle size distributions of KCl and ZnS condensates in the upper atmosphere of widely uncharacterized exoplanets. For demonstrative purposes we present transmission spectra of atmospheres with KCl and ZnS condensation particles with mean particle radii of 0.3 μm and 1 μm, respectively (Figure 4-5). The aim is to present two plausible scenarios that show the insensitivity of the proposed approach to estimate the mean molecular mass to the assumption of gray clouds. The sizes of the particles were selected to obtain haze spectra that do considerably deviate from the assumption of gray clouds while simultaneously allowing a reasonable fit to previously obtained transit depth measurements. Particles smaller than 0.3 μm would increasingly lead to steep slopes at near-infrared wavelengths. Larger particles would lead to an increasingly gray appearance of the clouds in transmission, and thus, brings us back to the assumption made in Section 4-5. We set the upper end of the haze layer at 5 mbar to obtain hydrogen-rich scenarios that show water absorption features with transit depth variations similar to the ones of water worlds. Scenarios with similar transit depths variations are the ones most

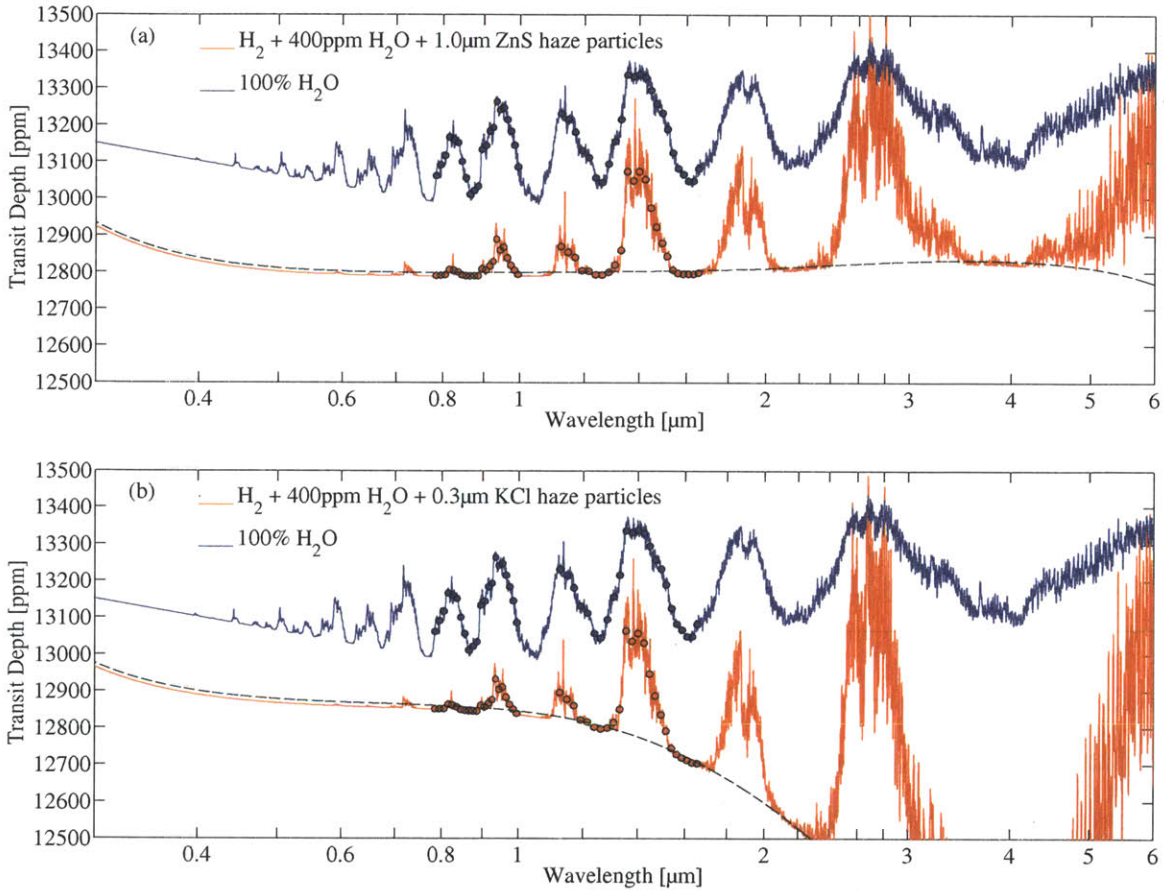

Figure 4-5: Comparison of model transmission spectra of water worlds and cloudy sub-Neptunes with non-gray high-altitude clouds. The red model spectra in panel (a) and (b) are model spectra for two alternative scenarios for hydrogen-rich atmospheres with thin, high-altitude hazes on GJ 1214b. Panel (a) assumes ZnS particles with a mean radius of 1 μm, while panel (b) assumes KCl particles with a mean radius of 0.3 μm. The particles sizes and cloud top pressure (5 mbar) are chosen such that the main water features in the HST WFC3 are of similar size as the ones predicted for water vapor atmospheres (blue spectra). The non-gray effects of the hazes only are shown by the black dashed spectra for which the gaseous absorption was set to zero. The cores of the strong molecular absorption features remain largely unaffected by the non-gray effects of the hazes. The steepness of the feature wings and the relative depths between different absorption features remain measures of mean molecular mass, even in the presence high-altitude non-gray hazes, as long as significant absorption features can be observed. The spectra are offset for clarity by slightly modifying the planet's radius at the reference pressure level ($p = 10\,\mathrm{mbar}$).

difficult to distinguish from clear water worlds. The high-altitude hazes are assumed to be thin; the ratio of the condensed mass and the gas mass in the upper atmosphere is 1 ppm. Thin hazes lead to transmission spectra that deviate most strongly from gray clouds.

Figure 4-5 shows that the cores of the strong molecular absorption features are largely unaffected by wavelength dependence of the aerosols opacity. Estimates of the mean molecular mass made based on the feature cores in transmission spectra are, therefore, largely independent of the spectral properties of the aerosols. The favorable independence between absorption features and the haze properties is present for two reasons. First, for transmission spectra, the observed transit depth at a given wavelength is almost exclusively determined by the strongest opacity source at that wavelength. This is as a result of the grazing geometry in which the transmission spectrum is formed (Brown, 2001), combined with the exponential decrease in gas density with altitude. Second, aerosol opacities generally change more gradually with wavelength than molecular opacities. Molecular opacities at low pressures are dominated by sharp absorption lines and bands that result from quantum mechanical transitions between discrete vibrational and rotational states in the molecules. Light extinction by aerosols, on the other hand, is a result of interference of light that was scattered, refracted, or diffracted by a generally continuous distribution of different particles sizes. Spectral features arise as result of the interference or the wavelength dependence of the complex refractive index; however, the effects on the transmission spectrum are more gradual than molecular state transitions.

The wavelength dependence of condensed phase absorption is less critical for transmission spectra than it is for reflective spectra because, in the transit geometry, a single scattering event will prevent the light beam from the host star to arrive at the observer. The reflective spectrum of clouds, on the other hand, is generally dominated by multi-scattering within the cloud. The long pathways associated with light which is scattered multiple times within in a cloud can result in strong absorption features in reflective spectra of clouds. Water clouds, for example, will appear highly reflective at visible wavelengths for which the imaginary part of the refractive index is low (low

absorption), while it will appear almost black at some near-infrared wavelength for which the imaginary part of the refractive index is high (high absorption). We do not see the strong contrast in transmission spectra.

4.3.2 Distinction based on the Rayleigh Scattering Slope

Observations of the slope of the Rayleigh scattering at short wavelength provide an alternative way of constraining the mean molecular mass. In practice, however, the Rayleigh slope provides only an upper limit on the mean molecular mass due to the potential pressure of clouds or large particle hazes. As a result, a hydrogen-rich atmosphere could be identified if a steep negative slope is observed in the UV-visible part of the transmission spectrum. If there is no steep slope, however, the distinction between hydrogen-dominated and ice-dominated is not possible because the lack of a steep slope at short wavelength may due to a high mean molecular mass or the presence of large particle clouds. The upper limit on the mean molecular mass can be therefore be determined as

$$\mu_{\rm mix} \lesssim \frac{4k_BT}{gR_*} \frac{\ln\left(\frac{\lambda_1}{\lambda_2}\right)}{\left(\frac{R_p}{R_*}\right)_{\lambda_2} - \left(\frac{R_p}{R_*}\right)_{\lambda_1}}, \tag{4.2}$$

where we derived Equation (4.2) from Equation (4.1) using that the Rayleigh cross section σ is proportional to λ^{-4} . We assumed that, at least, two measurements of the transit depth R_p/R_* are available wavelengths λ_1 and λ_2 at which Rayleigh scattering dominates, and we incorporated the uncertainty factor $(1 \pm \delta T/T)$ from Equation (4.2) into the *approximately* smaller sign.

As an example, we consider a haze-free water-rich scenario on GJ 1214b in comparison to a range of hydrogen-dominated scenarios with high-altitude KCl hazes with different size distributions (Figure 4-6). In the absence of hazes, the slope of the Rayleigh scattering signature at short wavelength can determined from Equation (4.2) using an "approximately equal" sign instead of the "approximately smaller" sign. In the presence of the KCl hazes, however, the slope at short wavelength depends not

only on the mean molecular mass, but also on the size distribution of the haze particles, the vertical extend of the particles, and the amount of condensed mass. The slope is therefore not an unambiguous measure of the mean molecular mass. For haze particles small compared to the wavelength, the slope of the Rayleigh signature remains unchanged. As the haze particle become bigger, the slope decreases if the particles are present at high altitude in sufficient abundance. In the limit of gray, large particle clouds, more and more of the spectrum becomes flat.

An upper limit on the mean molecular mass can be determined based on a detection of straight Rayleigh signature at UV-visible spectrum because, at least in the limits of Mie scattering theory of spherical particles, the opacities of particles do not change steeper than $\sigma \propto \lambda^{-4}$ for any realistic particle size distributions. Besides, we are not aware of any condensate substances for which changes in the real or imaginary refractive index at UV-visible wavelengths would steepen the slope across a significant portion of the UV-visible spectrum. As a result, haze particle tend to flatten the UV-visible transmission spectrum and do not steepen it.

4.3.3 Probing the Molecular Abundances in Ice-rich Atmospheres

The distinction between H_2-dominated sub-Neptunes and water or ice-rich worlds described in Section 4.3.1 and 4.3.2 is solely based on the sharp contrast in molecular masses between hydrogen gas (H_2) and the ices (H_2O, CO_2, CO, CH_4, N_2, etc). The basic argumentation is that primordial H_2-dominated scenarios can be excluded if the mean molecular mass deviates significantly from $\mu_{ave} = 2.3 \ldots 3$. Measuring the mean molecular mass, however, does not unambiguously determine what the abundances of the individual ices species in the atmosphere are.

Figure 4-7 illustrates the difficulty in determining the mole fraction of the individual ice species for two vastly different atmospheres with identical molecule mass ($\mu_{ave} = 23.2$). Following the argumentation in Benneke & Seager (2012), the relative abundances of the ices that have IR absorption features, e.g., H_2O, CO_2, CO,

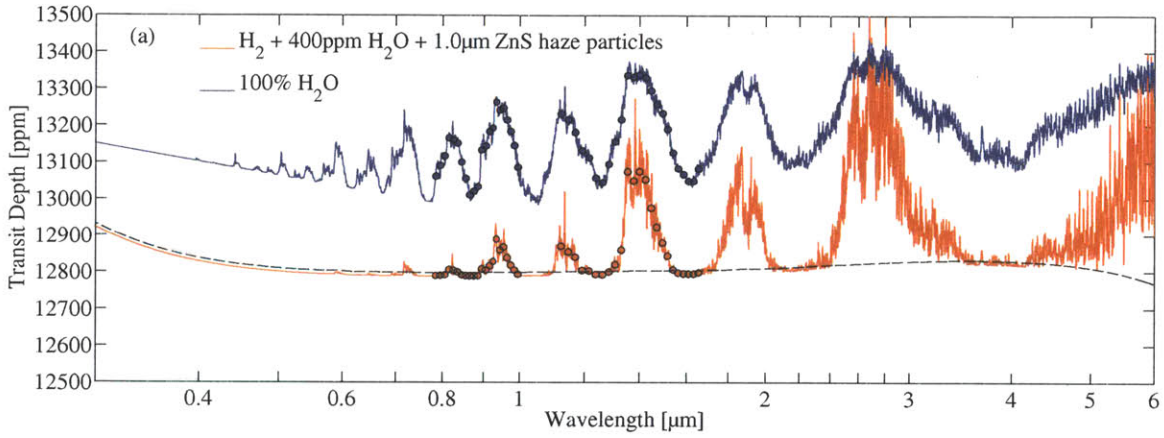

Figure 4-6: Comparison of model transmission spectra of water worlds and cloudy sub-Neptunes with non-gray high-altitude clouds. The red model spectra in panel (a) and (b) are model spectra for two alternative scenarios for hydrogen-rich atmospheres with thin, high-altitude hazes on GJ 1214b. Panel (a) assumes ZnS particles with a mean radius of 1 μm, while panel (b) assumes KCl particles with a mean radius of 0.3 μm. The particles sizes and cloud top pressure (5 mbar) are chosen such that the main water features in the HST WFC3 are of similar size as the ones predicted for water vapor atmospheres (blue spectra). The non-gray effects of the hazes only are shown by the black dashed spectra for which the gaseous absorption was set to zero. The cores of the strong molecular absorption features remain largely unaffected by the non-gray effects of the hazes. The steepness of the feature wings and the relative depths between different absorption features remain measures of mean molecular mass, even in the presence high-altitude non-gray hazes, as long as significant absorption features can be observed.

CH_4, and NH_3 can be determined by comparing the transit depths in the strongest absorption bands of the different ices. An atmosphere with 80% H_2O + 20% CO_2 ($H_2O/CO_2 = 4$), for example, can be distinguished from an atmosphere with 50% H_2O and 10% CO_2 ($H_2O/CO_2 = 50$) because the transit depth within the CO_2 band at 4.3 μm would be higher relative to the transit depths in the H_2O bands.

Scenarios with similar relative abundances of absorbing gases, however, are practically indistinguishable through infrared observations. Figure 4-7 shows that the NIR spectrum of an ice-rich atmosphere can remain virtually unchanged when the mole fraction of water is reduced from 80% to 8% and the mole fraction of CO_2 is reduced from 20% to 2%. Spectrally inactive gases may be present in the correct ratios for the mean molecular mass to remain unchanged. A distinction between 80% water and 8% water therefore required observations at short wavelengths.

Transmission spectra for water-dominated (80% H_2O) and water-rich (8% H_2O)

4.4 Results: Analysis of Published Spectral Observations of GJ 1214b

We now present a retrieval re-analysis of the currently available spectra transit observations of the super-Earth GJ 1214b. The broadband observations (Section 4.1) are not included in this particular retrieval analysis because we require one free offset parameter for each additional data set to account for the offset between different data sets due to brightness variations of the unocculted portion of the stellar disk and different instrumental effects (Berta et al., 2011). The inclusion of a free offset parameters for each data set currently justifies only the use of the two most informative spectral data sets. Single broadband observations, in particular, provide little information when a free offset parameter is included.

Hydrogen-dominated atmospheres are in agreement with the observations only if a hypothetical cloud deck is present at a fine-tuned pressure level (Figure 4-9). Clear atmospheres with hydrogen fraction above 40% ($\mu_{atm} < 11$) are disfavored by the

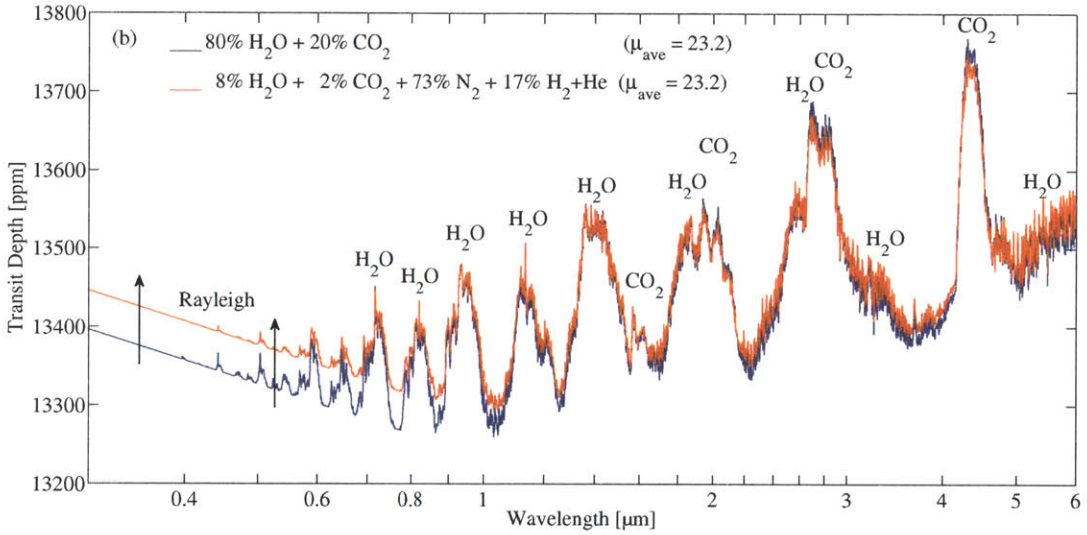

Figure 4-7: Comparison of transmission spectra for a H_2O/CO_2-dominated atmosphere (80% H_2O and 20% CO_2) and H_2O/CO_2-rich, but N_2-dominated atmosphere (8% H_2O and 2% CO_2) with identical mean molecular masses. Despite the vastly different compositions, the planet show virtually identical infrared transmission spectra, because the mean molecular mass and the relative abundances of the absorbers are identical. Distinction is possible only at short wavelength ($\lambda < 1\,\mu$m) based on the increased Rayleigh scattering due to the presence of N_2 and $H_2 + He$. The example that even a strong detection of a water feature is not sufficient to determine whether the atmosphere is dominated by water vapor or only a small fraction of the gas is water vapor.

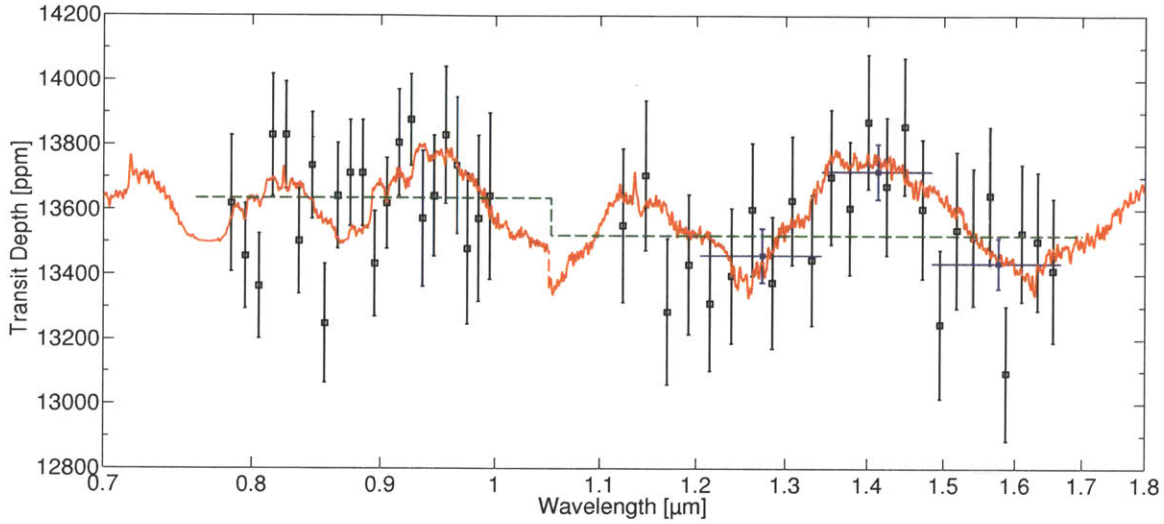

Figure 4-8: Observed transmission spectrum of GJ 1214b compared to model spectra. The VLT observations by Bean et al. (2010) (0.8-1μm) and the HST WFC3 observation by Berta et al. (2012) (1.1-1.7μm) are shown in black. A featureless spectrum (green) and a model spectrum of a 100% water vapor atmosphere (red) are shown for comparison.. Both the model for the flat spectrum and the water atmosphere include a free offset parameter that allows for a relative offset between the HST WFC3 and VLT observations (see step at 1.05 μm). The Bayesian model comparison for the observational data indicates the presence of water absorption at 1.8σ. In the light of the data, the water atmosphere (red) is 14.36 times more likely than the featureless model (green). A model-independent comparison of the transit depth "inside" the 1.4 μm and the transit depth in the surrounding troughs shows a deviation from a flat spectrum at a significance between 1.46σ and 2.65σ, depending on which data points are considered "inside" the feature. The binned data points (blue) would indicate an increased transit depth in the 1.4 μm water feature at a significance of 2.44σ when compared to trough on the long-wavelength side and 2.16σ when compared to the trough on the short-wavelength side. A model-independent approach generally leads to ambiguous detection significances of molecular features because the way the data are binned strongly influences the detection significances (Section 3.4).

data by more than 3σ due to the lack of deep absorption features.

The observed transit spectra by Bean et al. (2010) and Berta et al. (2012) lead to correlated constraints on the mean molecular mass (or water-to-hydrogen ratio) and the cloud top pressure (Figure 4-9) that are characteristic of transit observations that enable a marginal detection of absorption features but do not provide sufficient information on the shape of the feature to constrain the mean molecular mass independently (compare Figure 4-4). High posterior probabilities exist along a curve of constant feature size because the feature sizes are constrained relatively well by the observations. In the hydrogen-rich regime, the feature size remains constant along lines of constant water column density. The cloud-top pressure compatible with the synthetic observations decreases as the the water mole fraction in the atmosphere is increased (negative correlation). In the transition region between 10% and 90% water mole fraction, the change in mean molecular mass dominates the changes in feature size. Maintaining the same feature sizes while increasing the water fraction, therefore, requires an increase of the cloud top pressure (positive correlation). Changes in feature size are small if the water mole fraction is increased above 90% because the mean molecular mass remains largely unchanged and deeper layers in the atmosphere are optically thick and thus independent of the exact water mole fraction. As a result, the probability density remains largely unchanged above water volume mixing ratios of 90%.

Atmospheric scenarios below the region of high posterior probability (bottom left region of Figure 4-9) are disfavored by the observational data because the observed transmission spectra do not show deep absorption features expected for clear hydrogen-rich atmospheres. Hydrogen volume mixing ratios above 40%, corresponding to hydrogen mass ratios above 5%, can be excluded at high significance ($>3\sigma$) unless clouds block the deep feature sizes. Atmospheric scenarios with water fraction between 1% and 10%, corresponding to 90% to 99% H_2, lead to the the largest feature sizes for a given cloud-top pressure. Atmospheric scenarios with water fraction between 1% and 10%, therefore, require the clouds to block the grazing light beam up to the 1 mbar level at high significance ($>3\sigma$).

Conversely, atmospheric scenarios above the region of high posterior probabilities (top region of Figure 4-9) do not explain the suggested transit depth variations and are, therefore, marginally ruled out by the data. The 2σ Bayesian credible region extends to a surface pressure of 10 μbar for water-dominated worlds and reaches up 1 μbar for atmospheres that are composed of 90-99% of hydrogen. In the hydrogen-dominated regime, the 2σ credible region extends to atmospheric models with water partial pressures below 0.01 μbar at the cloud-top.

4.5 Discussion

4.5.1 Scaling Laws for Required Observation Precision

Planet and Star Scenario The quantitative results obtained for the super-Earth GJ 1214b in Sections 4.3.1.1 and 4.3.1 can be generalized for transiting super-Earth exoplanets with different bulk properties and different host stars using the scaling law

$$\frac{\sigma_{required}}{\sigma_{ref}} \approx \frac{R_P}{R_{P,\mathrm{ref}}} \frac{T_{eq}}{T_{eq,\mathrm{ref}}} \frac{g_{P,ref}}{g_P} \frac{R^2_{*,ref}}{R^2_*}, \tag{4.3}$$

where $\sigma_{required}$ is the maximum allowed observational uncertainty in the spectral transit depth measurements, R_p is the planetary radius, T_{eq} is the equilibrium temperature, g_P is the surface gravity of the planet, and R_* is the radius of the host star. Equation (4.3) is derived by relating the area $2R_pH$ of an annulus around the star with a width of one scale height $H \propto T_{eq}/g$ to the cross section of the stellar disk πR^2_*.

Equation (4.3) is valid for clear, hazy, and cloudy atmospheres within only a few percent as long as identical scenarios for the atmospheric compositions and aerosol properties are compared. The simple scaling law is valid for all types of atmospheres because differences between the transit depths observed at two different wavelengths are directly related to the difference in the altitudes Δz at which the atmosphere becomes opaque to grazing light beam at the two wavelengths. The difference in the altitudes Δz, in turn, is related to the pressure scale on which the atmospheric

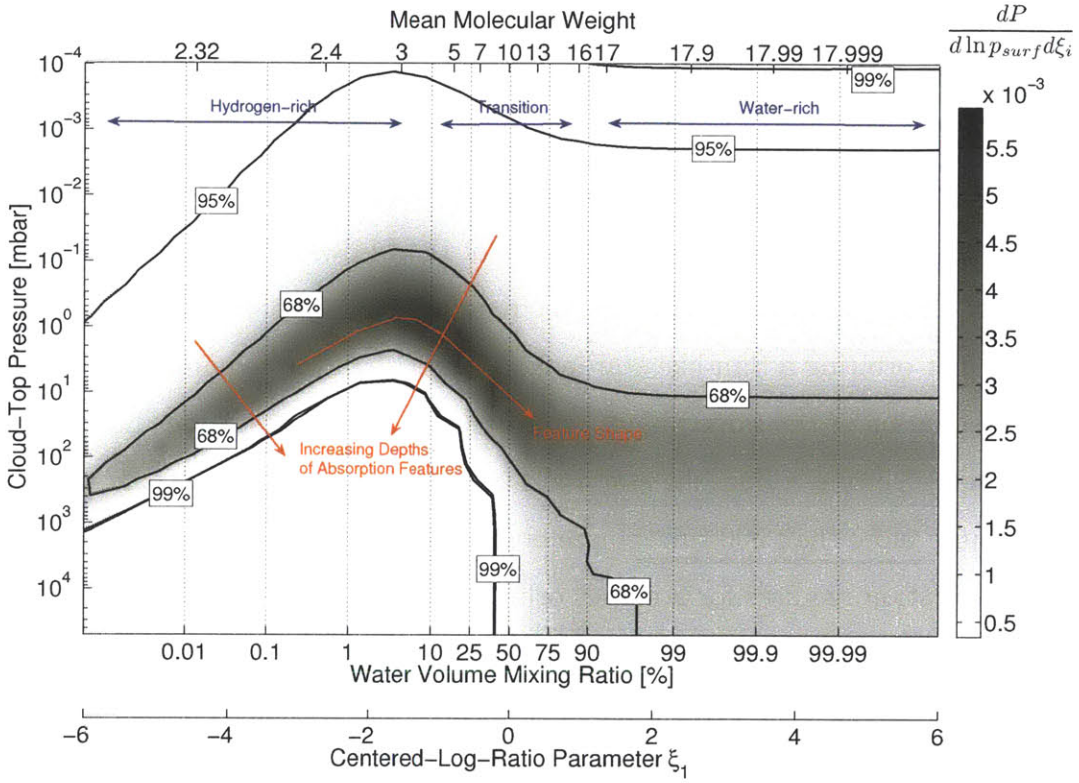

Figure 4-9: Atmospheric constraints derived from the observed transmission spectra by Bean et al. (2011) and Berta et al. (2012). The gray shading illustrates the two-dimensional posterior probability as a function of water volume mixing ratio and cloud top pressure for atmospheric mixtures of H_2O and H_2. The black contour lines indicate the 68%, 95%, and 99% Bayesian credible regions. The 95% Bayesian credible region extends over large parts of the parameter space, preventing an unambiguous characterization of the atmosphere of GJ 1214b with the currently available data. Starting from the most robust statement, we can robustly exclude clear hydrogen-dominated atmosphere with hydrogen volume mixing ratios above 40% at $>3\sigma$. Featureless models with no water absorption ($p_{surf} < 10^{-3}$ mbar) are disfavored by the observational at $\sim 2\sigma$. Both water-dominated and cloudy, hydrogen-dominated atmospheres are, however, in agreement with the data at 1σ due to degeneracy between the water volume mixing ratio and the cloud-top pressure (compare Figure 4-4). The prior probability is uniform in the parameter space spanned by $\log(p_{surf})$, $\xi_1 = \log\left(X_{H2O}/\sqrt{X_{H2O} \cdot X_{H2}}\right)$.

scenarios, e.g., cloud top pressure and compositional profiles, are defined by the $\Delta z = -H \cdot \Delta P/P$. Equation (4.3) does not account for the increase in atmospheric path length of grazing light beams due to an increase planet radius. The longer path length, however, generally leads an approximately uniform increase in transit depths across the spectrum and has little effect of the transit depths variations.

Equation (4.3) shows that the required observational precision depends most strongly on the radius of the host star due to large differences in stellar radii and the square dependence. The stellar radius of the M-dwarf GJ 1214 is only 21.1% of radius of a Sun-like star. As a result, the required photometric precision to characterize a planet orbiting a Sun-like star is 22.5 larger than the required precision for the characterization of the same planet orbiting GJ 1214. Atmospheric characterizations of a planet orbiting a Sun-like star with the same apparent brightness would therefore require more than 500 times more observational time than a similar atmospheric characterization requires for a planet orbiting GJ 1214.

The effect of the atmospheric temperature and planetary radius on the required precision is more subtle and only scales linearly. The required precision for the atmospheric characterization of a moderate temperature, Earth-sized planet orbiting a nearby M-dwarf, for example, is only lower by a factor of a few compared to GJ 1214b (see Section 4.5.3 for a discussion).

Spectral Resolution of Observations The quantitative results on the photometric precision in Sections 4.3.1.1 and 4.3.1 are presented for a resolving power $R = \lambda/\Delta\lambda = 70$. Higher resolution spectra, whose uncertainties are dominated by white noise, can provide the same information, even if the uncertainties of the individual data points are higher. Assuming that the observation uncertainties are dominated white noise, the requirements on the precision of each single data point scale as

$$\sigma_{\mathrm{HR,\,required}} \approx \sigma_{\mathrm{ref}} \sqrt{\frac{\Delta\lambda_{\mathrm{ref}}}{\Delta\lambda_{\mathrm{HR}}}} = \sigma_{\mathrm{ref}} \sqrt{\frac{R_{\mathrm{HR}}}{R_{\mathrm{ref}}}}, \tag{4.4}$$

for $R_{\mathrm{HR}} > R_{\mathrm{ref}}$. Equation 4.4 describes in a formal way that the required precision,

$\sigma_{\mathrm{HR,required}}$, of spectra with a higher resolving power, R_{HR}, can be binned to reduce the observational uncertainty of individual data points to σ_{ref} at a reference resolving power of R_{ref}. The higher resolution spectra, therefore, contain at least as much information about the atmosphere as the spectra with observational uncertainty σ_{ref} and reference resolving power R_{ref}.

Equation 4.4 can be regarded as a conservative scaling law because observations with significantly higher resolving power than $R = \lambda/\Delta\lambda = 70$ may capture individual peaks within the water absorption features that are not captured at low resolution. High resolution observations may therefore provide additional information to better constrain the gradient $dR_{P,\lambda}/d(\ln \sigma_\lambda)$ and thus the mean molecular mass (Equation4.1). We confirm in numerical studies that the Equation 4.4 is valid for resolving power between ~ 50 and several hundreds. A detailed numerical exploration of the effect of the resolving power is beyond the scope of this study.

4.5.2 Uncertainty Reduction through Stacking Transit Observations

In Section 3, we made the assumption that the uncertainty in the spectral data points scales inversely with the square root of the number of observed transits n. Based on the assumption we calculated how many transit observation need to be stacked with published observational techniques to detect water absorption in the atmospheres of super-Earths and to distinguish between hydrogen-rich sub-Neptunes and water worlds. The assumption is true for observational uncertainties that are dominated by white noise, such as photon-noise or stellar granulation noise. Instrumental effects or long-period stellar variability may ultimately set a lower limit on achievable precision for transit observations. To date, however, it is not clear whether and after how many transits the transit depth uncertainty will reach a lower limit.

There is impressive empirical evidence from space-based observatories such as *Kepler*, *Spitzer*, and *HST* that the transit depth uncertainty continues to decrease as the number of stacked transits increases to a few, tens, and even several hundred

transits. A prominent example is the continuous *Kepler* observations of the hot-Jupiter TrES-2b from which the visible broadband transit depth was determined to a precision of 1.7 ppm by combining hundreds of transits (Barclay et al., 2012). Spectroscopic observations of three transits of GJ 1214b using *HST WFC3* by Berta et al. (2012), reaching a precision within 10% of the photon limit, suggest that a similar trend is possible for spectroscopic transit observations. More observations are required to fully understand whether the uncertainty of exoplanet transmission spectra is ultimately limited by instrumental and/or astrophysical noise.

4.5.3 Atmospheric Characterizations of Habitable Worlds around M-dwarfs

The compelling feature of the scaling law (Equation (4.3)) is that the photometric precision required to perform atmospheric characterizations scales only linearly with the atmospheric temperature and planet size. The weak scaling illustrates the great potential for transmission spectroscopy to characterize temperate and small exoplanets (Deming et al., 2009; Seager & Deming, 2010). Transit observations with currently available instrumentation have the potential to characterize the atmospheres of potentially habitable exoplanets orbiting nearby M-dwarfs if observational errors continue to decrease as the number of transits is increased to tens of transits (see Section 4.5.2).

For a super-Earth planet that orbits a GJ 1214-like star in the habitable zone at a moderate temperature of $T_{eq} = 300\,K$, the requirements on observational time will rise by only a factor of $(T_{eq,P}/T_{eq,\mathrm{GJ1214b}})^2 \approx 3.3$ compared to the ones presented in Section 4.3. Given a sufficiently large observational program that covers 40 or more transit we would, in principle, have the capability to find water or methane features with currently available instrumentation assuming that observational uncertainty remains to be dominated by the photon noise. Considering that the orbital period of a temperate planet orbiting a GJ 1214-like star is only ~9 days, 40 transit observations could theoretically be performed over the course of a year. In addition, improved

observational techniques such as the spatial scan mode of *HST WFC3* (Deming et al., 2013 in preparation) can reduce the number of required transits by a factor of a few by increasing the integration efficiency (duty cycle) of the observations from 10% Berta et al. (2012) to several tens of percents or higher. The spatial scan mode of *HST WFC3* was not yet available in 2011 when Berta et al. (2012) performed their transit observation of GJ 1214b.

4.5.4 Controversial Mass and Radius Estimates for GJ 1214b

The quantitative results for super-Earth GJ 1214b were computed using the mass and radius estimates reported by Charbonneau et al. (2009) ($M_P = 6.55\,M_{Earth}$ and $R_P = 2.678\,R_{Earth}$). Private communication with Josh Carter shortly before the submission of this thesis revealed, however, that the planetary mass may be underestimated significantly (Carter et al. 2013, in preparation). Charbonneau et al. (2009) assumed a circular orbit for GJ 1214b when estimating the planetary mass from radial velocity measurements. A reanalysis of the data shows that the orbit of GJ 1214b may be eccentric, changing the derived estimates of the planet's and star's bulk mass and radius. The new analysis suggests that the mass and radius of the planet GJ 1214b are $M_{\rm P} = 8.11^{+0.49}_{-0.48}\,M_{\rm Earth}$ and $R_{\rm P} = 2.41^{+0.14}_{-0.13}\,R_{\rm Earth}$.

The new bulk density $\rho_{\rm P} = 3.1 g/cm^3$ remains in agreement with both hydrogen-dominated gas envelopes and water-dominated gas envelopes, however, the new mass and radius estimates result in smaller atmospheric features. The surface gravity increases from $g_p = 8.96 m/s^2$ to $g_p = 13.7^{+1.6}_{-1.5} m/s^2$ which, in turn, decreases the scale height of the atmosphere and thus decreases the transit depth variation across the spectrum. Following Equation (4.3), all quantitative results presented in Section 4.3 need to be scaled by the factor

$$f = \frac{R_P}{R_{P,\rm ref}} \frac{g_{P,ref}}{g_P} \frac{R^2_{*,ref}}{R^2_*} = \frac{2.41}{2.678} \frac{8.96}{13.7} \frac{0.21^2}{0.189^2} = 0.727 \qquad (4.5)$$

if the finding by Carter et al. (2013, in preparation) are confirmed. The maximum observational uncertainty to distinguish between a cloudy hydrogen-dominated

atmosphere and a cloud-free water-dominated atmosphere would then decrease from 90 ppm to 65 ppm.

4.6 Summary and Conclusions

We proposed to distinguish between cloudy sub-Neptunes and clear high mean molecular mass atmospheres, such as water-dominated atmospheres, by observing the shapes of absorption features at NIR wavelengths. The observational distinction can be achieved efficiently for super-Earths orbiting M-dwarfs by observing spectral features, such as water features, at moderate resolution ($R \sim 50 \ldots 100$) near the brightness peak of the M-dwarf's spectrum. We demonstrated that a reduction of the observational uncertainties in the published *HST WFC3* and *VLT* transit observations by a factor of 2 to 3 would be sufficient to detect a clear water-rich atmosphere on GJ 1214b with high significance. Assuming that the observational uncertainty in the transit depth decreases with the square root of the number of transit observation, we propose that large observational programs of ten or more transits are capable of uniquely distinguishing between a water-rich and cloudy hydrogen-rich atmosphere.

Our results show that observations with currently available instruments should be capable of probing the nature of super-Earth exoplanets such as GJ 1214b, even in the presence of high mean molecular mass atmospheres. Orbiting close to a nearby M-dwarf, the super-Earth GJ1214b is an exceptional member of the super-Earth class for spectroscopic characterizations because the diminutive stellar radius (0.211 $R_{\odot}$) and the high planetary temperature (>500 K) result in relatively large transit depth variations if an atmospheric envelope is present. The atmospheric characterization of other currently known transiting super-Earths, such as 55 Cnc e and Kepler-11e, is significantly more challenging because the larger host star radius decreases the transit signal by a factor of ~20.

Large efforts for the discovery of GJ 1214b analogues are, however, ongoing. Ground-based transit surveys such as MEarth (Nutzman & Charbonneau, 2008) are currently present the most promising pathway to detect super-Earths around nearby

M-dwarfs that are most amenable to study. At the same time, the Kepler mission is enabling the discoveries of hundreds of super-Earths and sub-Neptunes, and the occurrence rates of super-Earths and Earth-sized planets.

If an exoplanet like GJ 1214b is found in the habitable zone of a close-by M-dwarf, this work indicates that we will have the capability to spectroscopically probe the atmosphere of a potentially habitable planet - not only in the next decades with *JWST* or *TPF*-like missions, but today with *HST* and ground-based telescopes.

Chapter 5

Evaluating EChO Science Instrument Configurations

EChO—the Exoplanet Characterization Observatory–is a dedicated mission concept to investigate the atmospheres of transiting exoplanets and is currently under assessment by the European Space Agency. The objective of EChO is to characterize the composition, chemistry, and physical processes in the atmospheres of hundreds of transiting exoplanets, ranging from hot Jupiters to temperate super Earths. The eventual scientific goals are to probe the diversity of planets in our galaxy, understand the formation and evolution of planets, and potentially identify biosignatures. The basic concept for EChO is to offer a stable platform that provides extremely precise and stable spectroscopic observations at visible, near-infrared and mid-infrared wavelengths simultaneously.

The main remaining questions for the conceptual design address EChO's spectral coverage in the mid-infrared as well as the short wavelength cutoff at visible wavelengths. Spectral coverage at mid-infrared beyond $\sim 11\,\mu$m would required cryogenic cooling, affecting the total mission costs by as much as 20%. The short wavelength cutoff sets which material is used to coat the optical surfaces in the telescope and scientific instruments. Determining which design is optimized for exoplanet characterization requires an integrated modeling approach that takes into account the scientific as well as engineering aspects of the mission.

In this chapter, I present an integrated design evaluation framework that simultaneously models the astrophysical signal and the EChO payload module to evaluate the expected science output of EChO as a function of the detector and instrument design parameters. The design evaluation framework is applied to assess and compare the science output of four currently considered designs for the EChO science instrument.

The main findings of the study are that optical surface materials with high reflectivity at short wavelengths (down to 400 nm) are crucial to constrain the molecular composition, metallicity, and elemental abundances of extrasolar planets. The extra costs to enable transit observations beyond $\sim 11\,\mu$m, however, appear not to be justifiable given the limited additional information provided by this wavelength range.

5.1 Introduction

5.1.1 Science Objectives

The main objective of EChO is to identify the nature and atmospheric composition of a representative sample of known transiting exoplanets (Tinetti et al., 2012). The target list will include hot, warm, and habitable-zone planets, ranging from Jupiter-sized planets with equilibrium temperatures T_{eq} up to 2,000 K, to those of a few Earth masses and temperatures as low as $T_{eq} \sim 300\,$K. The concept is optimized for photon-noise limited transit spectroscopy of planets orbiting nearby target stars with stellar types A, F, G, K and M and brightness magnitudes between $K \sim 3-4$ and $K \sim 9-10$. EChO will be the ideal instrument to perform follow-up characterization of transiting planets that may be found by the proposed TESS mission, currently being developed at MIT.

The EChO legacy will be measurements of the atmospheric compositions, elemental abundances, dynamics, and structure in the atmosphere of a representative sample of known exoplanets. The data will help us understand the natures of wide variety of planets without analogues in the Solar System, including the potentially ice-rich,

warm super-Earths such as GJ 1214b, hot lava worlds such as proposed for Corot-7b, and potentially carbon-rich giant planets. The observations will enable us to better understand the interplay between photochemistry, thermochemistry, and transport processes in the atmospheres by constraining models of atmospheric chemistry and dynamics.

EChO observations are expected to fundamentally improve our understanding of planet formation and evolution. EChO will also provide an opportunity to find the first biosignatures on planets outside our Solar System by intensive studies of temperate super-Earths around nearby M-dwarfs. A more detailed discussion of the science objectives of EChO can be found in Tinetti et al. (2012)

5.1.2 Mission Concept

EChO is a proposed M3 mission for the Cosmic Vision 2015-2025 program dedicated to the characterization of transiting exoplanets. The main design driver is the stringent requirement on the photometric stability at a parts-per-million level necessary for precise differential spectroscopy at the visible to mid-IR wavelengths. The requirement on the photometric stability is also the biggest challenge of the EChO mission, as it demands extreme pointing and temperature stability. Additional constraints that need to be taken into account in the design are the mission cost cap of 470M Euros (~$600M USD) and ESA's requirement to launch on a Soyuz-Fregat rocket.

The current concept for the EChO telescope consists of an off-axis, afocal three-mirror Korsch telescope with an effective area of $1.13\,\mathrm{m}^2$. One fundamental strength of the EChO design is that it will simultaneously cover a broad wavelength range from the visible to mid-infrared. The current baseline design goal provides continuous wavelength coverage between 400 nm to $16\,\mu$m at moderate resolution ($R = 300$ for $\lambda \leq 5\,\mu$m and $R = 30$ for $\lambda \geq 5\,\mu$m). The wavelength coverage from 400 nm to $16\,\mu$m was selected in the initial design phase because it covers the main absorption features of the most relevant species (Tinetti et al., 2012).

EChO will host only one spectrometer instrument. The preferred observation mode will be long-time series spectroscopy of point-sources. The spacecraft's stringent

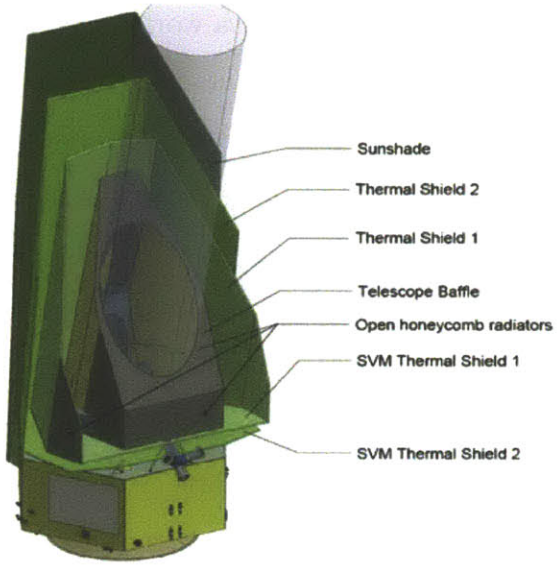

Figure 5-1: EChO spacecraft and thermal shields for passive cooling system design. Figure taken from Tinetti et al. (2012).

pointing and alignment requirements of a few milli-arcseconds (mas) are proposed to be achieved 3-axis stabilized. The stringent pointing requirement can potentially be relaxed using fast fine-steering/tip tilt mirror within the instrument (Figure 5-3). The required thermal environment for the payload module and science instrument will be provided by a multi-layer sunshield (Figure 5-1).

The EChO spacecraft will be placed in an grand halo orbit around L2. The main advantages of placing the spacecraft at the L2 point are the highly stable thermal environment and good visibility of the sky to repeatedly observe several tens of prime targets. The mission lifetime is currently set to 5 years and the proposed launch date is 2022.

5.1.3 Instrument Design

5.1.3.1 Optical Layout

The spectrometer design for EChO is a multi-channel dispersive spectrometer with all reflective optics (Figures 5-2). The design was selected over alternative concepts, such as cross-dispersive spectrometers, static Fourier-Transform-Spectrometers, dynamic

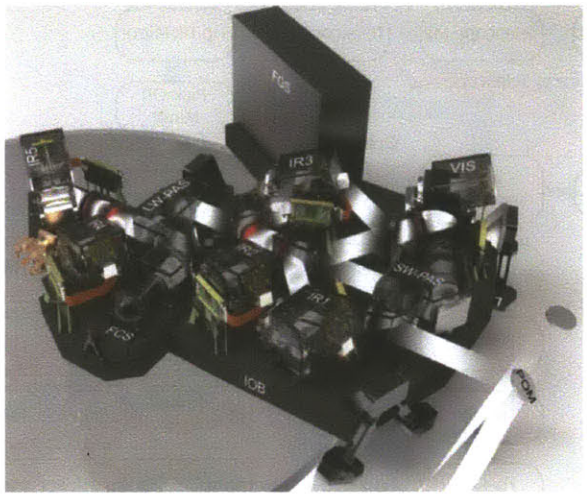

Figure 5-2: Scientific instrument layout for EChO baseline design. The computer rendered illustration shows the geometrical configurations of the spectral channels VIS, IR1, IR2, IR3, IR4, and IR5. Figure adopted from Glauser (2013).

Fourier-Transform-Spectrometers, or fiber-fed pupil spectrometers, because of its low susceptibility to thermal variations (Glauser, 2013).

The path of light entering the science instrument is illustrated in Figure 5-3. The collimated beam from the pick-off-mirror passes through the short-wavelength pupil adapter system (SW-PAS). The SW-PAS provides the appropriate field mask and pupil stop to image the telescope pupil onto the grating of the six channels. It also allows for the injection of light from the short-wavelength flat field calibration (SW-FCS) and provides an invariant interface to the telescope optics.

A series of dichroic mirrors separates and guides each part of the wavelength range to 4-6 dedicated spectrometer channels, depending on the final wavelength coverage. Each spectrometer channel consists of a grating, a three mirror anastigmats camera (TMA) and a focal plane array / detector (FPA). The gratings are used in 1st order spectroscopy to provide the science data and, simultaneously, in 0th order for accurate pointing monitoring.An additional beam splitter is installed in the visible channel to guide part of the visible light to the Fine Guiding System (FGS). Designs with infrared coverage beyond $\sim 10\,\mu$m will host an additional pupil adapter system (LW-PAS) and flat field calibration (LW-FCS) to isolate all long wavelength components in a separate temperature environment.

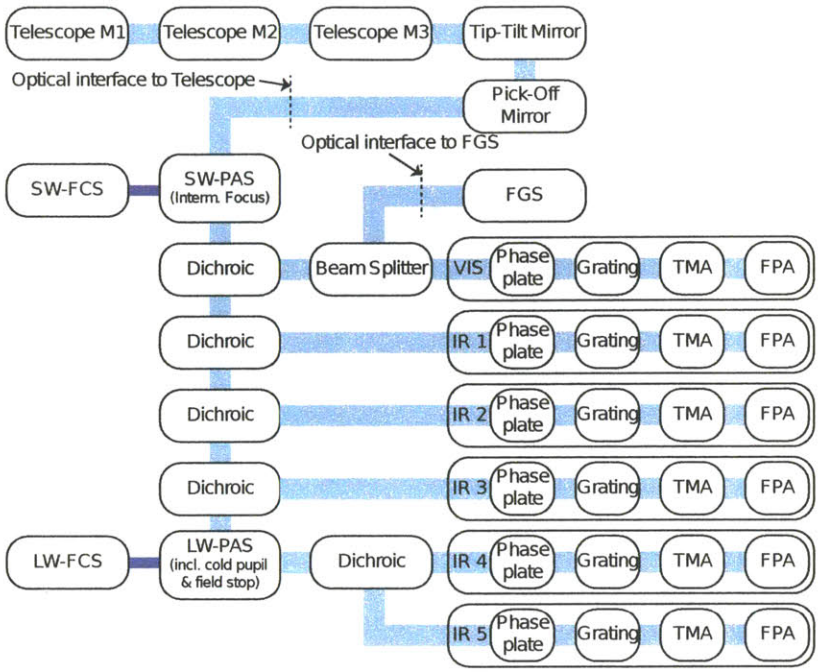

Figure 5-3: Optical architecture for baseline configuration of EChO science instrument. Figure modified from Glauser (2013).

5.1.3.2 Detector Technology

The spectral channels covering the visible and near-infrared wavelengths ($\lambda < 5\,\mu$m), i.e., channels VIS, IR1, IR2, and IR3, will be equipped with mercury cadmium telluride (MCT) detectors. MCT detectors are widely used in ground-based and space-based astronomy. Their expected performance has been tested over a wide range of wavelengths. The Teledyne H2RG MCT detectors are currently successfully operated on the optical test bench (Blank et al., 2012).

MCT detectors are widely used for near-infrared astronomy and their expected performance is well established. Removing the CdZnTe-substrate enables the extension of the cut-on wavelength down to 400 nm. The removal process has become a standard procedure and, without the CdZnTe-substrate, the quantum efficiency of MCT detectors reaches ~80%, comparable to state-of-the art CCD and CMOS detectors (Figure 5-4). For EChO it was, therefore, found that using MCT detectors at visible wavelengths provides little disadvantages compared to the commonly used CCD technology, but provides significant advantages in the commonality of the

detectors and electronics.

At mid-infrared wavelengths ($\lambda > 5\,\mu$m), Si:As impurity band conduction detectors were selected in the first baseline design for the channels IR4 and IR5 (e.g., Ressler et al., 2008). The Si:As detectors require an operating temperature of $\sim 7\,$K and, therefore, cannot be operated without cryogenic cooling. In addition, Si:As detectors are sensitive up to $28\,\mu$m, which requires that the instrument optics of IR4 and IR5 are actively cooled down to $\sim 15\,$K to suppress their thermal emission. Si:As detectors have a high readiness level (TRL 6-7) because a strong heritage and experience exists from the development of the *Mid InfraRed Instrument* (*MIRI*) for *JWST*. Extensive instrument test have been carried out for *MIRI*.

MCT detectors can, in principle, be used for all spectral channels covering the considered spectral range between 400 nm and $16\,\mu$m (Glauser, 2013). The advantage of using MCT detectors would be that many MCT detectors can be operated at a temperature as high as 55 K and would not require costly cryogenic cooling. Their cut-off at long wavelengths can be fine tuned between the NIR and $\sim 20\,\mu$m by adjusting the material composition of the detector. The steeply increasing dark current towards long wavelength, however, would not allow them to meet the current noise requirements at long wavelengths. More detailed discussions of the detector technologies can be found for MCT detectors on EChO in Blank et al. (2012) and for the Si:As detectors on JWST in Ressler et al. (2008).

5.1.4 Design Questions

The main unresolved questions for the design of the EChO's payload addressed in this work are the short wavelength cutoff and the mid-infrared capabilities. The short wavelength requirements directly affect the requirements on the reflectance and material of the optical surfaces of the telescope and instrument. Spectral coverage shorter than $\sim 550\,$nm, realistically, precludes the use of gold (Au) as the material for the optical surface due to its low reflectance at short wavelengths (Figure 5-6). The use of silver (Ag) or aluminum (Al), in turn, will lead to a measurable loss in reflectance and thus photon flux to the detectors at wavelengths larger than

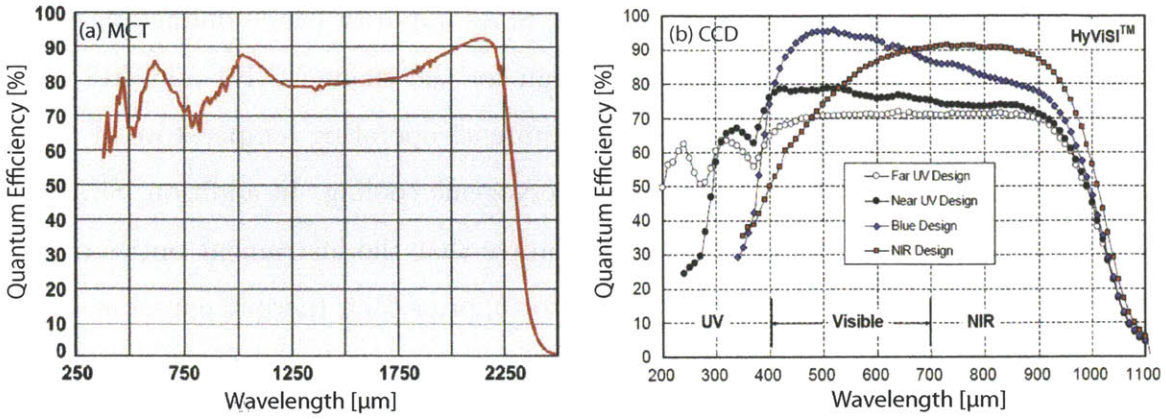

Figure 5-4: Quantum efficiency of MCT detectors (a) and CCD detectors (b) at visible and NIR wavelengths. The process of removing the CdZnTe-substrate commonly used by MCT detectors increases the quantum efficiency of MCT detectors at short wavelengths to values that are comparable to the quantum efficiency values achieved by state-of-the art CCD detectors. In this work, we assume a wavelength-independent quantum efficiency of 80% at visible and NIR wavelengths. Figures credit Teledyne.

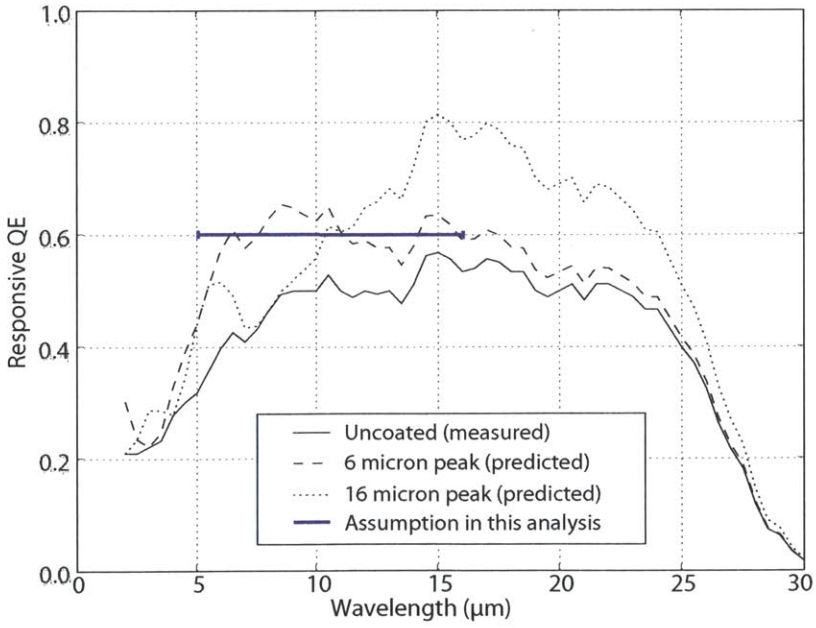

Figure 5-5: Quantum efficiency of Si:As at infrared wavelengths. In this work, we assume a wavelength-independent quantum efficiency of 65% between 5 and 16 μm (blue line). Figure adopted from Ressler et al. (2008).

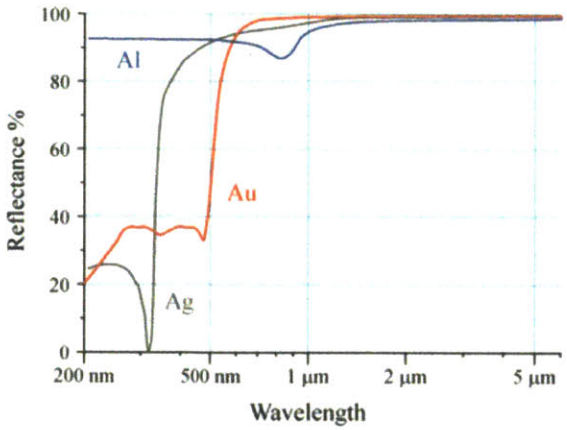

Figure 5-6: Reflectances of optical surface materials. Figure adopted from NIST.

$\sim$ 600 nm. The short wavelength cutoff is, therefore, a trade-off between additional spectral coverage and a loss in the throughput at near-infrared wavelengths.

The long wavelength requirements, on the order hand, directly affect whether cryogenic cooling is required for the science instrument. Spectral coverage beyond $\sim 10 - 11\,\mu$m will require the use of Si:As detectors and, therefore, will demand cryogenic cooling of the detector to ~ 7 K and cryogenic cooling of the instrument to ~ 15 K. Current estimates indicate that a cryogenic cooling system would increase the total mission costs by $\sim 20\%$. The question to be answered is whether the increase in the total mission costs by $\sim 20\%$ due to cryogenic cooling is justified or whether the funds that would be freed by a fully passively-cooled design could be used more efficiently for a different purpose in the mission design.

Four alternative design configurations with different spectral coverages, detector technologies, and optical surface materials are currently being considered for EChO's science instrument (Table 5.1). The configurations can be regarded as local optima in the design space given the restrictions introduced by different cooling technologies, optical surface materials, and numbers of spectral channels.

The baseline configuration represents the scientifically most capable configuration and covers the full spectra range between 400 nm and 16 μm. Wavelength shorter than 5 μm are observed with mercury cadmium telluride (MCT) detectors. For optimum performance, wavelengths longer than than 5 μm are observed with Si:As detectors

due to their low dark current. The Si:As detectors make cryogenic cooling necessary. The short wavelength cut-off at 400 nm requires the use of silver or aluminum as the material for the optical surfaces.

Configurations 2, 3 and 4 remove the requirement for cryogenic cooling by reducing the long wavelength coverage from 16 μm to 11 μm and replacing the Si:As detector in channels IR4 and IR5 by a single MCT detector that covers the range between 5 μm and 11 μm. MCT detectors with moderate dark current up to $\sim$ 11 μm are currently being developed by Teledyne and may be a good alternative to the Si:As detectors for wavelengths shorter than 11 μm.

Configurations 3 and 4 additionally enable the use of gold as the optical surface material by lowering the requirements on the short wavelength cut-off from 400 nm to 550 nm or 700 nm, respectively. Configuration 4 reduces the number of channels to 4 by removing the visible channel completely.

Other design parameters are fixed to the values described in the EChO Science Requirements Document and the EChO Mission Requirements Document. Limitations for the effective area of the primary mirror and telescope configuration is largely set by the launch vehicle and cost cap (Section 5.1.2). Requirements on sensitivity limits for the brightest and faintest target stars are mostly set by stellar population studies.

5.2 Design Evaluation Framework

5.2.1 Overview

Finding the spacecraft and mission design for EChO that delivers the most science output requires an integrated modeling approach that simultaneously considers the science output and engineering aspects of the space telescope design. The expected science output as a performance measure for EChO can, to the first order, be represented as the constraints on atmospheric parameters that EChO is expected to determine for a wide range of planets in the target planet population.

Parameter	Configuration 1 (Baseline)	Configuration 2	Configuration 3	Configuration 4
Wavelength Coverage	400 nm - 16 μm	400 nm - 11 μm	550 nm - 11 μm	700 nm - 11 μm
Number of Channels	6	5	5	4
Detector Technology	Vis 0.4 – 0.8 μm MCT IR1 0.7 – 1.5 μm MCT IR2 1.5 – 2.5 μm MCT IR3 2.5 – 5.0 μm MCT IR4 5.0 – 8.5 μm Si:As IR5 8.5 – 16 μm Si:As	Vis 0.4 – 0.8 μm MCT IR1 0.7 – 1.5 μm MCT IR2 1.5 – 2.5 μm MCT IR3 2.5 – 5.0 μm MCT IR4 5.0 – 11 μm MCT —	Vis 0.55 – 0.8 μm MCT IR1 0.7 – 1.5 μm MCT IR2 1.5 – 2.5 μm MCT IR3 2.5 – 5.0 μm MCT IR4 5.0 – 11 μm MCT —	— IR1 0.7 – 1.5 μm MCT IR2 1.5 – 2.5 μm MCT IR3 2.5 – 5.0 μm MCT IR4 5.0 – 11 μm MCT —
Spectral Resolving Power	300 ($\lambda \leq 5\,\mu$m) 30 ($\lambda > 5\,\mu$m)	300 ($\lambda \leq 5\,\mu$m) 30 ($\lambda > 5\,\mu$m)	300 ($\lambda \leq 5\,\mu$m) 30 ($\lambda > 5\,\mu$m)	300 ($\lambda \leq 5\,\mu$m) 30 ($\lambda > 5\,\mu$m)
Material of optical surfaces	Silver (Ag)	Silver (Ag)	Gold (Au)	Gold (Au)
Cooling	Cryogenic down to 7 K for IR4 and IR 5	Passive down to 45 – 55 K	Passive down to 45 – 55 K	Passive down to 45 – 55 K

Table 5.1: Alternative configurations for the EChO Science Instrument.

The integrated design evaluation combines scientific modeling of the astrophysical signal and engineering models of the EChO payload module to directly link the detector and instrument design parameters to the atmospheric constraints as an estimate of the scientific output (Figure 5-7). The inputs to the framework are the EChO design parameters, the target exoplanet and host star scenario, and the devoted number of transits. The output is a set of atmospheric constraints describing what we have learned about the target exoplanet given the simulated EChO observations.

Starting from the target planet scenario, the exoplanet atmosphere model described in Section 2.3 simulates a high-resolution transmission spectrum of the exoplanet atmosphere. Simultaneously, the spectral type, distance, and location of the host star scenario are used to derive the stellar flux density spectrum observed by EChO. The radiometric model we describe in (van Boekel, Benneke, et al., 2012) then computes synthetic observations of the exoplanet's transmission spectrum based on the model transmission spectrum of the exoplanet. The expected observational uncertainty in each wavelength bin is computed taking into account a set of instrument design parameters, the flux density spectrum of the observed star, the zodiacal background, the transit duration calculated from the planet's orbital parameters, and the number of stacked transits. Finally, the synthetic observations, including their expected observational uncertainties, are fed into the atmospheric retrieval method (Section 2) to determine which atmospheric constraints could be found if the chosen EChO configuration had observed the target object.

5.2.2 Radiometric Model

The radiometric model used to simulate the optical system and the science instrument of EChO is described in detail in our joint publication (van Boekel, Benneke, et al., 2012). The model consists of an instrument model to propagate the astrophysical signals on to the detector, a detector model to simulate the detector response, and a signal-to-noise model to compute the resulting spectrum and its observational uncertainty for a defined set of observations.

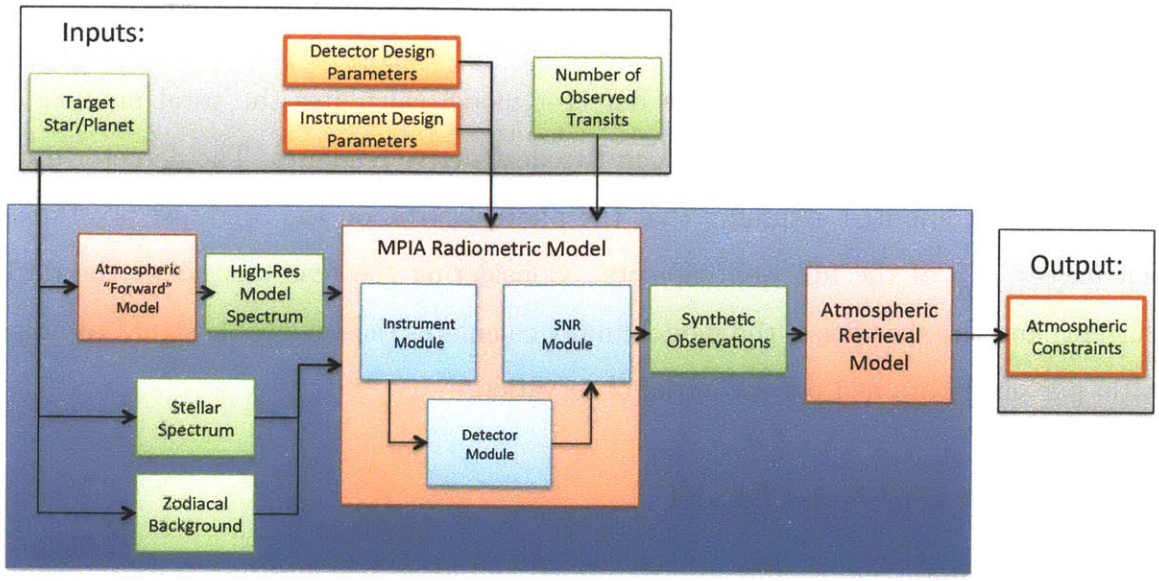

Figure 5-7: Design evaluation framework for assessment of EChO configurations. Implemented models are illustrated in light red. Modules within radiometric model are blue, and data and simulation results are illustrated by green boxes. The design inputs and atmospheric constraints are highlighted by a red contour.

5.2.2.1 Instrument Model

The objective of the instrument model is to calculate the rate at which photons hit each individual pixel of the detector. The inputs to the instrument models are specified as the stellar brightness, the stellar spectrum, and the planetary spectra. The model then considers the wavelength-dependent reflectance functions of the optical surfaces, the wavelength-dependent transmission and reflectance functions of the dichroic mirror, and the beam splitter throughput to determine the wavelength-dependent photon flux arriving at the individual spectroscopic cameras. The signal arriving at the spectroscopic camera is then convoluted in the spectral direction with the instrumental dispersion profile. In spatial direction, the light is spread using an estimated Gaussian point spread function. The outputs of the instrument model are the photon rates received by each individual pixel in photons per second.

5.2.2.2 Detector Model

From the photon rate received, the detector model calculates the total number of electrons collected in any pixel between two destructive readouts. The detector duty cycle is then computed assuming that the photoelectron on the brightest pixel does not exceed 2/3 of the full well capacity. Considering the read-out noise, the dark current, and the shot noise, the model finally calculates the achievable signal-to-noise ratio per pixel obtained per second of observation.

5.2.2.3 Signal-to-Noise Model

The signal-to-noise model combines the signal and noise contributions from all pixels in a given resolution element. The time to build up the signal for a transit observation is then calculated from the orbital parameters of the planet and the stellar radius. Finally, the model takes into account that the transmission spectrum is a difference spectrum between the measured in-transit flux and the measured out-of-transit flux. Accounting for the finite duration baseline measurement to obtain the out-of-transit flux, the signal-to-noise ration (SNR) of the difference spectrum is obtained by multiplying the SNR of the in-transit spectrum by $(1 + 1/f)^{-1/2}$, where f is the ratio between the observational time for the baseline measurement and the eclipse duration. Finally, the total SNR of the each spectral data point is calculated accounting for the number of stacked transit observations, assuming that the errors in the individual transits are uncorrelated.

5.2.3 Synthetic EChO Observations of Representative Planet Scenarios

EChO will observe wide variety of transiting exoplanets ranging from super-Earth exoplanets to giant planets. To evaluate EChO's overall capability to characterize the planets, model spectra were generated for four planet scenarios (2 giant planets and 2 super-Earths) that are representative of the expected planet population accessible to EChO (Figure 5-8). For each of the four planet scenarios, four simulated sets of

EChO observations are generated for the four different configurations of the science instrument (see Figures 5-9 for a haze-free giant planet scenario). The capabilities of the individual configurations of EChO in studying the planetary scenarios are then assessed and compared by analyzing the simulated data sets obtainable from the different EChO configurations using the Bayesian retrieval method. The computational complexity of performing four independent retrieval analyses limits the total number of planetary scenarios considered in this study to no more than $\sim 3-5$.

A wide range of atmospheres of Neptune-sized to Jupiter-sized planets can be represented by two atmospheric scenarios. The first scenario is a solar composition atmosphere at an equilibrium temperature, of 1000 K. The second scenario is a carbon-rich planet (C/O=1) at an equilibrium temperature of 300 K. The motivation for the difference in equilibrium temperatures, which are essentially measures of the stellar irradiation of the planet, is to probe two different chemical regimes that strongly affect the spectrum of the planet. The infrared spectra of carbon-rich giant exoplanets at $T_{eq} = 300\,\mathrm{K}$ are dominated by the absorption of methane and carbon-monoxide. Giant exoplanets with a solar composition at $\sim 1000\,\mathrm{K}$, on the other hand, are dominated by water absorption at infrared wavelengths and, more importantly, the Rayleigh signatures at visible wavelengths are largely masked by the strong resonance absorption lines of sodium and potassium, which become gaseous above $\sim 800-900\,\mathrm{K}$.

The capability of EChO to study super-Earth exoplanets that are dominated by gases other than hydrogen is assessed by analyzing synthetic observations of two super-Earth scenarios. The atmosphere of the first scenario is dominated by nitrogen dominated (98% N_2+ 1% H_2O + 1% CO_2) and can be regarded as representative of atmospheres with a spectrally inactive gas as the dominant species. The second scenario is a water vapor world (95% H_2O + 5% CO_2) and represents super-Earth atmospheres that are dominated by a strong absorber such H_2O, CO_2, or CH_4. The equilibrium temperatures of the super-Earth scenarios planet are chosen to be 500 K, which is representative of the EChO prime target for intense super-Earth studies.

The host stars for the two giant planet scenarios are sun-like stars at 25 parsecs

distance, representing a median star in the EChO planet population (Tinetti et al., 2012). The results derived for sun-like host stars at 25 parsec are representative of a large range of stellar types and distances because similar results can be achieved for other host stars if the number of transit observations is increased or decreased to obtain the same signal-to-noise levels for observational data points. Super-Earth exoplanets that are dominated by gases other than hydrogen are considered to orbit K5 stars at only 15 parsecs. The motivation for this selection is that the study of super-Earths will be limited to several prime targets that orbit smaller stars and are at a shorter distance from Earth. The planet occurrence reported by Howard et al. (2012) suggests that a transit survey mission like TESS will provide many of these prime target by EChO's launch in 2022.

Most of the results presented in this chapter are for cloud-free atmospheric scenarios. The conceptual findings are similar for cloudy or haze atmospheres, and, where necessary, comments are provided in the results to explain how the findings would change of clouds or hazes are present in the atmospheres.

5.3 Results

This section addresses the design questions posed in Section 5.1.4 by analyzing and comparing the capabilities of the four different science instrument configurations. The first part demonstrates that EChO's short wavelength coverage, ideally down to 400 nm, is essential in identifying the composition and metallicity of a wide range of EChO's target planet population. Optical surface materials with high reflectivity at short wavelengths are, therefore, key to meeting the science objectives. The second part identifies that the Si:As detector with lower dark currents and spectral coverage up to 16 μm leads to measurable improvements in the atmospheric constraints derived from a given set of transit observations. The same constraints, however, can be recovered by increasing the number of transit observations for a given target by $\lesssim$ 10%.

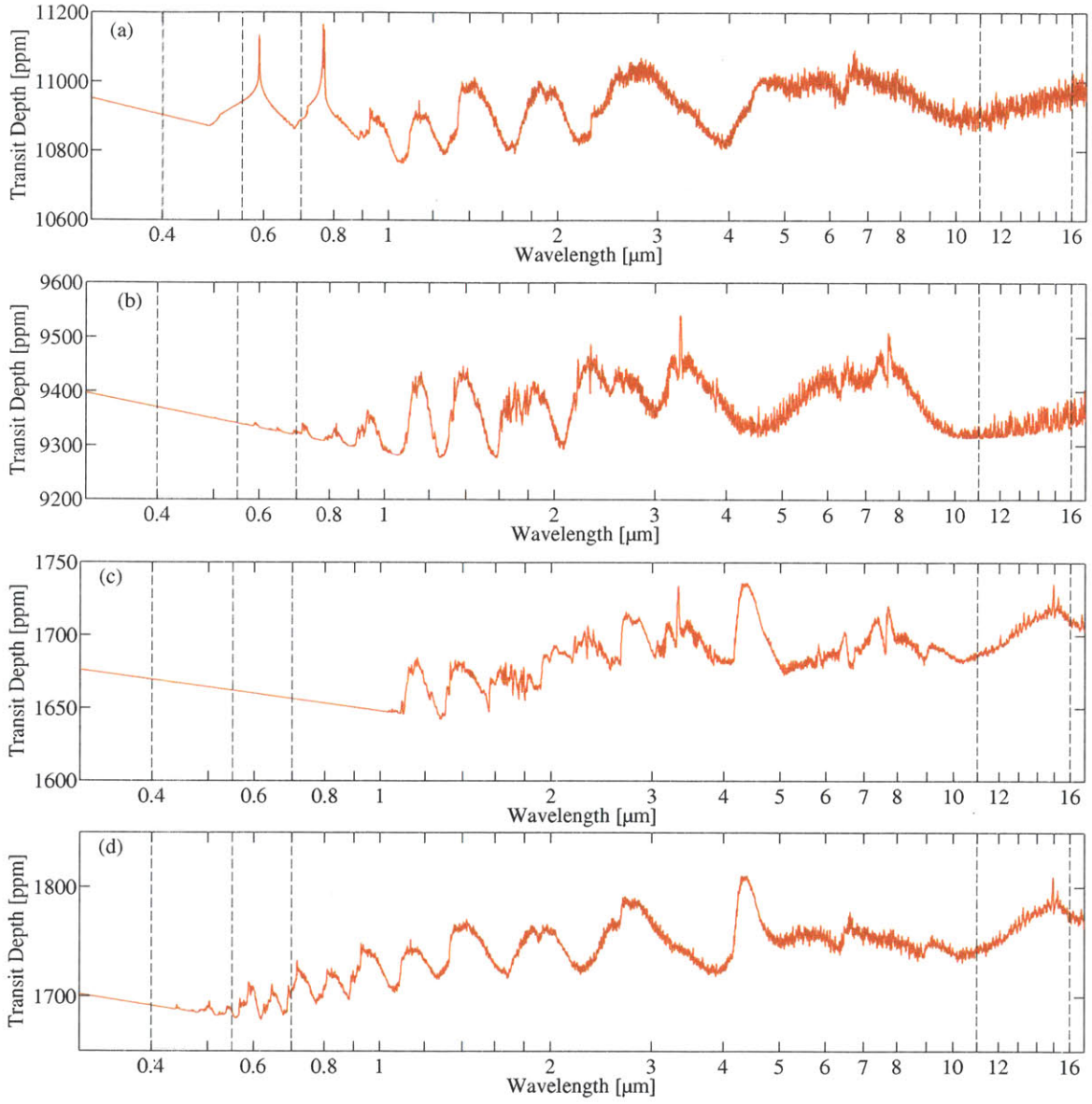

Figure 5-8: Model spectra of exoplanet scenarios used to assess EChO's capability in characterizing the composition of exoplanet atmospheres. Model spectra are shown for hot Jupiter with solar composition (a), temperate Jupiter with C/O=1 (b), a super-Earth with N_2-dominated atmosphere and super-Earth dominated by H_2O and CO_2. The short-wavelength cut-offs and long-wavelength cut-on of different EChO configurations are indicated by dashed, vertical lines. Note that only configuration with a short-wavelength cutoff at 400 nm capture the Rayleigh slope for all four scenarios.

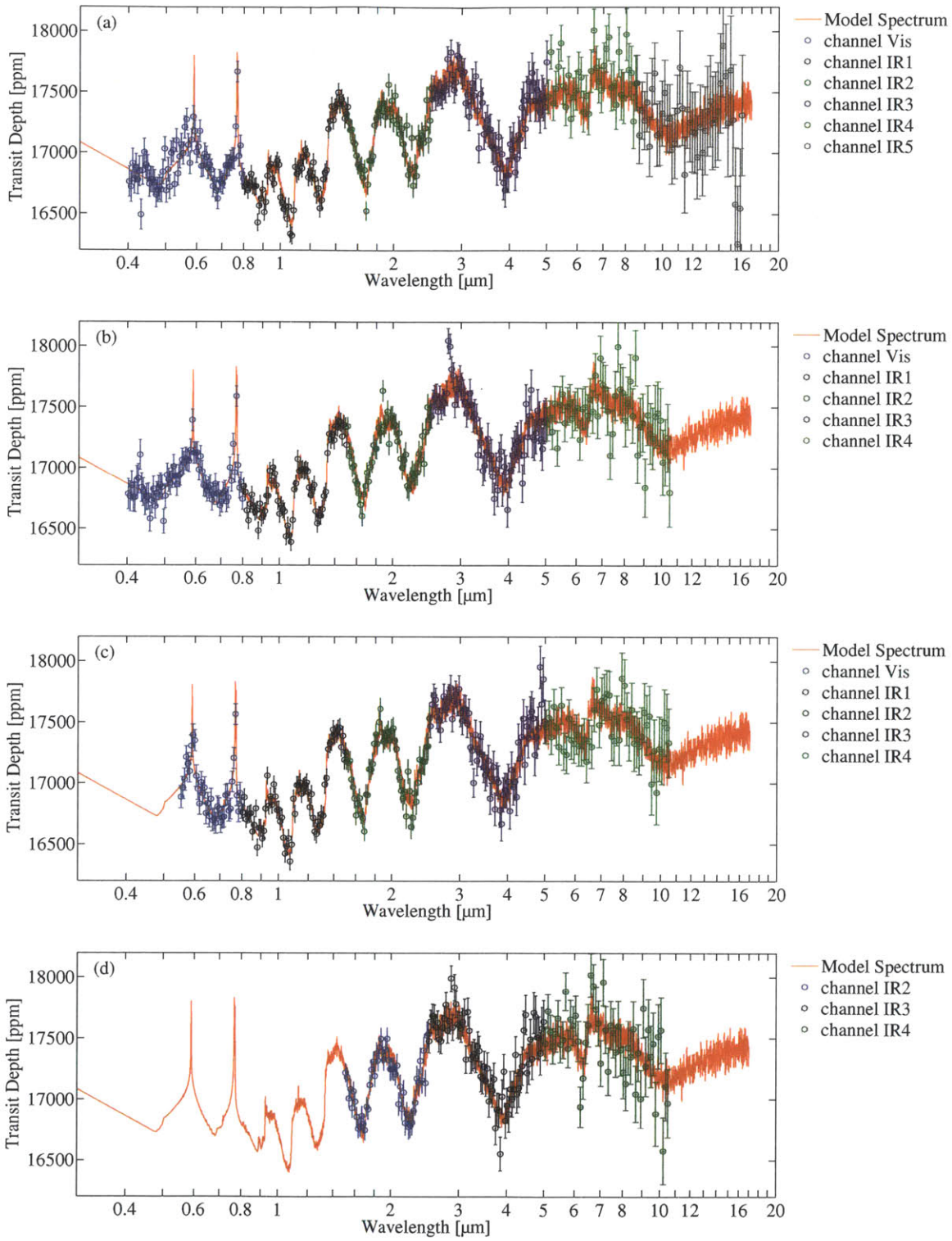

Figure 5-9: Simulated observations of a hot Jupiter with solar composition for the four different EChO instrument configurations. The model transmission spectrum (red) is identical the one in panel (a) of Figure 5-8. Synthetic observation and their uncertainties of the different instrument channels are indicated by colored circles and vertical error bars.

5.3.1 Importance of EChO's Short Wavelength Coverage

The baseline configuration covering the full spectral range between 400 nm and 16 μm captures all spectral "observables" identified in Section 3.2 to uniquely constrain the molecular composition of cloud-free super-Earths and giant planet atmospheres (Figure 5-10). A unique characterization is possible because the EChO measurements would cover the features of all relevant molecular absorbers at infrared wavelengths as well as the Rayleigh scattering at short wavelengths.

Configurations 3 and 4 with short wavelength cutoffs of 550 nm or 700 nm, on the other hand, would not be able to provide unique constraints for a some of the scenarios considered in this study. Neither configuration 3 or 4 would be able to probe the Rayleigh scattering signature for giant planets above $T \sim 900\,\mathrm{K}$ (Giant Planet Scenario 1) due to the strong opacities of gaseous Na and K at wavelengths greater than 500 nm (Figure to be added). As a result, only the relative abundances of the molecular absorbers would be constrained, while the absolute mole fractions of the gases in the atmospheres would remain largely unconstrained.

The lack of short wavelength observations would prevent scientists from identifying the metallicity of warm and hot giant planets using transmission spectroscopy (Figure 5-11(b)). The carbon-to-oxygen ratio would still be retrievable because all relevant carbon- or oxygen-bearing species show absorption features such that the relative abundance of carbon and oxygen atoms in the atmospheric gas can be identified without knowing the abundance of hydrogen (Figure 5-11(a)).

Configuration 4 with the short wavelength cutoff at 700 nm will, in addition, lack the ability to constrain the absolute mole fractions for many super-Earth scenarios with water absorption (Figure 5-12). Water absorption effectively blocks the Rayleigh scattering signature at all wavelengths greater than 700 nm. A comparison of panels (a),(c), and (d) in Figures 5-12 demonstrates that the benefits of observing the spectral range between 400 nm and 550 nm (or 700 nm respectively) strongly outweighs the loss in the throughput for red and far red wavelengths due to silver's lower reflectance. Even for a conservative assumption of 96% reflectance of silver and

a total count of 4 optical surfaces between the primary mirror and the first dichroic mirror, the throughput would drop by no more than 15% compared to the throughput for gold-coated surfaces, corresponding to a maximum increase in observational error bars of 8% at 600 nm.

The exact quantitative constraints of the atmospheric compositions will depend on the exact planet/star scenario and on how much observational time is assigned to the specific targets. It will thus depend on the detailed time scheduling, which is beyond the scope of this analysis. It can be stated, however, that a single transit observation would generally be sufficient to identify the main molecular gases and get a first estimate of the metallicity and carbon-to-oxygen ratio of the atmospheric gas for all cloud-free giant planets within 25 parsecs orbiting a quite G-star (or smaller). The dominant species in the atmospheres of several prime super-Earth targets would be identifiable over the lifetime of EChO if they orbit a nearby M-dwarfs or late K-dwarf. Over the proposed mission lifetime, the baseline configuration of EChO would therefore enable us to understand the nature and main characteristics of tens of hydrogen-rich giant planets as well as several prime super-Earth exoplanets.

Up to this point, I have presented results for cloud-free atmospheric scenarios. Qualitatively, the importance of short wavelength observations remains unchanged as long as the haze or cloud particles are large enough such that their opacity does not scale as λ^{-4}, thus their effect on the planetary spectrum is different from the effect of molecular Rayleigh scattering. As for cloud-free atmospheres, a unique characterization will require EChO to cover the signature of molecular Rayleigh scattering at short wavelengths. If the haze or cloud particles are small, however, all four EChO configurations considered will be limited to constrain the relative abundances of molecular species because the necessary information to constrain the absolute mole fractions and metallicities of hydrogen-rich planets is simply not available in the astrophysical signal.

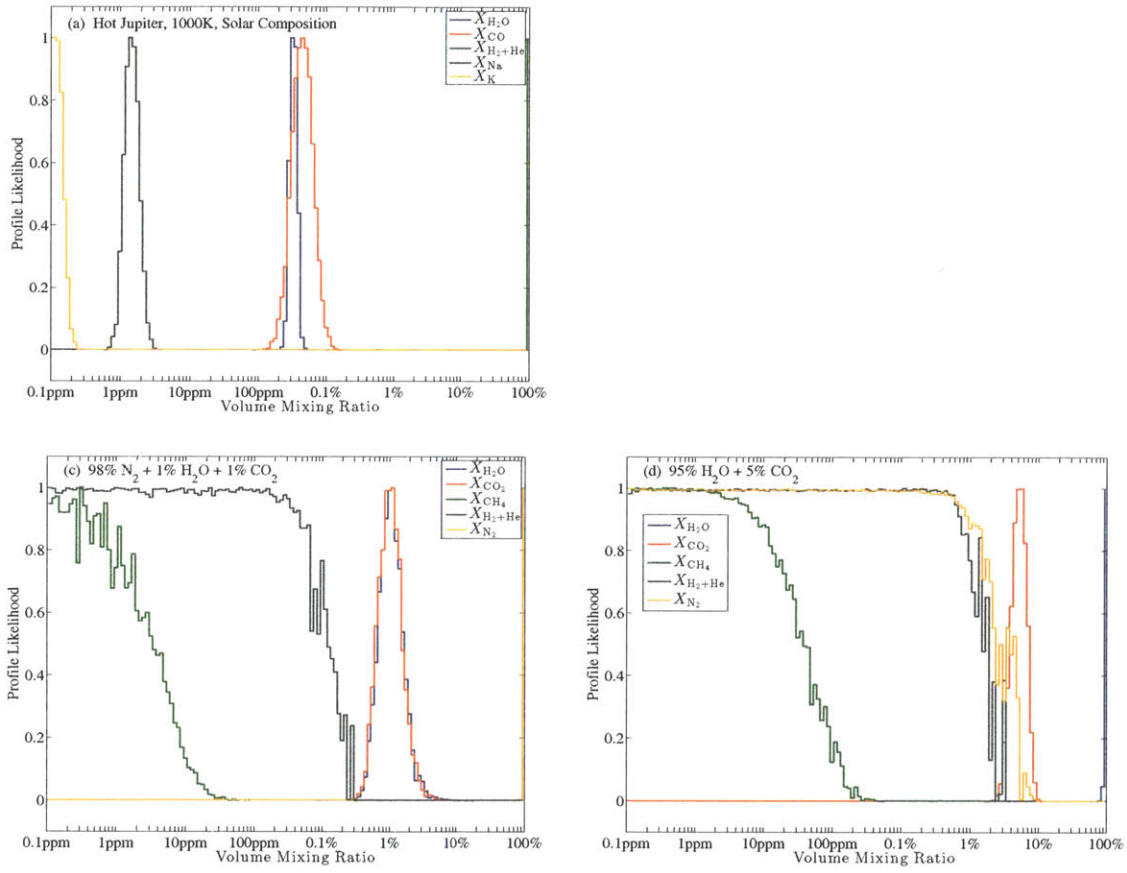

Figure 5-10: Unique constraints on absorber abundances from synthetic observation with EChO's baseline configuration. The unique constraints on the volume mixing ratios of the absorbing gases manifest as well-constrained, single-modal distributions. The spectral-inactive gases may have no lower bound if the abundance of the low such that the presence of the gas has not effect on the spectrum. The details of the observational scenario are discussed in Section 5.2.3.

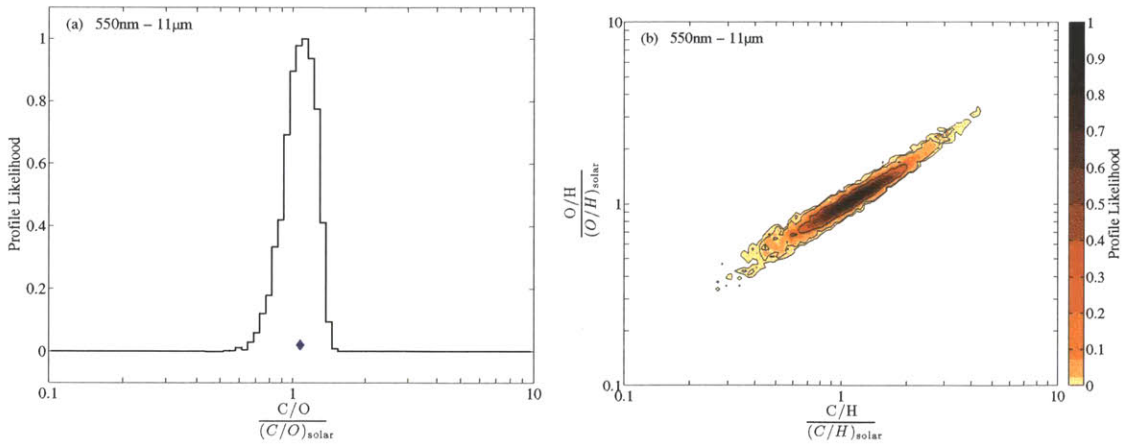

Figure 5-11: Confidence regions for (a) carbon-to-oxygen ratio and (b) metallicity derived from synthetic observations of solar composition atmosphere with EChO configuration 3. The relative abundance ratios between H_2O and CO can be constrained from the infrared observation alone, leading to good constraints on the carbon-to-oxygen ratio. The carbon-to-hydrogen ratio and oxygen-to-hydrogen, on the other hand, are poorly constraint due to the lack of short-wavelength absorption to constrain the absolute abundances of H_2O and CO. The details of the observational scenario are discussed in Section 5.2.3.

5.3.2 Long Wavelength Coverage and IR Detector Technology

Two design options for the coverage of wavelengths larger than $5\,\mu$m are the Si:As detectors (baseline configuration) and MCT detectors (configuration 2) (Table 5.1). The performance of the baseline configurations with Si:As detectors and cryogenic cooling is superior because Si:As detectors provide a lower dark current and a larger wavelength coverage (up to $16\,\mu$m compared to $11\,\mu$m for configuration 2). The results presented in this subsection indicate, however, that the smaller dark current and increased spectral coverage leads only to moderate improvements in EChO's capability to characterize exoplanet atmospheres. For a given target exoplanet, the same science can be done without cryogenic cooling by assigning a slightly larger observational time. The total costs saved by not using Si:As detectors and a cryogenic cooling system may, therefore, be used more efficiently by using MCT detectors and increasing the mission life time to compensate for EChO's slightly smaller science output per observational time.

In contrast to the short wavelength spectrum discussed in Section 5.3.1, the spec-

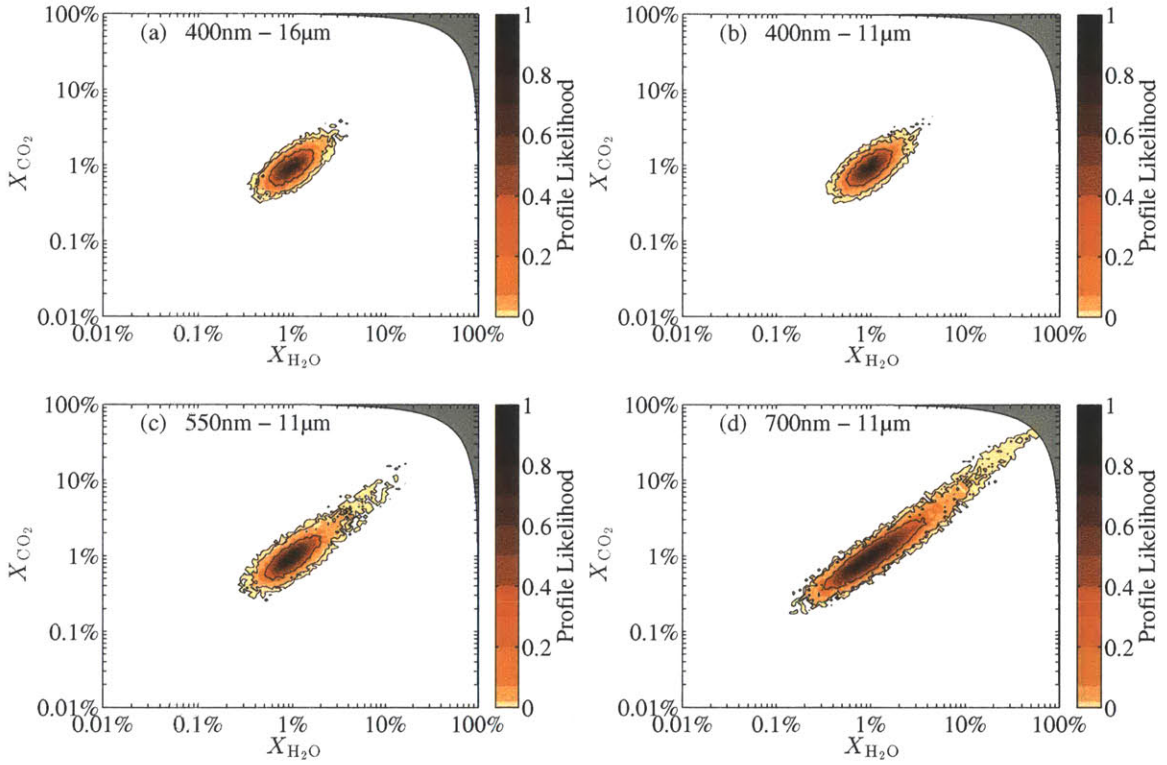

Figure 5-12: Comparison of the ability of four EChO configurations to constrain the volume mixing ratios of H_2O and CO_2. Panel (a) to (d) show the confidence regions on the volume mixing ratios of H_2O and CO_2. For configurations 1 and 2, volume mixing ratios are well-constrained around the expected value of 1% used to simulate the synthetic observations. Reducing the spectral coverage at mid-infrared wavelength from 16 μm to 11 μm leads to insignificant degradation of the atmospheric constraints. For configuration 3 with a short wavelength cutoff at 550 nm, the mixing ratios of H_2O and CO_2 become strongly correlated (panel c). The 3σ confidence region extends to $> 10\%$. For configuration 4 the correlation continues worsen (panel d). For short-wavelength cutoff at 700 nm, it becomes impossible to distinguish between the original N_2-rich scenario and an atmospheric dominated by H_2O and CO_2. The details of the observational scenario are discussed in Section 5.2.3.

tral range between $11 - 16\,\mu$m does not provide any unique information in the transmission spectrum that would not be available from observations between 700 nm and $11\,\mu$m. An analysis of relevant spectral features shows that there are no spectral features of a molecular absorber that do not also have features at wavelengths shorter than $11\,\mu$m.

Covering the spectral range between $11 - 16\,\mu$m can be regarded as merely providing independent measurements of the same spectral observables that are also observed between 700 nm and $11\,\mu$m. The benefit of simultaneously obtaining the independent measurements between 11 and $16\,\mu$m is that minimally tighter constraints can be retrieved on the abundances of a subset of molecular species for a given transit observation (Figure 5-12). The wider spectral coverage thus effectively increases EChO's science output per unit mission time. The improvement is, however, minuscules and limited to the three molecular species CO_2,H_2O, and O_3 with features between 11 and $16\,\mu$m.

The lower dark current of Si:As detectors, which is the second potential benefit of using Si:As detectors, provides only small improvements in EChO's capabilities. The observations of prime targets around nearby bright stars (brighter than K magnitude 8) are dominated by shot noise and dark current has negligible effects on the error bars for both Si:As and MCT detectors. The difference between Si:As and MCT detectors will therefore be limited to the faintest stars in the target population (K magnitudes 9-10) and, even then, only the spectral range above $5\,\mu$m will be affected.

5.4 Discussions

5.4.1 Wavelengths of Molecular Vibrations

One of the main results of Section 5.3 is that mid-IR coverage beyond $11\,\mu$m provides only redundant information on the planetary atmospheres and therefore is not required for the success of EChO. The underlying reason is that all relevant molecular species display vibrational modes that result in absorption bands at wavelengths

below $\sim 10\,\mu$m. The occurrence of absorption bands below $\sim 10\,\mu$m is a direct result of the molecular energy levels and therefore true for all planetary atmospheres in which stable molecules can form ($T \lesssim 2000 - 3000\,\mathrm{K}$). The purpose of this section is to explain, from first principles, why molecular bands corresponding to vibrational transition of virtually all molecules occur at wavelengths below $\sim 10\,\mu$m.

Molecular lines correspond to transitions between discretized molecular energy states. The difference to atomic lines is that the energy states of molecules can change not only as a result of electronic transitions, but also as a result of changes in the molecule's vibrational or rotational states. Molecular spectra are more complex than atomic spectra because even simple linearly symmetric molecules such as $CO_2$and N_2O can undergo three distinct vibrational modes: ν_1 for symmetric stretching, ν_2 for bending motion, and ν_3 antisymmetric stretching. In addition, these transitions between vibrational states are generally accompanied by simultaneous transitions in the rotational state, leading to a forest of individual molecules in each of the vibrational bands.

The energy levels of the molecular vibrations can be derived, to first order, using parabolic approximations to the molecular potential curves. The energy levels of symmetric stretching of the diatomic molecules, for example, can be derived using the parabolic approximation

$$V(x) = \frac{1}{2}kx^2 \tag{5.1}$$

to the molecular potential energy as a function of internuclear separation near the of the bottom of potential energy well. Here, k is the force constant of the molecular bond, and $x = R - R_e$ is the deviation of the internuclear distance R_e for which potential energy V is minimum. The force constant k for the harmonic oscillator approximation can then be derived from the true molecular potential energy curve using

$$k \approx \left(\frac{\mathrm{d}^2V}{\mathrm{dx}^2}\right)_{x=0}. \tag{5.2}$$

The Schrödinger equation for the relative motion of the two atomic masses m_1 and m_2 in the diatomic molecule is then

$$-\frac{\hbar^2}{2m_{red}}\frac{\mathrm{d}^2\Psi}{\mathrm{d}x^2}+\frac{1}{2}kx^2\Psi=E\Psi, \tag{5.3}$$

where the reduced mass is

$$m_{red}=\frac{m_1m_2}{m_1+m_2}. \tag{5.4}$$

harmonic oscillators as classical analogs to the true quantum mechanical natures of the molecular vibrations. In this classic mechanics model, the simplest vibrational mode, i.e. the symmetric stretching of the molecule, can be described as an harmonic oscillation of the internuclear separation around minimum of the molecular potential energy curve (Figure ___). Near the bottom of the potential energy well, the potential energy curve can be approximated as parabolic potential energy curve

$$V=\frac{1}{2}kx^2 \tag{5.5}$$

where k is the force constant of the bond, and $x=R-R_e$ is the deviation of the internuclear distance from the bottom of the potential energy curve. Equation (5.3) is the same as Schrödinger equation for a particle undergoing harmonic motion, thus the vibrational energy levels are

$$E_\nu=\left(\nu+\frac{1}{2}\right)\hbar\omega, \tag{5.6}$$

where the frequency

$$\omega=\sqrt{\frac{k}{m_{red}}} \tag{5.7}$$

and the vibrational quantum numberν is an integer $\nu=0,\ 1,\ 2,\ldots$

Using typical values for the force constant k and the atomic masses m_1 and m_2, it can be shown that the difference in the energies of vibrational states corresponds to the energy of photons in the near-infrared range. For example, for a HCl molecule,

the force constant is $516\,\mathrm{Nm}^{-1}$ and the reduced mass $m_{red} = 1.63 \cdot 10^{-27}\mathrm{kg}$, resulting in the frequency $\omega = 5.63 \cdot 10^{14}\mathrm{s}^{-1}$ according to Equation (5.7). The ν_1-band (symmetric stretching) of the HCl molecule is therefore at $\lambda \approx 3.35\,\mu\mathrm{m}$. Table lists the computed or experimentally determined wavelengths of the vibrational modes for the most relevant molecular species, taken from the HITRAN database (Rothman et al., 2009). All molecular species except the trace gases ClO and CCl_4 display vibrational bands at $\lambda < 11\,\mu\mathrm{m}$. ClO and CCl_4 are trace gases below the parts per billion level in Earth's atmosphere. It is unlikely that ClO and CCl_4 would be available at levels detectable for a transiting exoplanet.

5.4.2 Aperture Size

The objective in setting the aperture size for EChO is to maximize the collection area to collect as many photons as possible while meeting the stringent constraints on total mission costs and the spacecraft mass and size set by the Soyuz launch vehicle. Throughout this study the effective collection area of EChO was set to 1.13 m^2 because initial design studies revealed that an effective primary mirror diameter of $\sim$1.2 m can plausibly be incorporated in an ESA M-class mission. A detailed study of the effect of the aperture size on the scientific output is not part of this study, however, the design evaluation framework presented in Section 5.2 can also be employed to study the scientific output as a function of the aperture size.

One question one may be interested to answer addresses the minimum aperture size required for EChO to achieve a planet characterization mission worth pursuing. If EChO needed to be scaled down, for example, the question arises at which aperture size would one need to decide that the mission is not worth pursuing? To answer this question, one needs to specify how many super-Earths, Neptunes, and Jupiters need to be studied, and what the stellar spectral class and apparent magnitude of the host stars are. One would then check for each target planet individually, how many transit are observable over the course of the mission lifetime, and whether the required

Molecule	Wavelength [μm]							
	ν_1	ν_2	ν_3	ν_4	ν_5	ν_6	ν_7	ν_8
Water (H_2O)	2.73	6.27	2.66					
Carbon dioxide (CO_2)	7.20	14.99	4.26					
Ozone (O_3)	9.07	14.27	9.60					
Nitrous oxide (N_2O)	4.50	16.98	7.78					
Carbon monoxide (CO)	4.67							
Methane (CH_4)	3.43	6.52	3.31	7.66				
Oxygen (O_2)	6.43							
Nitric oxide (NO)	5.33							
Sulfur dioxide (SO_2)	8.68	19.31	7.34					
Nitrogen dioxide (NO_2)	7.58	13.33	6.18					
Ammonia (NH_3)	3.00	10.53	2.90	6.15				
Nitric acid (HNO_3)	2.82	5.85	7.54	7.67	11.38	15.46	17.24	13.11
Hydroxyl radical (OH)	2.80							
Hydrogen fluoride (HF)	2.52							
Hydrogen chloride (HCl)	3.47							
Hydrogen bromide (HBr)	3.91							
Hydrogen iodide (HI)	4.48							
Ethane (C_2H_62)	3.39	7.20	10.05	34.60	3.45	7.25	3.37	6.81
Ethylene (C_2H_4)	3.30	6.16	7.45	9.78	3.22	8.09	10.54	10.6
Chlorine oxide (ClO)	11.31							
Carbonyl sulfide (OCS)	11.64	19.23	4.85					
Acetylene (C_2H_2)	2.96	5.07	3.04	16.34	13.72			
Carbon tetrachloride (CCl_4)	21.55	46.08	12.52	31.65				
Carbonyl fluoride (COF_22)	5.14	10.38	17.18	8.05	16.16	12.92		
Chlorine nitrate ($ClONO_2$)	5.76	7.73	12.36	12.82	17.76	22.99	38.17	14.06
Formaldehyde (H_2CO)	3.59	5.73	6.67	3.52	8.01	8.57		
Formic acid (HCOOH)	2.80	3.40	5.65	7.21	8.14	9.04	16.00	9.68
Hydrogen cyanide (HCN)	3.02	14.03	4.77					
Hydrogen peroxide (H_2O_2)	2.78	7.16	11.55	38.61	2.81	8.09		
Hydrogen sulfide (H_2S)	3.82	8.45	3.81					
Hydroperoxy radical (HO_2)	2.91	7.18	9.11					
Hypobromous acid (HOBr)	2.77	8.6	16.13					
Hypochlorous acid (HOCl)	2.77	8.07	13.81					
Methanol (CH_3OH)	2.72	3.33	3.52	6.77	6.88	7.46	9.31	9.68
Methyl chloride (CH_3Cl)	3.40	7.38	13.66	3.29	6.89	9.83		
Methyl cyanide (CH_3CN)	3.39	4.41	7.22	10.87	3.32	6.91	9.61	27.62
Nitrogen oxide cation (NO+)	4.27							
Phosphine (PH_3)	4.31	10.08	4.30	8.94				
Sulfur hexafluoride (SF_6)	12.90	15.55	10.55	16.26	19.08	28.9		

Table 5.2: Vibrational modes of molecular species commonly found in planetary atmospheres. Values derived from Rothman et al. (2009). All molecular species (except for the trace gases ClO and CCl_4) display vibrational bands at $\lambda < 11\,\mu$m.

atmospheric constraints can be achieved assuming that all observable transits of the target planet are observed. For orbital periods of tens or hundreds of days, it is conceivable that a small telescope is not able to collect enough signal to achieve the desired precision, even if all transits were observed over the mission lifetime. The second criteria one would need to examine is whether the desired number of target planets can be studied. While it may be possible to achieve the desired precision for each planet individually, it may not be possible to observe a sufficient number of transits for the a larger number of desired planets. To study

A simple scaling can be provided for photon noise limited observations, as expected for bright targets and sufficiently large apertures. In the photon-noise limit, the number transits $N_{\rm req}$ required to achieve a desired precision scales as

$$N_{\rm req} = \left(\frac{R_1}{R_{1\rm ref}}\right)^2 N_{\rm ref}, \tag{5.8}$$

where R_1 and $R_{1,\rm eff}$ are the effective diameter of the primary mirror in the design and the reference design and $N_{\rm ref}$ is the number of transits required by the reference design. A reduction in aperture diameter by 30%, for example, would require the observations of at least twice as many transits to achieve the same goal, effectively reducing the efficiency of the telescope in half. If the telescope diameter is sufficiently small or faint target are observed, however, noises sources other than photon noise, such as dark current and thermal emission from the telescope and instrument, become dominant and need to be considered in detail.

5.5 Summary and Recommendations

In this chapter, I have presented an integrated framework to assess the science output of four different configuration for EChO science instrument. The framework is novel in that it simultaneously models the astrophysical signal and the optical system and detector technology to evaluate the expected science output of EChO.

The main findings of the study are that optical surface materials, such as silver, with high reflectivity at short wavelengths (down to 400 nm) are crucial to constrain

the molecular composition, metallicity, and elemental abundances of extrasolar planets. Failure to capture the Rayleigh scattering slope at short wavelengths would results in strong degeneracies between the abundances of different gases in the atmosphere.

The extra costs to use Si:As detectors and cryogenic cooling to capture wavelength beyond $\sim 11\,\mu$m, however, is not required. If Teledyne can indeed deliver MCT detectors with a cut-on wavelength of $10-11\,\mu$m and dark current rate of 10-100 $e^{-}/px/s$, I recommend reducing the requirements on the wavelength coverage to $10-11\,\mu$m.

The 20% reduction in mission costs due to the removal of a cryogenic cooling system could be used well to increase the mission time to acquire more signal for prime targets. Even an increase of only 10% in the observational time assigned to a specific target planet will lead to larger improvement in atmospheric constraints than is provided by capturing the mid-infrared range between 11 and16 μm, for all four planetary scenarios studied in this work.

The added advantage of the long-wavelength MCT detectors is that they may be operated far beyond the design mission lifetime. Cryogenically cooled Si:As detectors would need to stop science operation once the cryogen is consumed.

Chapter 6

Conclusions

6.1 Thesis Contribution

This thesis is devoted to establishing a Bayesian atmospheric retrieval framework to infer the atmospheric compositions and properties of clouds and hazes from spectral observations of exoplanets. Given an observational data set, the retrieval framework first identifies which molecular gases and types of aerosols are present in the atmosphere and then constrains their abundances and properties. By not employing any assumptions on the elemental composition of the planet or the chemical and dynamical processes in the atmosphere, the results provided by the retrieval framework remain independent of our preconceived ideas of planet formation and evolution.

In this thesis work, I apply the atmospheric retrieval framework to answer the fundamental questions regarding the uniqueness and information content of atmospheric spectra (Chapter 3), how to characterize super-Earth exoplanets (Chapter 4), and which designs of dedicated space telescopes are most efficient in characterizing the atmospheres of transiting planets (Chapter 5).

Chapter 3 demonstrates that the information provided by nature in the form of the transmission spectrum is sufficient to *uniquely* constrain the mixing ratios of the absorbing gases and up to two spectrally inactive gases in the optically-thin part of exoplanet atmospheres. I establish a comprehensive picture of which details in transmission spectra are essential for the unique characterization. In particular, I show

that a *unique* constraint of the mixing ratios of the gases is possible if the observations are sufficient to quantify the broadband transit depths in at least one absorption feature for each absorber and provide the slope and strength of the molecular Rayleigh scattering signature. The surface pressure or cloud-top pressure can be quantified if a surface or cloud deck is present at low optical depth.

Chapter 4 presents the first atmospheric retrieval study for a super-Earth exoplanet — the exoplanet GJ 1214b. I conclude that the currently available observations are insufficient to identify the nature of the planet's atmosphere. I demonstrate, however, that an observational distinction between hydrogen-rich sub-Neptunes and water worlds can be achieved efficiently by observing near-infrared absorption features, such as water features, at moderate resolution ($R \sim 50 \ldots 100$). In a numerical study, I demonstrate that a reduction of the observational uncertainties in the published *HST WFC3* and *VLT* transit observations by a factor of 2 to 3 would be sufficient to detect a clear water-rich atmosphere on GJ 1214b with high significance. Large observational programs of ten or more transits may therefore be capable of uniquely distinguishing between a water-rich and cloudy hydrogen-rich atmosphere.

Chapter 5 addresses the question of how to design the science instrument for a space telescope dedicated to the characterization of exoplanetary atmospheres. I establish an integrated design evaluation framework that simultaneously models the astrophysical signal and the EChO payload module to evaluate the expected science output of EChO as a function of the detector and instrument design parameters. I demonstrate that optical surface materials with high reflectivity at short wavelengths (down to 400 nm) are crucial to constrain the molecular composition, metallicity, and elemental abundances of extrasolar planets. The extra costs of cryogenic cooling to enable transit observations beyond $\sim 11\,\mu$m, however, appear not to be justifiable given the limited additional information provided by this wavelength range.

Today, the observational characterization of exoplanet atmospheres is still in its infancy and it is believed that the retrieval framework developed in this thesis will play a critical role in future characterizations of worlds outside our Solar System.

6.2 Outlook

Over the last 3½ years that this thesis work was performed, the field of exoplanets has evolved tremendously. The first transiting super-Earth exoplanet, GJ 1214b, was announced only 22 days before the beginning my doctoral research. Today we know from the *Kepler* mission that the galaxy is teeming with super-Earths. Tens of confirmed super-Earths and hundreds of super-Earths waiting for confirmation suggest that super-Earths are the ubiquitous in the galaxy.

Meanwhile, astronomers around the world are pointing the most powerful telescopes at favorable super-Earth targets to study their atmospheres. Still, despite the tremendous success in detecting super-Earths, the nature of super-Earths remains a mystery. Are they scaled up versions of the terrestrial planets in the inner Solar System, small versions of the giant planets in the outer Solar System, or a completely new type of planet, potentially rich in water vapor? Are they capable of supporting life?

Eventually, we will need to find out what the nature of these planets actually is — at any cost. It is our chance to understand our own existence in a broader context. This work demonstrates that the information nature provides us with in the form of transmission spectra is sufficient to uniquely constrain the compositions of the atmospheres and answer many of our questions. Even better, this work also demonstrates that, for the most favorable planets, current instrumentation is on the verge of finding atmospheric signatures and determining what the hydrogen and water fractions of super-Earths are. Based on the findings in Chapter 4, for example, the largest Hubble Space Telescope program ever awarded for a single exoplanet was devised in collaboration with Prof. Jacob Bean. The program will hopefully provide the first hints of the atmospheric composition of the super-Earth GJ 1214b.

Ultimately, more powerful telescopes are required to study the detailed compositions of exoplanet atmospheres. Today's telescopes do not provide sufficient spectral coverage required for unique characterizations, and the data are often plagued by systematic instrumental noise sources. Scheduled for launch in 2018, the *James Webb*

Space Telescope (JWST) has the potential of characterizing the first atmospheres of temperate terrestrial planets — if one is found to orbit nearby M-dwarfs in the habitable zone. Programs like *MEarth* or the proposed *TESS* mission are on the way to search for these prime targets. Ultimately, a dedicated mission such as the proposed EChO mission investigated in chapter 5 will be the key to probing and uniquely characterizing the composition of tens of temperate planets.

Appendix A

An Algebraic Solution to Infer the Mean Molecular Mass

For thin or cloudy atmospheres the change in the transit depth across the spectrum, $\Delta\delta$, as proposed by Miller-Ricci et al. (2009), cannot be used to uniquely constrain the mean molecular mass because clouds, hazes, and a surface also affect the feature depths. Here, we show that measuring the linear slope of the Rayleigh scattering signature or the shapes of individual features, instead, does provide constraints on the atmosphere scale height and can be used to estimate the mean molecular mass for general atmospheres independently of other atmospheric properties. We derive an algebraic solutions that can be used to infer the mean molecular mass directly from the transmission spectrum.

From the geometry described by Brown (2001), we obtain the slant optical depth, $\tau(b)$, as a function of the impact parameter, b, by integrating the opacity through the planet's atmosphere along the observer's line of sight:

$$\tau_\lambda(b) = 2\int_b^\infty \sigma_\lambda(r)\, n(r)\, \frac{r\,dr}{\sqrt{r^2 - b^2}}. \tag{A.1}$$

Here, r is the radial distance from the center of the planet. For Rayleigh scattering, the extinction cross section is only very weakly dependent on pressure and temperature, and we can assume $\sigma_\lambda(r) = \sigma_\lambda$. Furthermore, motivated by hydrostatic

equilibrium, we assume that the atmospheric number density falls off exponentially according to $n(r) = n_0 e^{-\frac{r}{H}}$, where H is the atmospheric scale height. With these assumptions we can analytically perform the integration in Equation (A.1) and obtain

$$\tau_\lambda(b) = 2n_0\sigma b\mathcal{K}_1\left(\frac{b}{H}\right) \approx 2n_0\sigma b\sqrt{\frac{\pi}{2\frac{b}{H}}}e^{-\frac{b}{H}}, \tag{A.2}$$

where the modified Bessel function of the second kind $\mathcal{K}_1(x)$ is approximated by its asymptotic form $\mathcal{K}_1(x) = \sqrt{\frac{\pi}{2x}}e^{-x}\left[1 + O\left(\frac{1}{x}\right)\right]$ for large x (Bronstein et al., 1999). For spectral regions, for which the atmosphere is optically thick, the surface does not affect the transmission spectrum and the observed planet radius as a function of wavelength can be approximated as

$$R_{P,\lambda} \approx b(\tau_\lambda = 1), \tag{A.3}$$

because the number density falls exponentially with altitude leading to steep increase in τ_λ as a function of b. Forming the ratio between the radii at two different wavelengths, λ_1 and λ_2, for which the extinction cross sections are σ_1 and σ_2, and solving for the scale height, we obtain

$$H|_{r=R_P} \approx \frac{R_{P,2} - R_{P,1}}{\ln\left(\frac{\sigma_2}{\sigma_1}\sqrt{\frac{R_{P,2}}{R_{P,1}}}\right)} \longrightarrow \frac{dR_{P,\lambda}}{d\ln\left(\sigma_\lambda\sqrt{R_{P,\lambda}}\right)} \approx \frac{dR_{P,\lambda}}{d(\ln\sigma_\lambda)}, \tag{A.4}$$

where we considered the limit of $\lambda_1 \to \lambda_2$ and then approximated for $\frac{d\ln R_{P,\lambda}}{d\ln\sigma_\lambda} \ll 1$.

Given an estimate of the atmospheric temperature, e.g., $T \approx T_{\rm eq}$, we can observationally determine an estimate on the mean molecular mass

$$\mu_{\rm mix} = \frac{k_B T}{g}\left(\frac{dR_{P,\lambda}}{d(\ln\sigma_\lambda)}\right)^{-1} \times \left(1 \pm \frac{\delta T}{T}\right), \tag{A.5}$$

where the factor $\left(1 \pm \frac{\delta T}{T}\right)$ accounts for the inherent uncertainty due to the uncertainty, δT, in modeling the atmospheric temperature, T, at the planetary radius $r = R_{P,\lambda}$.

At short wavelengths for which Rayleigh scattering dominates, the extinction cross

section σ is proportional to λ^{-4}, and we obtain

$$H \approx \frac{R_{P,\lambda_2} - R_{P,\lambda_1}}{4 \ln\left(\frac{\lambda_1}{\lambda_2}\right)}. \tag{A.6}$$

Given two transit depth observations at $\lambda_1$and λ_2 in the Rayleigh scattering regime, we obtain the estimate for the mean molecular mass

$$\mu_{\rm mix} = \frac{4k_B T}{g R_*} \frac{\ln\left(\frac{\lambda_1}{\lambda_2}\right)}{\left(\frac{R_p}{R_*}\right)_{\lambda_2} - \left(\frac{R_p}{R_*}\right)_{\lambda_1}} \times \left(1 \pm \frac{\delta T}{T}\right). \tag{A.7}$$

Bibliography

Aitchison, J. 1986, The Statistical Analysis of Compositional Data (Monographs on Statistics and Applied Probability), 1st edn. (Chapman & Hall Ltd., London)

Barclay, T., Huber, D., Rowe, J. F., et al. 2012, The Astrophysical Journal, 761, 53

Bean, J. L., Désert, J.-M., Kabath, P., et al. 2011, The Astrophysical Journal, 743, 92

Bean, J. L., Kempton, E. M.-R., & Homeier, D. 2010, Nature, 468, 669

Benneke, B. & Seager, S. 2012, The Astrophysical Journal, 753, 100

Berta, Z. K., Charbonneau, D., Bean, J., et al. 2011, The Astrophysical Journal, 736, 12

Berta, Z. K., Charbonneau, D., Désert, J.-M., et al. 2012, The Astrophysical Journal, 747, 35

Blank, R., Anglin, S., Beletic, J. W., et al. 2012, 845310

Borysow, A. 2002, Astronomy and Astrophysics, 390, 4

Bronstein, I. N., Semendjajew, K. A., & Musiol, G. 1999, Taschenbuch Der Mathematik (Frankfurt: Deutsch Harri GmbH; Auflage: 4., überarb. u. erw. A.)

Brown, J. C. & Craig, I. J. D. 1986, Inverse Problems in Astronomy, A guide to inversion strategies for remotely sensed data, 1st edn. (Taylor & Francis)

Brown, T. M. 2001, The Astrophysical Journal, 553, 1006

Burrows, A., Budaj, J., & Hubeny, I. 2008, The Astrophysical Journal, 678, 1436

Burrows, A., Marley, M., Hubbard, W. B., et al. 1997, The Astrophysical Journal, 491, 856

Burrows, A. & Sharp, C. M. 1999, The Astrophysical Journal, 512, 843

Chahine, M. T. 1974, Journal of the Atmospheric Sciences, 31, 233

Charbonneau, D., Berta, Z. K., Irwin, J., et al. 2009, Nature, 462, 891

Christensen, P. R. & Pearl, J. C. 1997, Journal of Geophysical Research: Planets, 102, 10875–10880

Conrath, B. 1998

Croll, B., Albert, L., Jayawardhana, R., et al. 2011, The Astrophysical Journal, 736, 78

Crossfield, I. J. M., Barman, T., & Hansen, B. M. S. 2011, The Astrophysical Journal, 736, 132

Deming, D., Seager, S., Winn, J., et al. 2009, Publications of the Astronomical Society of the Pacific, 121, 952

Des Marais, D. J., Harwit, M. O., Jucks, K. W., et al. 2002, Astrobiology, 2, 153

Désert, J.-M., Kempton, E. M.-R., Berta, Z. K., et al. 2011, The Astrophysical Journal, 731, L40

Ehrenreich, D., Tinetti, G., Etangs, A. L. d., Vidal-Madjar, A., & Selsis, F. 2006, Astronomy and Astrophysics, 448, 15

Etangs, A. L. d., Pont, F., Vidal-Madjar, A., & Sing, D. 2008, Astronomy and Astrophysics, 481, 4

Feroz, F. & Hobson, M. P. 2008, Monthly Notices of the Royal Astronomical Society, 384, 449

Feroz, F., Hobson, M. P., & Bridges, M. 2009, Monthly Notices of the Royal Astronomical Society, 398, 1601–1614

Ford, E. B. 2005, The Astronomical Journal, 129, 1706

Fortney, J. J., Marley, M. S., Saumon, D., & Lodders, K. 2008, The Astrophysical Journal, 683, 1104

Gelman, A., Carlin, J. B., Stern, H. S., & Rubin, D. B. 2003, Bayesian Data Analysis, Second Edition, 2nd edn. (Chapman and Hall/CRC)

Glauser, A. 2013, Submitted to Jornal of Astronomical Instrumentation

Goody, R. M. & Yung, Y. L. 1995, Atmospheric Radiation: Theoretical Basis, 2nd edn. (Oxford University Press, USA)

Gregory, P. C. 2005, The Astrophysical Journal, 631, 1198

Guillot, T. 2010, Astronomy and Astrophysics, 520, 13

Hansen, J. E. & Travis, L. D. 1974, Space Science Reviews, 16, 527

Heng, K. 2012, The Astrophysical Journal, 748, L17

Hinkley, S., Oppenheimer, B. R., Zimmerman, N., et al. 2011, Publications of the Astronomical Society of the Pacific, 123, 74, ArticleType: research-article / Full publication date: January 2011 / Copyright © 2011 The University of Chicago Press

Howard, A. W., Marcy, G. W., Bryson, S. T., et al. 2012, The Astrophysical Journal Supplement Series, 201, 15

Hunten, D. M. 1983, Venus (University of Arizona Press)

Jessberger, E. K. & Kissel, J. 1991, in , 1075–1092

Knutson, H. A., Charbonneau, D., Allen, L. E., Burrows, A., & Megeath, S. T. 2008, The Astrophysical Journal, 673, 526

Krasnopolsky, V. A., Maillard, J. P., & Owen, T. C. 2004, Icarus, 172, 537

Kuchner, M. J. 2003, The Astrophysical Journal, 596, L105

Lee, J. m., Fletcher, L. N., & Irwin, P. G. J. 2011, Monthly Notices of the Royal Astronomical Society, 420, 170

Lefevre, F. & Forget, F. 2009, Nature, 460, 720

Léger, A., Selsis, F., Sotin, C., et al. 2004, Icarus, 169, 499

Line, M. R., Zhang, X., Vasisht, G., et al. 2012, The Astrophysical Journal, 749, 93

Lodders, K. & Jr, B. F. 1998, The Planetary Scientist's Companion (Oxford University Press, USA)

Macintosh, B. A., Graham, J. R., Palmer, D. W., et al. 2008, 701518

Madhusudhan, N., Harrington, J., Stevenson, K. B., et al. 2011a, Nature, 469, 64

Madhusudhan, N., Mousis, O., Johnson, T. V., & Lunine, J. I. 2011b, The Astrophysical Journal, 743, 191

Madhusudhan, N. & Seager, S. 2009, The Astrophysical Journal, 707, 24

McKay, C. P., Pollack, J. B., & Courtin, R. 1989, Icarus, 80, 23

Miller-Ricci, E. & Fortney, J. J. 2010, The Astrophysical Journal, 716, L74

Miller-Ricci, E., Seager, S., & Sasselov, D. 2009, The Astrophysical Journal, 690, 1056

Morley, C. V., Fortney, J. J., Marley, M. S., et al. 2012, The Astrophysical Journal, 756, 172

Nettelmann, N., Fortney, J. J., Kramm, U., & Redmer, R. 2011, The Astrophysical Journal, 733, 2

Nutzman, P. & Charbonneau, D. 2008, Publications of the Astronomical Society of the Pacific, 120, 317, ArticleType: research-article / Full publication date: March 2008 / Copyright © 2008 The University of Chicago Press

Oppenheimer, B. R., Baranec, C., Beichman, C., et al. 2013, arXiv:1303.2627

Palle, E., Osorio, M. R. Z., Barrena, R., Montanes-Rodriguez, P., & Martin, E. L. 2009, Nature, 459, 814

Pater, I. d. & Lissauer, J. J. 2010, Planetary Sciences, 2nd edn. (Cambridge University Press)

Pawlowsky-Glahn, V. & Egozcue, J. J. 2006, in Compositional Data Analysis in the Geosciences: From Theory to Practice, Vol. 264 (Geological Society, London, Special Publications), 1–10

Perna, R., Heng, K., & Pont, F. 2012, arXiv:1201.5391

Querry, M. 1987, 333

Ressler, M. E., Cho, H., Lee, R. A. M., et al. 2008, 70210O

Rodgers, C. D. 2000, Inverse Methods for Atmospheric Sounding: Theory and Practice (Singapore: World Scientific)

Rogers, L. A. & Seager, S. 2010a, The Astrophysical Journal, 712, 974

Rogers, L. A. & Seager, S. 2010b, The Astrophysical Journal, 716, 1208

Rothman, L., Gordon, I., Barbe, A., et al. 2009, Journal of Quantitative Spectroscopy and Radiative Transfer, 110, 533

Rothman, L., Gordon, I., Barber, R., et al. 2010, Journal of Quantitative Spectroscopy and Radiative Transfer, 111, 2139

Schiebener, P., Straub, J., Levelt Sengers, J. M. H., & Gallagher, J. S. 1990, Journal of Physical and Chemical Reference Data, 19, 677

Seager, S. & Deming, D. 2010, Annual Review of Astronomy and Astrophysics, 48, 631

Seager, S., Kuchner, M., Hier-Majumder, C. A., & Militzer, B. 2007, The Astrophysical Journal, 669, 1279

Seager, S., Richardson, L. J., Hansen, B. M. S., et al. 2005, The Astrophysical Journal, 632, 1122

Seager, S., Whitney, B. A., & Sasselov, D. D. 2000, The Astrophysical Journal, 540, 504

Segura, A., Kasting, J. F., Meadows, V., et al. 2005, Astrobiology, 5, 706

Sellke, T., Bayarri, M. J., & Berger, J. O. 2001, The American Statistician, 55, 62

Shao, M., Deems, E., & Fletcher, L. 2010, Response to Request for Information for Proposed Activities Dilute Aperture Visible Nulling Coronagraph Imager (DAViNCI) Imaging and Spectroscopy of Exo-planets from Nearby Stars, Tech. rep.

Showman, A. P., Fortney, J. J., Lian, Y., et al. 2009, The Astrophysical Journal, 699, 564

Sivia, D. S. & Skilling, J. 2006, Data analysis: a Bayesian tutorial (Oxford University Press)

Skilling, J. 2004, AIP Conference Proceedings, 735, 395

Smith, W. L. 1970, Applied Optics, 9, 1993

Sneep, M. & Ubachs, W. 2005, Journal of Quantitative Spectroscopy and Radiative Transfer, 92, 293

Susskind, J., Barnet, C., & Blaisdell, J. 2003, Geoscience and Remote Sensing, IEEE Transactions on, 41, 390

Tinetti, G., Beaulieu, J. P., Henning, T., et al. 2012, Experimental Astronomy, 34, 311

Trotta, R. 2008, Contemporary Physics, 49, 71

Turnbull, M. C., Traub, W. A., Jucks, K. W., et al. 2006, The Astrophysical Journal, 644, 551

Valenti, J. A. & Piskunov, N. 1996, Astronomy and Astrophysics Supplement Series, 118, 595

Winn, J. N. 2011, in Exoplanets (University of Arizona Press)